CHALMERS

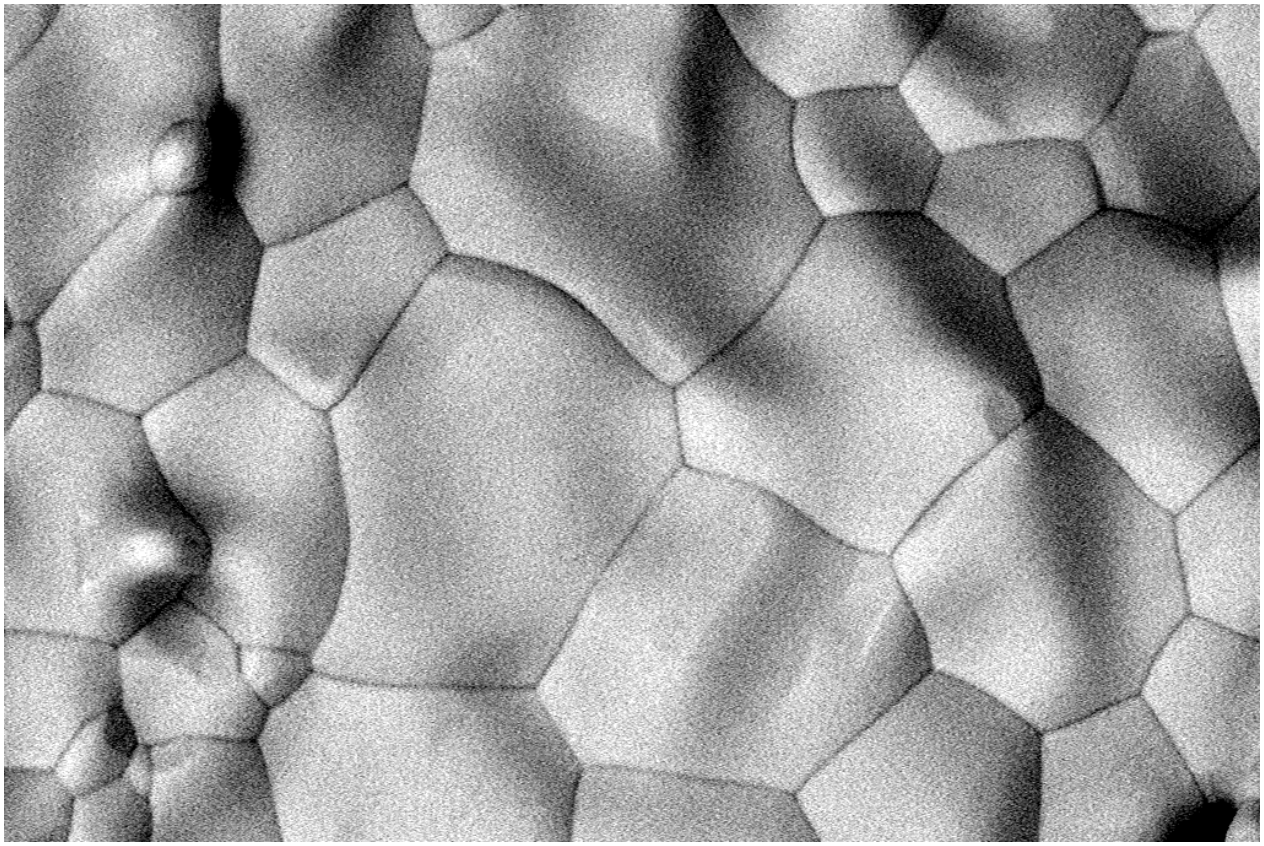

Synthesis and Densification of $BaTiO_3$ based Proton Conducting Oxides for Clean Energy Applications

Master thesis within the program of Materials Chemistry and Nanotechnology

ADAM BENSON

Department of Chemistry and Chemical Engineering
CHALMERS UNIVERSITY OF TECHNOLOGY
Gothenburg, Sweden 2015

CHALMERS

Synthesis and Densification of $BaTiO_3$ based Proton Conducting Oxides for Clean Energy Applications

A study on the impact of ceramic processing and chemical modification on the density and proton conductivity of $BaTiO_3$ based proton conducting oxides

ADAM BENSON

Department of Chemistry and Chemical Engineering
CHALMERS UNIVERSITY OF TECHNOLOGY
Gothenburg, Sweden 2015

CHALMERS

Synthesis and Densification of $BaTiO_3$-based Proton Conducting Oxides for Clean Energy Applications
A study on the impact of ceramic processing and chemical modification on the density and proton conductivity of $BaTiO_3$ based proton conducting oxides
ADAM BENSON

Department of Chemistry and Chemical Engineering
Chalmers University of Technology
SE-412 96 Gothenburg
Sweden
Telephone + 46 (0)31-772 1000

Study performed in collaboration with Swerea IVF.

Cover:
[A picture of the fracture surface of a $BaTi_{0.3}In_{0.7}O_{3-\delta}$ pellet with an average grain size of 10µm, taken with a scanning electron microscope. Can be found on page 59.]

Department of Chemistry and Chemical Engineering
Gothenburg, Sweden 2015

CHALMERS

Synthesis and Densification of $BaTiO_3$-based Proton Conducting Oxides for Clean Energy Applications
A study on the impact of ceramic processing and chemical modification on the density and proton conductivity of $BaTiO_3$ based proton conducting oxides

ADAM BENSON
Department of Chemistry and Chemical Engineering
Chalmers University of Technology

ABSTRACT
The aim of this thesis was to investigate different possibilities of improving the density and proton conductivity of two different barium titanate-based materials, namely $BaTi_{0.3}Sc_{0.7}O_{3-\delta}$ and $BaTi_{0.3}In_{0.7}O_{3-\delta}$. Two different approaches have been employed: chemical modification and ceramic processing. The two base materials were chemically modified in two different ways: by introduction of tin, substituting some of the titanium, or by a mixed substitution of indium and scandium. The ceramic processing approach was split into three different routes involving ball milling, cold isostatic pressing and slipcasting. The different materials were synthesized by the standard solid state reaction and sintering technique and analyzed using X-ray diffraction, scanning electron microscopy, thermogravimetric analysis and impedance spectroscopy to elucidate phase purity, microstructure, hydration behavior and conductivity.

The results from X-ray diffraction showed that the scandium substituted samples, irrespective of chemical modification or processing, were more difficult to purify than the indium substituted counterparts, i.e. they required a higher sintering temperature. Using ball milling and cold isostatic pressing, pure $BaTi_{0.3}Sc_{0.7}O_{3-\delta}$ was obtained after a final sintering at 1500ºC. $BaTi_{0.3}In_{0.7}O_{3-\delta}$ on the other hand achieved phase purity after a final sintering at 1400ºC, even without any previous ceramic processing. Examining the results of thermogravimetric analysis showed that all synthesized samples could be purposefully hydrated and achieve a hydration level between 76-100% of the maximum theoretical level of hydration, depending on the chemical makeup and previous processing of the sample in question. The introduction of tin seems to have improved the materials' ability to retain some remnant hydration at higher temperatures while the mixed scandium and indium substituted samples showed a dehydration behavior in between that of the purely indium and purely scandium substituted samples. In addition, the mixed scandium/indium samples displayed a synergistic effect in terms of the extent of hydration, reaching higher levels of hydration than both $BaTi_{0.3}Sc_{0.7}O_{3-\delta}$ and $BaTi_{0.3}In_{0.7}O_{3-\delta}$. Only some of the processed samples were analyzed by thermogravimetry and displayed a hydration behavior much like that of their non-processed cousins. This is not surprising, as these two sets of samples only differed in the ceramic processing that they were subjected to and not in chemical makeup.

It was found that chemical modification approach did not succeed in achieving materials of a higher (relative) density, instead a small decrease in density compared to the purely scandium or indium substituted samples was observed. In contrast, some of the processing routes did yield significant increases in density, especially the route involving ball milling and cold isostatic pressing of the sample powder as an ethanol-containing paste. In one of the most successful cases, this ceramic processing route yielded a sample of $BaTi_{0.3}Sc_{0.7}O_{3-\delta}$ with a relative density of 93%, a result which the author has not found to be achieved in any other study, nor in this one using any other approach. This same processing route also, routinely, yielded samples of $BaTi_{0.3}In_{0.7}O_{3-\delta}$ with relative densities >95%. Scanning electron microscopy, performed on two isostatically pressed samples, gave an indication of the correctness of the calculated relative densities and revealed a larger grain size of 10µm in the BTI70 sample compared to the 2µm of the BTS70 sample.

The conductivity results obtained from the preliminary analysis of the impedance data have been found to be comparable to those reported in previous studies on similar materials. In addition, the data indicates extensive proton conduction present in both $BaTi_{0.3}In_{0.7}O_{3-\delta}$ and $BaTi_{0.3}Sc_{0.7}O_{3-\delta}$, as indicated by the orders of magnitude higher conduction in a wet versus a dry atmosphere. Nonetheless, no correlation between an increased density causing an increase in conductivity has been found.

Keywords: barium titanate, scandium substitution, indium substitution, proton conductivity, density, chemical modification, ceramic processing, cold isostatic pressing, ball milling, slipcasting, hydration, impedance spectroscopy.

FOREWORD/ACKNOWLEDGEMENTS

The author would like to give special thanks to his supervisor Christopher Knee, Associate Professor at the Department of Chemistry and Chemical Engineering, Chalmers University of Technology, Gothenburg, Sweden for his guidance, ideas and helpfulness during the entire span of the thesis. The author would also like to thank Nico Torino for his help and his playing of music during lab work. Special thanks also goes out to Seikh Mohammad Habibur Rahman for his expert guidance on impedance spectroscopy and other assorted lab equipment. Last but not least, the author would also like to thank Johanna Stiernstedt at Swerea IVF in Mölndal, Sweden for her guidance in the labs of Swerea IVF and for sharing her knowledge of ceramic processing.

Table of Contents

List of abbreviations

Abbreviation	Meaning
SOFC	**S**olid **O**xide **F**uel **C**ell
YSZ	**Y**ttria-**S**tabilized **Z**irconia
AC	**A**lternating **C**urrent
TGA	**T**hermo**g**ravimetric **A**nalysis
DSC	**D**ifferential **S**canning **C**alorimetry
XRD	**X**-**R**ay **D**iffraction
SEM	**S**canning **E**lectron **M**icroscopy
CIP	**C**old **I**sostatic **P**ressing
T-BTS70	**T**rial-**B**a**T**i$_{0.3}$**S**c$_{\mathbf{0.7}}$O$_{3-\delta}$
T-BTI70	**T**rial-**B**a**T**i$_{0.3}$**I**n$_{\mathbf{0.7}}$O$_{3-\delta}$
P-BTS70	**P**rocessing-**B**a**T**i$_{0.3}$**S**c$_{\mathbf{0.7}}$O$_{3-\delta}$
P-BTI70	**P**rocessing-**B**a**T**i$_{0.3}$**I**n$_{\mathbf{0.7}}$O$_{3-\delta}$
BTSI35	**B**a**T**i$_{0.3}$**S**c$_{\mathbf{0.35}}$**I**n$_{0.35}$O$_{3-\delta}$
BTSI50	**B**a**T**i$_{0.3}$**S**c$_{\mathbf{0.5}}$**I**n$_{0.2}$O$_{3-\delta}$
BSTS70	**B**a**S**n$_{0.15}$**T**i$_{0.15}$**S**c$_{\mathbf{0.7}}$O$_{3-\delta}$
BSTI70	**B**a**S**n$_{0.15}$**T**i$_{0.15}$**I**n$_{\mathbf{0.7}}$O$_{3-\delta}$

List of tables

List of figures

1. Introduction

The issue of global warming has occupied the center stage in international environmental debate for decades. Rising global temperatures and sea levels are making climate refugees out of already exposed groups of people and threaten to shift the global climate towards a more inhospitable variant of the one we have today. As many now know, society's consumption of fossil fuels such as oil and coal is the main contributing factor to this problem and many new technologies based on renewable fuels have emerged in response. Examples include combustion of biomass and the increasingly effective modern photovoltaic, or solar, cells. Some of these technologies have the added advantage of releasing considerably less polluting species into the atmosphere and waterways than traditional energy sources and technologies. [1], [2]

One technology which has the potential, in the ideal case, to provide the modern society with energy, without polluting the atmosphere and contributing to global warming through emission of greenhouse gases, is the fuel cell. The fuel cell operates on a relatively simple principle utilizing a fuel gas such as hydrogen, propane or natural gas in junction with an oxidizing gas, most often the oxygen in air, to produce electricity but also heat which can be harnessed by heat recovery if necessary. The gaseous reactants react with each other at one of the two electrodes by transport of one of the species, in ionic form, through an electrolyte while electrons travel in the external circuit. Consequently, the electrolyte is designed to transport either ions of the fuel gas or oxygen ions. Depending on the fuel gas that is used, different types of electrolyte materials are employed and the fuel cells are often characterized according to their electrolyte material. [2], [3], [4]

One type of fuel cell utilizes ceramic oxides as a solid electrolyte material and is therefore aptly named as the solid oxide fuel cell, or SOFC. SOFCs can so far almost exclusively be used at relatively high temperatures between 600 and 1000°C and are therefore best suited for generation of electricity in large heat and power plants since the high operating temperatures required lead to slow startup. The reason for the high operating temperature is mainly the slow rate of transport of oxygen ions through the electrolyte at lower temperatures. [2], [3], [5]

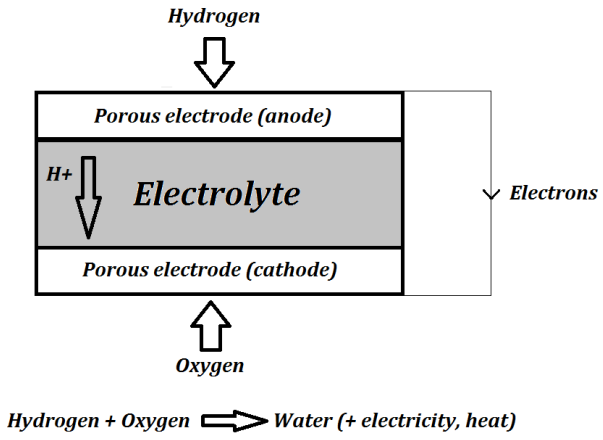

Figure 1. A schematic figure showing the principal components of a proton conducting solid oxide fuel cell utilizing hydrogen gas as fuel.

A sub-class of solid oxide fuel cells is the proton conducting SOFCs, see figure 1. Proton conducting materials have the potential to play a pivotal role in the transition to a cleaner energy based future through their use as electrolytes in solid oxide fuel cells which operate in the intermediate temperature range (200°C-600°C), i.e. in a lower range than traditional SOFCs. Other possible applications, apart from fuel cells, include steam electrolyzers as well as humidity and hydrogen

sensors. The advantage of proton conducting electrolytes over standard oxygen ion conducting materials is the high ion conductivity in this lower temperature range as well as facilitated water management. [6], [7], [8], [9]

1.1 Background

There is a strong interest in developing the fuel cell technology and, in particular, that of the solid oxide fuel cells because of advantages over other energy converting technologies. These advantages include a high energy efficiency and potential for non-existent air pollution. However, this does not mean that there isn't room for improvement, as extensive research and development is going into improving the reliability and long term performance through improved low and medium temperature operation. [2], [5]

A possible candidate for medium temperature operation (200-600^{o}C) is a sub-class of SOFCs, namely the proton conducting solid oxide fuel cells. One of the most prominent classes of materials used as electrolyte in proton conducting SOFCs are the lower valence-substituted perovskites, which have been heavily studied in this context for some years. Different perovskites have been studied, although research has mainly focused on alkaline earth zirconates and cerates, see [10-13], and relatively little research has gone into other alkaline earth compounds, such as alkaline earth titanates. [6], [8]

One type of alkaline earth titanate which has demonstrated proton conductivity when a fraction of the titanium is substituted with a metal of lower valence is barium titanate. One of the main problems with the preparation of barium-containing proton conducting ceramics however, is the difficulty with which to strike a balance between high density and low barium deficiency in the finished material. In other words, it's a challenge to produce a dense polycrystalline material while also preventing the evaporation of barium during the high sintering temperatures necessary for acceptable densification. Some studies have already tried to address this problem by for example covering the prepared pellet with barium-containing powder to prevent barium loss during sintering. [6], [7], [8], [10], [14]

The problem described above for barium titanate seemingly applies to barium zirconate as well as it has been stated that there is a lack of reproducibility when it comes to synthesis of and subsequent conductivity measurements on barium zirconates. Since these issues seem to be shared among at least some of the barium containing alkaline earth perovskites, ideas for solving the problems might be gleaned from successful attempts at improving the densification of, if not barium titanate, compounds belonging to this family. Barium cerate based materials, for example, have benefited from an increased density when prepared as freeze dried precursors before final sintering. In summary, the common factors for preparation of dense ceramic materials are the avoidance of agglomerates and achieving a small particle size, see [15-17, 10].

In light of the information presented above, one wise approach might be to introduce additional processing steps before final sintering in order to improve the density of the finished material. More specifically, the utilization of ball milling to reduce particle size in junction with different procedures

before final sintering, such as cold isostatic pressing (CIP) and slipcasting, could result in dense and high performance proton conducting barium titanate-based materials.

1.2 Purpose

The purpose of this study was to find ways to improve the density and conductivity of two barium titanate-based proton conducting materials, namely $BaTi_{0.3}Sc_{0.7}O_{3-\delta}$ and $BaTi_{0.3}In_{0.7}O_{3-\delta}$. Two different approaches have been used: chemical modification and utilization of ceramic processing steps, see figure below.

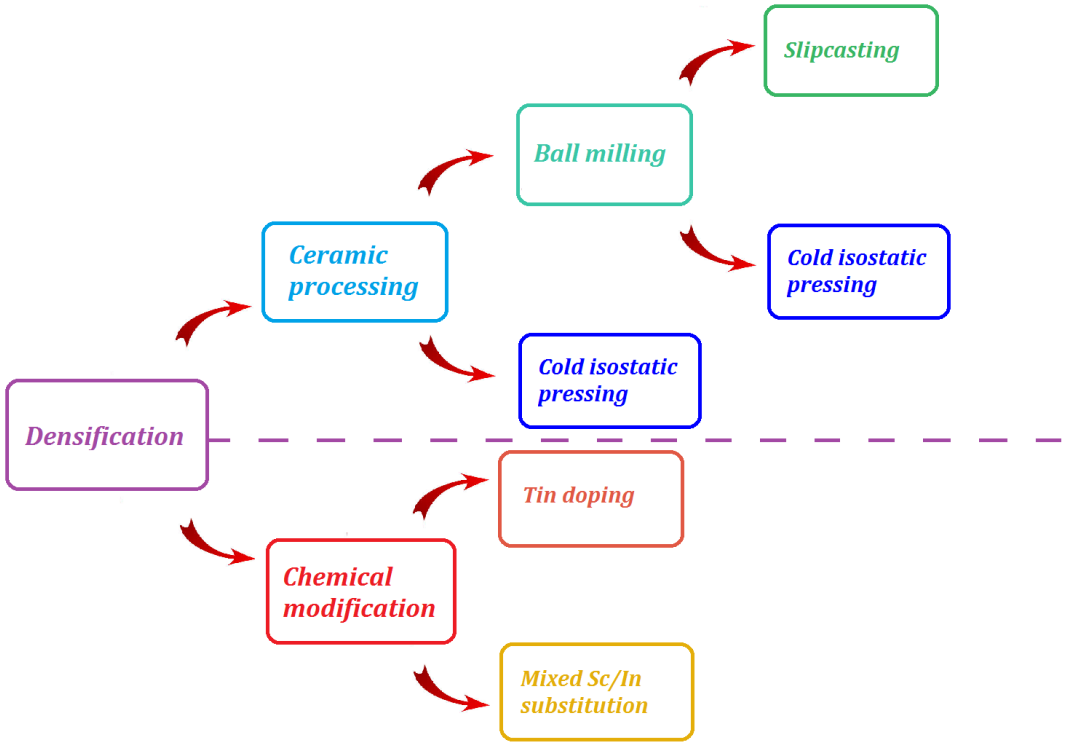

Figure 2. A schematic figure showing the principal steps of the two different approaches used to improve the density of $BaTi_{0.3}Sc_{0.7}O_{3-\delta}$ and $BaTi_{0.3}In_{0.7}O_{3-\delta}$, namely the ceramic processing approach and the chemical modification approach. The dashed line separates the two.

In addition, the materials were characterized using X-ray diffraction, scanning electron microscopy, thermogravimetric analysis and impedance spectroscopy in order to elucidate phase purity, microstructure, hydration behavior, conductivity etc.

1.3 Practical constraints

Constraint 1.
The laboratory work in terms of synthesis, densification and characterization was limited to four sets of materials, all based on barium titanate:
1. $BaTi_{0.3}Sc_{0.7}O_{3-\delta}$ and $BaTi_{0.3}In_{0.7}O_{3-\delta}$ (trial samples)
2. $BaTi_{0.3}Sc_{0.7}O_{3-\delta}$ and $BaTi_{0.3}In_{0.7}O_{3-\delta}$ (ceramic processing samples)
3. $BaTi_{0.3}Sc_{0.35}In_{0.35}O_{3-\delta}$ and $BaTi_{0.3}Sc_{0.5}In_{0.2}O_{3-\delta}$ (mixed Sc/In samples)
4. $BaSn_{0.15}Ti_{0.15}Sc_{0.7}O_{3-\delta}$ and $BaSn_{0.15}Ti_{0.15}In_{0.7}O_{3-\delta}$ (tin samples)

There were different reasons for limiting the scope to these four particular sets. Firstly, a trial set seemed prudent in order to identify problems during synthesis and phase purification. Secondly, a separate set of processing samples was needed in order to thoroughly investigate the effect of different processing routes on sample density. Thirdly, since the effect of processing on density would be investigated using different processing techniques, it seemed advisable to synthesize at least two different sets of chemically modified samples to investigate the effects of different chemical modifications on select sample characteristics.

Constraint 2.
Three different ceramic processing routes have been studied, see figure 3.

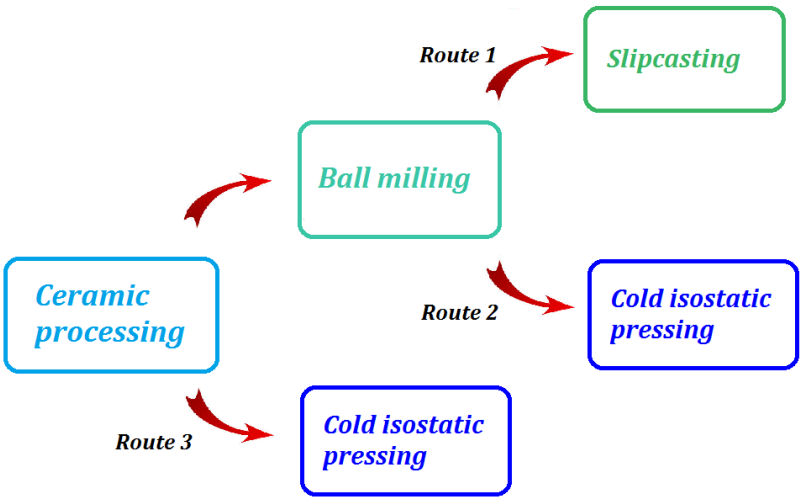

Figure 3. A schematic figure showing the principal steps of the three different ceramic processing routes that were employed in order to improve the density of $BaTi_{0.3}Sc_{0.7}O_{3-\delta}$ and $BaTi_{0.3}In_{0.7}O_{3-\delta}$.

The reasons for using these processing techniques in particular are twofold. Firstly, both slipcasting and isostatic pressing, as well as ball milling, are straightforward routine techniques for processing of

ceramic materials. Secondly, none of them require large amounts of material which was deemed crucial as both indium- and scandium oxide, which were used for synthesis, are expensive reactants.

Constraint 3.
Conductivity was only measured in a wet and dry argon atmosphere, no other gases were used.

1.4 Question formulation

This study aims at answering two central questions:

1. Do the chemical modification or ceramic processing approaches increase the density of the involved materials compared to the original, trial samples?

2. If so, does this result in an appreciable increase in the proton conductivity of the materials, compared to other studies?

2. Theory

Presented below is a theoretical background on fuel cells, proton conduction, the structure of barium titanates etc, as well as on the processing and analysis techniques used in this study.

2.1 Proton conducting solid oxide fuel cells

Much like the general description of a fuel cell given in the introduction, the components of a proton conducting solid oxide fuel cell includes a cathode and an anode connected through an electron-conducting wire, as well as the solid oxide electrolyte in between, which enables proton transport between the two electrodes, see figure 1. The anode must be able to facilitate reaction between the fuel gas, for example H_2, and the electrolyte in order for a sufficient amount of protons to be formed and then transported through the electrolyte. It must also be porous in order to ensure extensive contact between the fuel gas and itself. This goes for the cathode as well, to facilitate the reaction between protons and oxygen ions on the cathode side. The demands put on the electrolyte include blocking of extensive electron transport to prevent short circuit and, of course, satisfactory proton conduction characteristics. The electrode reactions that take place in a proton conducting SOFC utilizing hydrogen gas and oxygen are shown in equations 1, 2 and 3 below. [2], [4]

Anode:

$$2H_2 \rightarrow 4H^+ + 4e^- \qquad (1)$$

Cathode:

$O_2 + 4e^- \rightarrow 2O^{2-}$ (2)

$4H^+ + 2O^{2-} \rightarrow 2H_2O$ (3)

2.2 Proton transfer in ceramic oxides and other materials

There are several different types of proton conduction mechanisms operating in different kinds of materials. Examples include transport of protons through liquid regions of water that exist throughout the material, such as in polymer membranes, or conduction enabled by proton vacancies or interstitials in a material with crystallographically fixed protons, such as in different types of crystalline hydrates. The mechanism for proton conduction in the materials relevant to this investigation involves protonic defects being introduced into the material through water vapor. The water molecule dissociates, forming a hydroxide ion and a proton. The hydroxide ion fills an oxygen vacancy present in the material while the proton bonds to an oxygen ion in the lattice to form another hydroxide ion, effectively introducing two proton defects in the structure. The oxygen vacancy mentioned is created during material synthesis by substitution of lattice cations with lower valence cations, inducing a charge imbalance in the structure. This balance is restored by the loss of oxygen anions. The equilibrium of water vapor, oxygen lattice atoms and oxygen vacancies with the hydroxide groups enabling mobile protons can be described, using Kröger-Vink notation, by equation 4 below where O_O^x is an oxygen atom, of neutral charge, situated at an oxygen site in the lattice, $V_O^{\cdot\cdot}$ is a doubly positive vacancy situated at an oxygen site and $OH_O^{\cdot}$ is an hydroxide ion denoted with a single positive charge compared to the oxygen site it occupies. [6], [9], [18], [19]

$$H_2O(g) + O_O^x + V_O^{\cdot\cdot} = 2OH_O^{\cdot} \quad (4)$$

The hydration reaction represented by equation 4 is typically exothermic which means that at high temperatures the reaction becomes disfavored, causing dehydration. Consequently, the amount of protons available for transport decreases and in extension the conductivity decreases. The proton conductivity in these types of materials therefore, generally, reaches a maximum at some characteristic temperature as the dehydration reaction becomes favorable and outweighs the gain in conductivity caused by the increased mobility of the protons when the temperature is raised. It is also obvious from equation 4 that increasing water vapor partial pressure or the amount of oxygen vacancies, through doping for example, favors the formation of hydroxide groups and consequently mobile protons in the material. [9], [18]

The mobility of ions in any material is governed by different factors such as the polarizability of the lattice, electrostatic interaction between the ion and the local environment or structure, as well as the strain energy. The strain energy can be summarized as the ability of an ion to push through the tight corridors or channels of a lattice and depends on the polarizability of the ion and the amount of free volume available for it to move through. [18]

In contrast to most ions, protons, having a very small radius and being in principle an unshielded singly positively charged particle, have an extremely high polarizing ability which is the origin of its unique transport mechanisms. The movement of protons through an oxide material can be described by two elementary steps, termed the Grotthus mechanism. The first step is proton reorientation, by rotation around the oxygen it is covalently bonded to. The second step is a jump to the neighboring oxygen ion through oscillation of the proton between the two oxygen ions, enabled by hydrogen bonding. The second elementary step is shown below in equation (5) and (6), while both steps can also be seen in figure 4 below. [19], [20], [18]

$$O_1 - H \cdots O_2 \leftrightarrow O_1 \cdots H - O_2 \quad (5)$$

$$O_1 \cdots H - O_2 \quad (O_3) \leftrightarrow (O_1) \quad O_2 - H \cdots O_3 \quad (6)$$

Using molecular simulations, the detailed behavior of protons in perovskite structures, such as those of $BaCeO_3$ and $BaTiO_3$, have been investigated and reported in the literature, see [19]. It was found that the energetic barrier for the proton transfer step described above and illustrated below in figure 4, is smallest for $BaTiO_3$ when compared to $BaCeO_3$ and $BaZrO_3$, giving rise to predictions of a relatively high proton mobility in this compound since it has been found that the proton transfer step is rate-limiting. [19], [21]

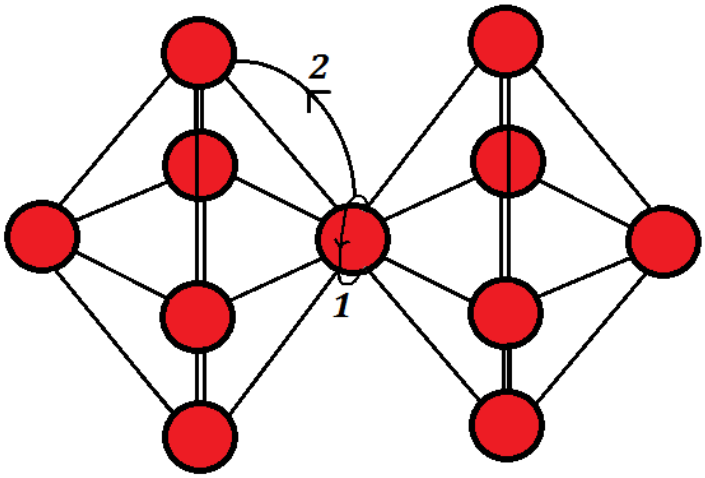

Figure 4. The figure illustrates the rotation of a proton around the oxygen to which it is covalently bonded as well as the proton transfer between two neighboring oxygen ions. Step 1 = Proton rotation, Step 2 = Proton jump. Red circle = oxygen atom, black arrow = moving proton.

As described previously, different kinds of proton conducting materials exhibit different proton conducting mechanisms depending on the nature of the material. Materials containing liquid regions, or layers, of water such as polymer membranes along with those having crystallographically fixed protons, such as hydrates, are very susceptible to dehydration and will in many cases start to lose water at 100°C and 200°C respectively. In contrast, materials that don't have protons as part of their nominal structure are more resistant towards higher temperature and exhibit proton conduction up to 600°C beyond in some cases. Temperature stability isn't the only important aspect when determining the performance of a proton conductor however and it goes without saying that maximum conductivity is also of utmost importance. As be seen in figure 5, the conductivities of some temperature sensitive materials, such as Nafion®, far surpasses those many temperature resistant oxides, although with the disadvantage of losing its conductivity above 100°C. As has been mentioned before, proton conductors generally perform better than oxygen conductors in terms of conductivity at lower temperatures. Nonetheless, there is a gap between 200°C and 600°C within which proton conduction is sub-par. Many applications, within energy conversion for example, require operating temperatures in this range and so bridging this gap is essential in order to meet these requirements and open up such applications for proton conducting materials. [9]

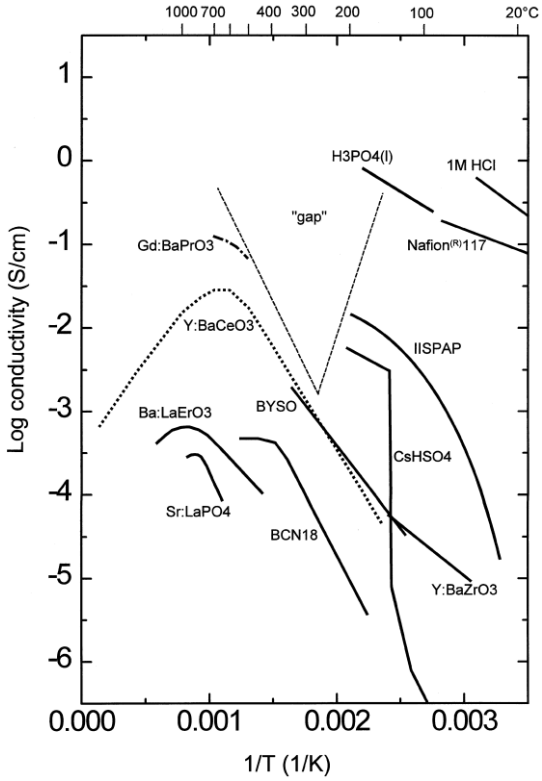

Figure 5. Proton conductivity displayed as a function of inverse temperature for selected proton conducting materials. Note the conductivity gap between 200°C and 600°C. Reproduced from [9] with permission. [9]

2.3 The structure of barium titanates

The materials investigated in this study are all based on barium titanate, $BaTiO_3$. Barium titanate, at ambient conditions, adopts a tetragonal perovskite structure which may change into a cubic perovskite structure upon heating or doping. For example, doping with a certain amount of indium or scandium may change the structure to a cubic or hexagonal perovskite. [22], [6], [8]

The constituent atoms of a perovskite are generally assigned the letters A,B or X depending on their place in the structure, resulting in the general perovskite formula ABX_3, where X can be oxygen for example. Looking at the structure by placing the divalent A cation at the centre of the unit cell, termed the A-type unit cell, it will be coordinated to 12 oxygen ions, denoted O, situated at the midpoints of the cell edges. It will also be surrounded by 8 tetravalent B cations situated at the cell corners. By doping the material, B

cations are substituted with lower valence cations, inducing a charge imbalance in the structure. The balance is restored by elimination of oxygen anions, creating oxygen vacancies. [23], [24]

The substituted perovskites used in solid state proton conductors typically exhibit the highest proton conductivity in the cubic form and their general formula can be written as $AB_{1-x}M_xO_{3-\delta}$, where $\delta = x/2$. Divalent alkaline earth metals occupy the A site and tetravalent metals occupy the B site along with the rare earth dopant metals, M, of lower valence. δ is the oxygen deficiency. An example is the perovskite $BaZr_{1-x}Y_xO_{3-\delta}$. [18]

It has been theorized that the electronegativity of the B-site atom compared to the A-site atom, which is titanium and barium, respectively, in the barium titanate case, will affect the ability of the material to trap protons and consequently affect the extent of hydration. A correlation was found by Norby, see [25], which showed that the smaller the difference between the electronegativity of the B- and A-site atom, the larger the negative enthalpy of hydration, i.e the more readily the material hydrates. If barium titanate is partly substituted with an atom with an electronegativity comparable to Ba, or at least lower in value than that for Ti which it substitutes, it might result in extensive hydration and a good temperature stability of the protonic defects. It should be noted however, that concerns have been raised regarding the validity of this correlation for high substitution levels, something which will be considered in the discussion section. [25], [26]

2.4 Previous studies on heavily substituted barium titanates

Some important studies have been done previously on the structure and conductive behavior of different heavily substituted barium titanates, including $BaTi_{0.5}In_{0.5}O_{3-\delta}$ as well as $BaTi_{1-x}Sc_xO_{3-\delta}$ where the substitution level x ranged from 0.1 to 0.8, see [6]-[8].

Looking at the reported conductivities of these materials when analyzed in wet and/or dry argon, see figure 6 below, it can be seen that between 350 and 500°C for the indium substituted sample and between 400 and 750°C for the scandium substituted samples, there is a conductivity plateau corresponding to the maximum protonic conductivity. At high temperatures, there is practically no proton conduction because the material can't hydrate. At semi-low temperatures there is a good hydration but no great proton mobility (and at very low temperatures hydration kinetics even prevent extensive hydration). The optimum temperature is that which strikes a balance between high proton mobility and satisfactory hydration, which is represented by the conduction plateau. This is where conductivity stays almost constant because of the opposing effects of material dehydration and increased proton mobility at the increasingly high temperatures. At a certain temperature, where proton conduction is at its highest, dehydration starts to win out over proton mobility. However at the same time the curve also, perhaps counterintuitively, starts to bend upwards as other conductive species (electron holes and oxide ions) start to dominate the conductive behavior of the material at these high temperatures.

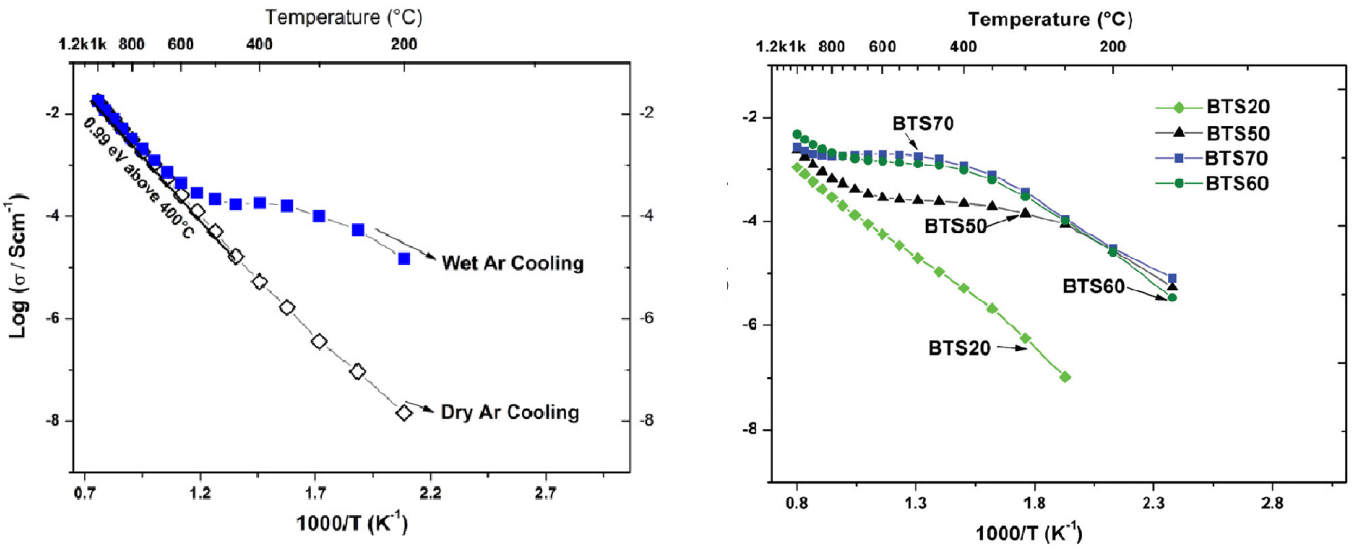

Figure 6. A figure showing conductivity results as reported in studies [6] and [8]. The graph to the left, taken from [6] with permission, shows the conductivity of a $BaTi_{0.5}In_{0.5}O_{3-\delta}$ pellet during cooling in wet and dry argon. The graph to the right, taken from [8] under the Creative Commons Attribution 3.0 Unported Licence, shows the conductivity of $BaTi_{1-x}Sc_xO_{3-\delta}$ pellets where the substitution level x equals 0.2 and 0.5-0.7, during cooling in wet argon.

By comparing the figure above with figure 5 it can be seen that these materials have the potential to fit rather nicely in the proton conduction gap. Improvements have to be achieved first though to fit squarely in the gap. The main challenge is to improve the conductivity by perhaps an order or of magnitude for scandium substituted $BaTiO_3$ and 2 orders of magnitude for indium substituted $BaTiO_3$. A possible way of achieving this, or at least move closer to this goal, would be to improve the density of these materials. The reported relative density value of the 50% indium substituted $BaTiO_3$ in the mentioned study was around 80% while the scandium substituted $BaTiO_3$ densities ranged from 77-89 %, although it seems only the lower level doped samples reached the higher range of these densities. If densities above 90-95 % could be achieved, perhaps these types of materials would be one step closer to filling the proton conducting gap indicated by Norby, see [9]. [6], [7], [8]

2.5 The effect of density on conduction

The effect of a materials density on its conductive properties can be summarized by stating that the presence of pores, i.e voids in the material, impairs conduction between grains by blocking the conduction path between them. Increasing the density is therefore beneficial for the conductivity of a material because the porosity is reduced. In a study on proton conducting yttrium-doped barium zirconate, it was found that high density (and prevention of barium loss during sintering at high temperature) yielded a material with high protonic conductivity compared to many previous studies. [10] Analyzing the problem of porosity in more detail, it is thought that porosity lowers mainly grain boundary conductivity by causing an increase in grain boundary resistance, leaving bulk conductivity

through the grains unchanged. It should be mentioned however that investigations into this phenomenon have so far produced somewhat contradictory results. In order to illustrate the contribution of grain boundary resistance to the total resistance and it's variance with porosity, the ratio $\frac{R_{GB}}{R_{TOTAL}}$ has been introduced, where R_{GB} is the grain boundary resistance and R_{TOTAL} is the total resistance of the material. For some materials it has been found that above a certain percentage porosity, the grain boundary resistance increases rapidly and can even assume a dominating fraction of the materials total resistance. As an illustrative example, the variance of this resistance ratio with porosity for yttria-stabilized zirconia, YSZ, can be seen in figure 7 below. It should be noted that YSZ is an oxide ion conductor and not a proton conductor. [27], [28], [29]

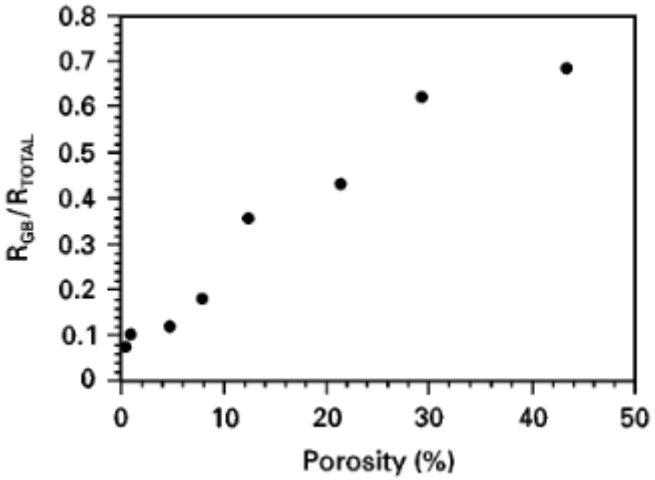

Figure 7. The impact of porosity on the ratio between grain boundary resistance and total resistance for YSZ-material. Reproduced from [27] with permission. [27]

In addition to improving the conductivity, a high density also improves the mechanical properties of most ceramic materials in general. The strength and toughness of ceramics usually decreases with increased porosity and so if a proton conducting material of high density could be achieved, it would consequently become more attractive as a reliable electrolyte which will not break easily when subjected to stresses during manufacturing, handling or operation. [30]

2.6 Processing methods

2.6.1 Ball milling

Ball milling is a processing technique which uses balls, made of an attrition resistant material, to grind a powder sample into a very fine powder of uniform particle size. This is achieved by placing the sample powder in a container, along with balls and often also some liquid media such as water or ethanol. The container is then placed in the ball mill and rotated in such a way that the sample powder is continuously

ground by the moving and cascading balls. Two common types of ball mills are the planetary ball mill and the rolling ball mill. The big difference between these, otherwise very similar, techniques is the fact that a rolling ball mill uses gravity to accelerate the contents of the container while the planetary ball mill uses centrifugal acceleration. On a rolling ball mill the sample is placed lying down, rolling thanks to the movement of two parallel rollers. In a planetary ball mill the sample is placed upright and rotates independently of the underlying counter rotating disc. In this way, a much more efficient milling is achieved. Because of the large centrifugal forces involved in planetary ball milling, a fine powder can be achieved in less time. [31]

2.6.2 Cold isostatic pressing

Cold isostatic pressing, or CIP, is a processing technique which utilizes a liquid such as water to apply pressure on an object isostatically, i.e applying the same pressure from all sides. Because of this, a powder pressed in this way will take the shape of a sphere. If another shape is desired such as that of a pellet, the sample powder must be pre-pressed axially. In order to prevent contamination of the sample, it is placed in an elastomeric vessel that will protect it from the surrounding water while it's elastomer properties hinders it from fracturing under the applied pressure. Typical pressures range from 100 to over 1000 MPa. The CIP variant utilized in this case is the wet bag variant, where the elastomer vessel is not attached to the press but separate from it. It is filled with the sample and then inserted into the press for sample compaction. [32], [33]

Cold isostatic pressing of ceramic and metal powders has been, and is being, studied quite extensively especially in terms of its effects on green and sintered sample density as well as their mechanical properties, although no studies focusing on barium titanates seems to have been conducted. Still, there are general observations regarding the impact of isostatic pressing on the properties of metallic and ceramic materials that should be applicable to barium titanates as well. The CIP technique compacts the material by forcing the collapse of aggregates, pores and by rearranging particles as well as in some cases, thanks to the very high pressures, inducing viscous deformation of particles at their points of contact. Some have likened it to a form of pre-sintering, doing essentially what the initial part of a sintering step would achieve. It can produce uniformly packed and dense green material which can aid densification during a following sintering. [34], [33]

2.6.3 Slipcasting

Slipcasting is a cheap, easy and efficient technique for processing ceramic materials. It relies on sedimention of the sample particles suspended in a liquid such as water or ethanol. After the suspension has been made, it is either poured into a porous plaster mold or into a bottomless non-porous mold with a plaster slab beneath. The liquid is drained from the suspension by either the plaster mold or plaster slab, while the particles sediment on the bottom taking the shape of the mold. To achieve near perfect packing of the particles, deflocculants are often used to achieve repulsion between particles. [35]

2.7 Analysis techniques

2.7.1 X-ray diffraction

The X-ray diffraction technique operates on the principle of crystals behaving like a diffraction grating when illuminated by X-rays. The diffraction depends on the crystal structure, more specifically on an interplanar spacing (explained below), denoted d_{hkl}, as well as the angle of incidence θ, equal to the angle of diffraction, of the incoming light. Diffraction intensities are only observed when there is constructive interference between the reflected X-rays. [23]

The condition for constructive interference is most easily explained using a figure, like the one below. The dots represent individual atoms and the lines mark the planes with common Miller indices hkl. The spacing between two planes with Miller indices hkl is d_{hkl}, mentioned earlier. These indices are used to denote different planes in a crystalline structure, whether it be the faces of a crystal or planes within the unit cell. The indices hkl are given to a specific plane depending on how many parts it divides the three dimensions a, b and c of the unit cell in. A plane which divides "a" into one part and is parallel to "b" and "c "would consequently be denoted 100. If this set of planes gives rise to constructive interference, the diffraction peak will share this notation, i.e 100. [23]

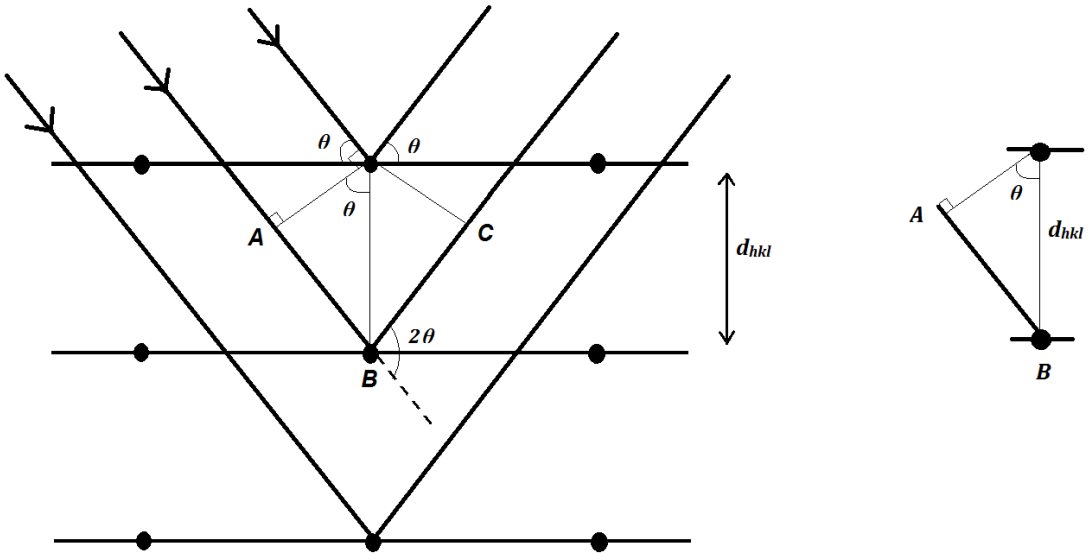

Figure 8. A figure showing the diffraction of incoming X-rays from three crystal planes with interplanar spacing d_{hkl}. The right-most figure shows an enlarged version of the part of the figure most relevant when deriving Bragg's equation through geometrical considerations.

As seen in the figure above, two parallel beams of X-ray radiation are scattered by two different atoms, lying on different planes with interplanar spacing d_{hkl}. The X-rays have an incident angle, θ, and for constructive interference to occur the reflected beams must be in phase. In order for that to happen, their

path length must differ by an integral number of the X-rays' wavelength. The path length difference, ΔL is given by: [23]

$$\Delta L = AB + BC \quad (7)$$

Both AB and BC can be expressed in terms of the diffraction angle θ and the interplanar spacing d_{hkl}:

$$\sin(\theta) = \frac{AB}{d_{hkl}} = \frac{BC}{d_{hkl}} \leftrightarrow AB = BC = d_{hkl}\sin(\theta) \quad (8)$$

From equation (7) and (8) it follows that:

$$\Delta L = AB + BC = 2d_{hkl}\sin(\theta) \quad (9)$$

Combining equation (9) with the fact that the path length difference must equal to an integral number of wavelengths, nλ, one arrives at the condition for constructive interference of X-rays by a crystalline solid, called the Bragg condition: [23]

$$n * \lambda = 2d_{hkl} * \sin(\theta) \quad (10)$$

2.7.2 Rietveld structure refinement

Although interpretation and extraction of structural parameter information from a well resolved diffractogram can be considered relatively straightforward, problems start to arise when there is significant peak overlap. The more complex the pattern, the harder it becomes to extract information about the sample as peak position, profile and other observables are more difficult to determine. A brilliant solution to this problem was found by H. M. Rietveld, who hypothesized that the overall diffraction profile could be fitted by a calculated profile from a structural model. If the calculated profile fits the experimentally observed diffraction profile, a good structural model has been achieved. The refinement part of this methods comes from the fact that the initial model must be refined until the calculated pattern replicates that which is observed. This is done by a least squares minimization procedure, minimizing the difference between observed and calculated intensities for each data point of the profile, according to equation (11):

$$M = \sum_i w_i\{y_i(obs) - y_i(calc)\}^2 \quad (11)$$

Where M is the function which is minimized, y_i(obs) and y_i(calc) are the observed and calculated intensities, respectively, of data point "i" and w_i is a weighting factor. The refinement is done through introduction of parameters describing different elements of the diffraction profile and letting their values vary until, ideally, the observed and calculated intensities converge or, more practically, until a set convergence criterion is reached. These parameters include: unit cell parameters, atomic positions and site occupancies, scale factor, profile parameters, background function etc. [36]-[39]

Although Rietveld refinement was originally only used for neutron diffraction data due to the completely Gaussian shape of the diffraction peaks, which simplifies peak profile modeling, it can also be applied to X-ray data. The main problem with using X-ray data compared to neutron data is the difficulty with which to model peak shape, which is typically not pure Gaussian in shape. The most common function to use for X-ray data is therefore the pseudo-Voigt function, which is a combination of Lorentzian and Gaussian components. [38], [39]

To begin a refinement one needs an initial structural model, i.e best guess values of crucial parameters such as unit cell symmetry, crystal space group and atomic positions and site occupancies. In addition, X-ray data consisting of many data points is needed in order to have many data points for which the calculated and observed values can be matched. Trying to refine a structure using non-satisfactory data will likely lead to a bad end result. Last but not least, angular limits and information about the used diffractometer is needed, such as wavelength data.

The success of the refinement can be evaluated using different approaches. Arguably the best, most convenient and visually appealing is the difference plot which plots the difference between the observed and calculated intensity for all data points and can give indications on what parameters that haven't been properly refined by showing characteristic patterns typical for a certain mismatch. A mismatch in peak profile is one example. Different, so called, R-values can also be used to represent the quality of the fit numerically. One of the most important R-values is that of R_{wp} defined as:

$$R_{wp} = \left[\frac{\sum_i w_i\{y_i(obs) - y_i(calc)\}^2}{\sum_i W_i\{y_i(obs)\}^2}\right]^{1/2} \qquad (12)$$

It should be noted however that these types of R-values must be used with caution. For example, there are two main tactics to handle the background in Rietveld refinement. Either, the background is estimated through interpolation and then subtracted, or it is included in the refinement through the use of a background function made up of refinable variables. Both approaches have advantages and disadvantages and can be used in different scenarios. However, if the background is large and not subtracted it will automatically produce a low R_{wp} value. This can easily be understood by studying equation (12). If the background is high, $y_i(obs)$ will be large and $y_i(calc)$ will, by modeling of the background, be similar in value to $y_i(obs)$ and so a high background will not really affect the numerator. The denominator however, will be heavily influenced by the high background as it doesn't include $y_i(calc)$. Consequently, the R_{wp} value will practically always display a low value for high background samples leading to false conclusions on the fitting. [36]-[39]

Heeding this word of caution, the R_{wp} value can be further compared with what is called the expected R-value, R_{exp}, which can be said to give an indication of the data quality. R_{exp} is defined as:

$$R_{exp} = \left[\frac{(N-P)}{\sum_i^N w_i\{y_i(obs)\}^2}\right]^{1/2} \qquad (13)$$

Where N is the number of observations and P is the number of parameters. The ratio between R_{wp} and R_{exp} has been given its own variable, χ^2, which is judged to give a good indication of the fit. Ideally, χ^2, should approach 1 but can take on smaller or larger values depending on data collection. [38]

2.7.3 Thermogravimetric analysis and differential scanning calorimetry

Thermogravimetric analysis, or TGA, is a relatively straightforward characterization technique. The mass change of a sample is monitored as the temperature changes and can be plotted as a function of time or temperature. [40]

Differential scanning calorimetry, or DSC, measures the changes in a sample's heat capacity as a function of temperature by monitoring the heat flow in and out of the sample, resulting from e.g phase transitions etc, and comparing them with a reference. [41]

2.7.4 Scanning electron microscopy

Scanning electron microscopy, or SEM, utilizes electrons to characterize structural features of a sample surface down to fractions of nanometers in size. It can be used to analyze microstructure, chemical composition and crystal orientations for example. The basic principle behind the technique is that electrons are ejected from an electron gun and focused to a beam with the aid of magnetic lenses. The interactions between the beam and sample surface include elastic and inelastic scattering of electrons giving rise to backscattered and secondary electrons, respectively, which can give complementary information about the sample. [42], [43], [44]

2.7.5 Impedance spectroscopy

There are different forms of opposition against the motion of charge carriers such as electrons or protons, termed resistance and reactance where the latter can be further subdivided into capacitance and inductance. Impedance is a term encompassing all these forms of opposition. It can be seen as an extension of the concept of resistance to more complex circuits, containing other elements than only ideal resistors. This is especially useful for circuits employing alternating current as they typically contain elements such as capacitors, with a charge opposing capacitance, which are not used in direct current circuits since they are detrimental to their function. [45], [46], [47], [48], [49]

The impedance, Z, is expressed in terms of its magnitude, $|Z|$, and a term called the phase shift, ϕ. The phase shift refers to the difference in phase between an applied voltage and the resulting current. Both capacitance and inductance give rise to a 90^o phase shift of the voltage with respect to the current while resistance does not cause a phase shift, i.e a shift of 0^o. The impedance, encompassing all types of charge opposition, produces a voltage phase shift between 0^o and 90^o. By mathematical manipulation the impedance can be expressed in complex form, with a real and imaginary part, according to equation (14) below. [47], [49], [50]

$$Z(\omega) = Z_{re} + jZ_{im} = |Z(\omega)|\cos(\phi) + j|Z(\omega)|\sin(\phi) = |Z(\omega)|[\cos(\phi) + j\sin(\phi)] \quad (14)$$

Where Z_{re} and Z_{im} is the real and imaginary part, respectively. The reason that impedance is written as a function of frequency and not time is explained below. By using the fact that impedance can be expressed in complex form, data can be plotted in Nyquist diagrams and Bode plots. It follows from equation (14) that when the phase angle is zero, the expression for impedance simplifies to:

$$Z(\omega) = Z_{re} \quad (15)$$

I.e impedance is only real for a phase shift of zero. As has been mentioned, the only charge impeding part of impedance giving rise to zero phase shift is the resistance. In other words, resistance makes up the real part of impedance. [49], [50]

For solid electrolyte materials, impedance is usually measured by applying a known current or voltage to a cylindrical sample via two electrodes in contact with the faces of the sample. The resulting voltage or current is then measured across a wide range of frequencies. Different atmospheres can be used, such as argon, oxygen, vacuum or water vapor, depending on the experiment and what is to be investigated. The sample response to the electrical stimulus depends on both external factors such as the atmosphere or temperature and internal or material factors, such as the microstructure. The response of a complex system, including capacitive and inductive elements, to an applied electrical signal can be represented by an equally complex system of time-dependent equations describing the behavior of these elements. By Fourier transformation these equations can be simplified by transformation into the frequency domain, which alleviates the problems of overburdening mathematical complexity. Impedance can therefore be described in the frequency domain and can be measured as a function of frequency, as is often done. [49]

Looking at the Nyquist diagram below, one can get an indication of the information that can be extracted from an impedance measurement.

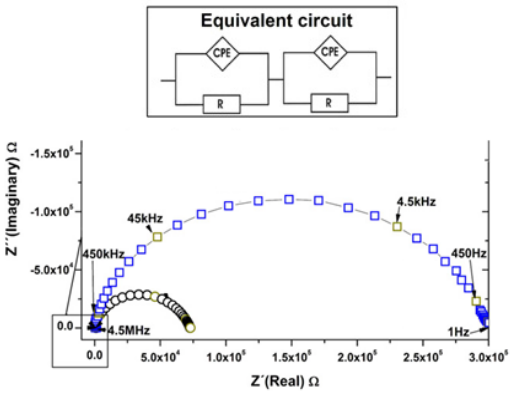

Figure 9. A schematic figure showing the typical appearance of a impedance spectroscopy Nyquist diagram. This specific diagram is from an analysis, in another study, performed on a $BaTi_{0.5}In_{0.5}O_{3-\delta}$ sample. Adapted from [6] with permission.

The behavior of the material may be modeled by an equivalent circuit, containing different elements such as capacitors and resistors, which can fit the observed data. The different circuit elements should all be related to physiochemical characteristics of the material so that specific system responses, such as a display of a high capacitance at high frequencies, for example, can be correlated to a property of the system, such as grain boundary conduction. By performing the experiment at different temperatures, a multitude of semicircles will be displayed, like those in the figure above, due to different system responses a different temperatures. By taking the right-most x-axis intercept (i.e not the origin intercept) of these semicircles values for the resistance can be collected and the corresponding conductivity plotted against temperature. [49], [50]

As has been mentioned previously, proton conduction generally reaches a maximum at a specific temperature and then decreases with temperature. There are other species that can be conducted through oxygen deficient perovskites however, namely electron holes (p-type conduction) and oxide ions. The conduction of these species generally increases with temperature and contribute to the total conductivity which could lead to false conclusions regarding proton conductivity at high temperatures. A way to avoid this is to employ methods to firstly confirm the existence of proton conduction in the material and secondly to separate it from the conductivity contributions of other species. One method is to, through impedance spectroscopy, study the so called isotope effect where the protons are replaced by deuterons in the material. Deuterons are heavier than protons and therefore have a lower frequency of oscillation between oxygen atoms during conduction which in turn leads to a decrease in the conductivity. This method can be used to verify the existence of proton conduction because the difference in conductivity can be measured by impedance spectroscopy. Further confirmation of material protonation can be done by performing TG analysis in order to study mass losses of water that can confirm the existence of protons in the material. To differentiate between proton conduction and other types of conduction, the conductivity can be measured by impedance spectroscopy in different atmospheres, during both heating and cooling cycles. A dry atmosphere should result in the material exhibiting a lower conductivity than it would in a wet atmosphere as the wet atmosphere increases the amount of protonic defects in the material, as previously seen in equation (4) and as illustrated in figure 10 below. [6], [18], [24]

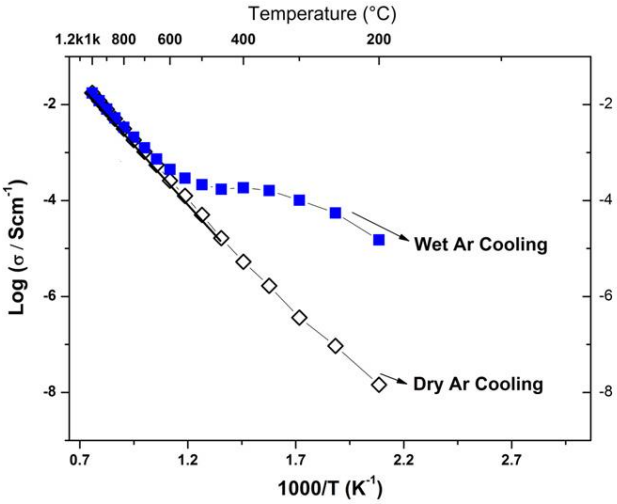

Figure 10. An illustrative plot of the temperature dependence of the total conductivity of a proton conducting material during cooling in two different atmospheres, dry and wet argon. Notice that the conductivity of the material in the wet atmosphere is orders of magnitude higher than in the dry atmosphere. This specific plot is from an analysis performed on a $BaTi_{0.5}In_{0.5}O_{3-\delta}$ sample. Adapted from [6] with permission.

The material should also exhibit a characteristic conductive behavior leading to a higher conductivity a low temperatures during the first heating cycle than during the subsequent cooling cycle, at low temperatures, in a dry atmosphere. This is because during the heating cycle, the material is usually partly hydrated and proton conduction is possible, while in the following cooling cycle the material has become dehydrated as it has gone through the heating cycle. The conductivities at higher temperatures should be virtually identical for the heating and cooling cycle because the sample is then dehydrated in both cases. This behavior is illustrated in figure 11 below. [6], [18]

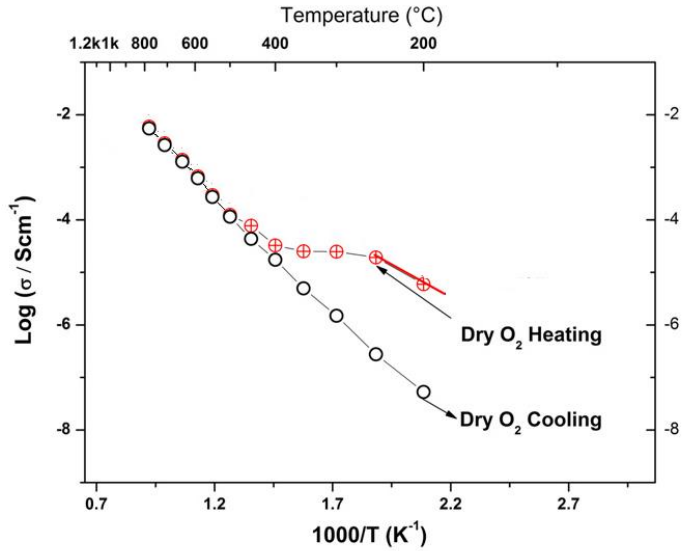

Figure 11. An illustrative plot of the temperature dependence of the total conductivity of a proton conducting material during heating and cooling in a dry oxygen atmosphere. Notice that the conductivity of the material during heating is orders of magnitude higher than during cooling, at low temperatures, but identical at higher temperatures. This specific plot is from an analysis performed on a $BaTi_{0.5}In_{0.5}O_{3-\delta}$ sample. Adapted from [6] with permission.

As can be seen in the figure above, conductivity can be measured in different atmospheres besides argon when using impedance spectroscopy. The reason for studying conductivity under an oxygen atmosphere, and not only under an inert argon atmosphere, is to examine the p-type contribution to conductivity using impedance spectroscopy. As the partial pressure of oxygen increases, the amount of electron holes and their contribution to the total conductivity should increase, as can be seen in equation 16 below. [6], [24]

$$V_o^{\cdot\cdot} + \frac{1}{2}O_2(g) = O_o^x + 2h^{\cdot} \qquad (16)$$

Where $V_o^{\cdot\cdot}$ is a doubly positive vacancy situated at an oxygen site, O_o^x is an oxygen atom of neutral charge situated at an oxygen site and $h^{\cdot}$ is an electron hole. It can be seen from equation 16 that if the oxygen partial pressure increases, the number of oxygen vacancies decreases and so equation 16 is in competition with the reaction described by equation 4. In other words, a high oxygen partial pressure will favor p-type conduction over proton conduction. [6], [24]

3. Experimental method

The synthesis and characterization of the four sets of barium titanate based samples is described below.

3.1 Synthesis method

Four sets of samples were synthesized using the standard solid state reaction and sintering technique. The first set consisted of one scandium doped and one indium doped barium titanate sample with the chemical formulas $BaTi_{0.3}Sc_{0.7}O_{3-\delta}$ and $BaTi_{0.3}In_{0.7}O_{3-\delta}$, hereafter denoted T-BTS70 and T-BTI70. These samples were "trial samples" (hence the T-prefix) used for finding a suitable synthesis route that would yield phase pure materials and for observing what relative densities that could be achieved without further measures.

Another set, the second one of the four, also consisted of one scandium doped and one indium doped sample with the same chemical formulas as above. These samples were synthesized after a satisfactory synthesis route had been found for the first set of samples, for the purpose of using them in ceramic processing techniques to investigate the impact on sample density. These samples are hereafter denoted P-BTS70 and P-BTI70 (P for processing). The processing steps were to be performed before the samples had reached a "dead" state, i.e with no more potential for sintering, but after the samples were deemed pure enough. This was decided because it was hypothesized that the effects of the ceramic processing steps wouldn't be as great if the material could not sinter properly afterwards. At the same time, the material had to be pure enough so that any increase in density could actually be correlated to the perovskite part of the material and not to a large impurity phase. The P-BTI70 sample reached this stage after heating 2, at 1200°C, and so no further sintering steps were done before densification while the P-BTS70 sample reached an acceptable purity after sintering at 1400°C. Two batches of these materials were made. Initial analysis of the first batch revealed that processing route 2 yielded the most promising

results and so a second batch was made to focus exclusively on this route in order to provide more material for further analysis. The ceramic processing steps will be described in detail later on.

The remaining two sets of samples were synthesized in order to investigate how manipulation of the basic chemical formulas of the first set of samples would affect the density and sintering behavior. One of these sets incorporated both scandium and indium in the same sample, with two different ratios, their chemical formulas being $BaTi_{0.3}Sc_{0.35}In_{0.35}O_{3-\delta}$ and $BaTi_{0.3}Sc_{0.5}In_{0.2}O_{3-\delta}$ hereafter denoted BTSI35 and BTSI50 (the number corresponds to the fraction of scandium). The reasoning behind this was that in the synthesis of the first set of samples, the indium doped variant was much easier to purify, i.e the pure perovskite phase formed at a relatively low temperature, 1400°C. The scandium doped sample however proved a much greater challenge and would not achieve phase purity even at 1550°C. By introducing indium it was thought that the sample could achieve phase purity at a temperature lower than 1550°C. In addition, the lower melting point of indium compared to scandium could help the sintering and thereby the densification, see table 1 below.

The last set of samples incorporated tin by substitution of a fraction of titanium in the structure, the reasoning behind this being that the low melting point of tin might help the sintering of particles during heat treatment, yielding a denser material, see table 1 below. In addition, it was thought that it might improve the hydration characteristics. The chemical formulas of the samples were $BaSn_{0.15}Ti_{0.15}Sc_{0.7}O_{3-\delta}$ and $BaSn_{0.15}Ti_{0.15}In_{0.7}O_{3-\delta}$, hereafter denoted BSTS70 and BSTI70.

Table 1. A list of the melting points of all reactants used during synthesis. All melting points are taken from the manufacturer information on the corresponding container (see next table for reactant information including manufacturer).

Compound	*Melting point (°C)*
$BaCO_3$	811
TiO_2	1825
Sc_2O_3	2485
In_2O_3	1910
SnO_2	1630

The same reactant powders were used for synthesis of all samples, except tin oxide which was naturally only used for the BSTS70 and BSTI70 samples. Information regarding the reactants used for synthesis can be found in the table below.

Table 2. Information regarding purity, manufacturer and batch number for the reactant powders used for synthesis of the different sets of samples.

Reactants used for synthesis				
Reactant	**Purity**	**Manufacturer**	**Batch/lot nr.**	**Used for (samples)**
$BaCO_3$	99.8 %	Alfa Aesar	H30X028	All
TiO_2	99.8 %	Sigma-Aldrich	MKBQ4471V	All
Sc_2O_3	99.9 %	Alfa Aesar	E11Y025	T-BTS70/P-BTS70/BSTS70/BTSI35/BTSI50
In_2O_3	99.99 %	Sigma-Aldrich	MKBL5705V	T-BTI70/P-BTI70/BSTI70/BTSI35/BTSI50
SnO_2	99.9 %	Sigma-Aldrich	07112BH	BSTS70/BSTI70

The synthesis procedure for all sets of samples was very similar and originated from the first draft that emerged during synthesis of the first set of samples, T-BTS70 and T-BTI70. The first step was weighing of stoichiometric amounts of the reactants, on a metal basis. The reactants were not dried before weighing. After weighing, the powders were mixed and ground in a mortar with sporadic addition of ethanol as needed for improved homogenization. The ethanol was then allowed to evaporate where after the powder mixture was weighed. Following this initial mixing of reactants, the samples were subjected to a stepwise synthesis procedure involving heating, grinding and pressing of the powders into pellets.

The mixing and grinding times for the first set of samples and the tin samples were identical. However, when synthesizing the mixed Sc/In samples and the samples used for ceramic processing the reactant mixing time was increased from 15 min to 20 min and the grinding times after each heating was increased from 10-15 min to 25 min.

All samples were placed in alumina crucibles and subjected to thermal treatments at different temperatures in both box and tube furnaces, from Entech and Lenton Thermal Designs respectively, as the synthesis proceeded. The heating steps are summarized in table 3 below. Before every heating, except the first, the powders were pressed into cylindrical pellets of 13 mm diameter using a manual M30 press from Research and Industrial Instruments Company (England) and approximately 150 MPa of pressure, to aid sintering. The pellets were weighed and their dimensions measured before and after each sintering. The dimensions were measured using a Cocraft Digital Caliper to get precise dimensions for density calculations. All sintering steps were performed in succession in the order that they are displayed in the table below.

Table 3. A summary of essential features for the heating/sintering steps performed during synthesis and phase purification. Manufacturer of the

Heat treatment	Performed on (sample)	Target temperature (°C)	Target dwell (hours)	Ramp up (°C/min)	Ramp down (°C/min)	Furnace type
1	All	1000	12	3	5	Box furnace
2	All	1200	12	5	5	Box furnace
3a*[1]	All	1400	20	5	5	Tube furnace
4a	T-/P-BTS70 /T-BTI70 /BSTS70	1500	20	2.5	2.5	Tube furnace
4b	T-BTS70 /BSTS70	1500	20	2.5	2.5	Tube furnace
5	T-BTS70 /BSTS70	1550	24	5	5	Tube furnace

* [1] There was a second 1400°C treatment, referred to as 3b in this report, performed only one time on a BTI70 sample because phase purity hadn't been achieved in that case. This sample will be referred to as T-BTI70 (batch 2).

The set of samples that were to undergo ceramic processing, P-BTS70 and P-BTI70, were synthesized in the way that has been described with one big difference; for the P-BTI70 sample, ceramic processing took place in between heating 2 and 3a (see table above) and for P-BTS70 between heating 3a and 4a. The processing techniques used for the first batch were ball milling, cold isostatic pressing and slipcasting, i.e processing route 1, 2 and 3 in figure 3, while for the second batch only route 2 was employed. The samples of the first batch were divided into three subsets according to the processing they went through, see table below. The first subset, which only went through CIP, consequently has the prefix CIP- and suffix –D because it was pressed in a dry state. The second subset, which was ball milled in addition to isostatic pressing, has the suffix –W as these samples were isostatically pressed while wet with ethanol from the ball milling. The third and last subset has the prefix SC- as it was the only one subjected to slipcasting. As has been mentioned, the second batch was subjected to ball milling and CIP and so its samples will be denoted in the same way as those from batch 1 that underwent the same treatment, with and added "(b.2)" at the end of the sample name.

Table 4. A table showing the division of the P-BTS70 and P-BTI70 samples into subsets, classifying each subset according to the ceramic processing techniques it was subjected to.

	Subset nr.	Sample	Ball milling	Cold isostatic pressing	Slipcasting
Batch 1					
	1	CIP-BTS70-D/CIP-BTI70-D	No	Yes	No
	2	CIP-BTS70-W/CIP-BTI70-W	Yes	Yes	No
	3	SC-BTS70/SC-BTI70	Yes	No	Yes
Batch 2					
	1	CIP-BTS70-W (b.2) /CIP-BTI70-W (b.2)	Yes	Yes	No

All isostatic pressing was done using a press from Avure Autoclave Systems and 400 MPa of pressure, using water as the pressurized medium, which was held for 30 seconds. Before the isostatic pressing, the sample powder was pre-pressed into a cylindrical pellet of 12 mm diameter. This was done using a manual press from NIKE Hydraulics and approximately 150 MPa of pressure where after the sample pellet was vacuum packed in a balloon to protect it from the water during subsequent isostatic pressing.

The ball milling was done in two subsequent steps. First the samples were ball milled at 200 rpm for one hour in a Retsch PM 400 planetary ball mill in approximately 3 ml of ethanol (50% ethanol and 50% sample powder, by volume) and then ball milled further overnight at 50 rpm on a roller ball mill from Heynau, again in ethanol. 30 g of 5 mm diameter zirconia balls were used for both ball milling sessions. Following this, the formed slurry was allowed to dry in an oven at 40°C until it had formed a thick paste. This paste was subsequently pressed in the same manner as described above, producing pellets of CIP-BTS70-W and CIP-BTI70-W. Note that for batch 1, some of the slurry was not CIP:ed and instead used for slipcasting, see below.

Most of the ball milled slurry was used for the slipcasting process, producing subset 3 of batch 1. Hollow plastic cylinders were placed on a plaster brick and filled to the top with slurry. Thereafter a lid was placed on top to ensure a slow and steady drying of the slurry through absorption of ethanol by the plaster, avoiding rapid ethanol evaporation. Small amounts of the slurry were continuously added to the cylinder until all the slurry had been used. It was then allowed to dry completely overnight forming two pellets, SC-BTS70 and SC-BTI70, by sedimentation of the solid material.

3.1.1 Hydration of samples

Hydration was carried out in a custom setup, using an Entech tube furnace connected to a heated flask of water through which nitrogen gas was bubbled. The water was kept at a temperature of 60°C, corresponding to an approximate water vapor pressure of 20 kPa, or 0.197 atm. The temperature in the oven was ramped up 3.3°C/min to 800°C where it dwelled for 2 hours. The temperature was then ramped down 3.3°C/min, in steps, dwelling for 2 hours each at the temperatures 600°C, 400°C and 200°C until it was finally ramped down to 150°C and held there until the samples were removed from the oven.

3.2 Characterization methods

Characterization of the synthesized samples was done by powder X-ray diffraction, impedance spectroscopy, thermogravimetric analysis and scanning electron microscopy. The principles behind these techniques and how they were used in this study are described below.

3.2.1 Powder X-ray diffraction

The powder X-ray diffraction measurements were performed using a D8 Vario Advance Diffractometer from Bruker AXS utilizing a copper X-ray source and a germanium monochromator to produce $K\alpha_1$ X-rays of wavelength 1.54056 Å. The phase purity was checked after each sintering/grinding cycle using a short 20 minute scan in the 2θ range 20°-60° with 0.05° increments. To get data for Rietveld refinement a long 10 hour scan in the 2θ range 20°-100° was done with 0.01° increments. Rietveld refinement was performed on two samples, CIP-BTI70-W and CIP-BTS70-W using the program GSAS. Structure data thus obtained was then imported into the program VESTA for visualization of the crystal structure.

3.2.2 Impedance spectroscopy

Impedance spectroscopy was performed using a ProboStat measurement cell from NorECs, Norway connected to a Solartron 1260 impedance spectrometer. Measurements were performed on one 11-12 mm diameter wet-pressed CIP pellets of BTI70 and two similar pellets of BTS70 which had been pre-painted on both sides using a Pt ink (Pt ink 6926, Metallor, UK). The painted area was approximately 8 mm in diameter. The impedance was measured in three separate stages. The first stage was measurement during a heating-cooling (HC) cycle in dry argon. The second stage was measurement during cooling in wet argon and the third stage measurement during cooling in dry argon. The temperature interval used for all three stages was 150-1000°C and the frequency range employed was 100mHz to 6MHz. The program Z-View was used to view and fit the obtained data. The equivalent circuit used to evaluate the data consisted of a resistance and a constant phase element in parallel, further connected in series to another parallel resistance and constant phase element.

3.2.3 Thermogravimetric analysis and differential scanning calorimetry

TGA and DSC was performed using a STA 409 PC Luxx combined differential scanning calorimeter and thermo gravimeter from NETZSCH. Between 100-150 mg of samples was used for each TG run and placed in an alumina crucible. The analysis was performed in a nitrogen atmosphere with a flowrate of 20 ml/min. The measurement chamber was heated from room temperature to 1000°C at a rate of 15°C/min and held at this temperature for 30 minutes before termination.

3.2.4 Scanning electron microscopy

Scanning electron microscopy was done on the surface and fracture surface of a wet isostatically pressed BTI70 and BTS70 pellet using a Phenom ProX desktop SEM utilizing a 10 kV accelerating voltage and pin stub charge reduction sample holder for non-conducting samples.

4. Results

Results from synthesis, densification and characterization of the different samples are presented in the following sections.

4.1 X-ray diffraction and structure analysis

A description of the results obtained by X-ray diffraction is presented below.

4.1.1 XRD on T-BTS70 and T-BTI70

For all four sets of synthesized materials, when looking at the 2θ-range of 20-60°, the perovskite phase can be identified by the peaks at the approximate 2θ values of 21°, 30°, 37.5°, 43°, 49° and 53.5°, corresponding to d-spacing values of 4.225, 2.975, 2.395, 2.100, 1.857 and 1.711 Å. Depending on chemical modification of BTI70 and BTS70, the perovskite peaks may shift position to slightly higher or lower d-spacings, as is the case for the tin and mixed Sc/In samples. This is discussed further at a later stage.

X-ray scans of T-BTI70 sample revealed a progressively purer perovskite phase as the sintering temperature increased. This can be seen in figure 21 below, where the diffraction patterns obtained after each sintering step are stacked on top of each other to show the progression of the perovskite development. The most dramatic change towards a pure perovskite phase seems to happen during sintering at 1200°C, with an improvement seen at 1400°C. It should be noted that during firing at 1500°C the T-BTI70 pellet had melted and reacted with the crucible, thereby destroying the sample. Some material could be scraped off and an XRD analysis revealed a multitude of phases comprised of mixed species from both the sample and the alumina crucible.

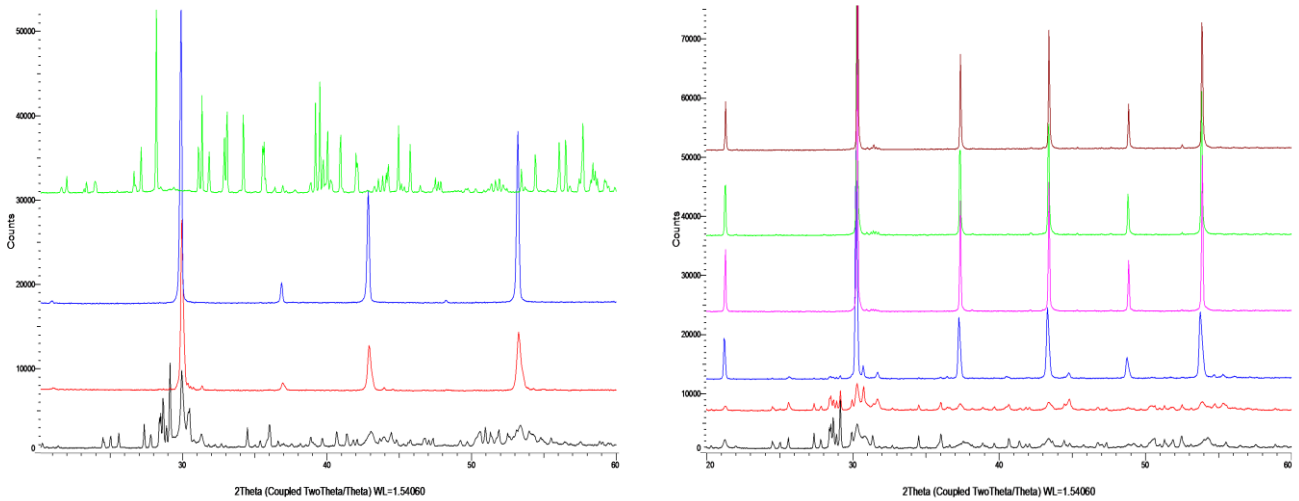

Figure 12. X-ray diffractograms of the T-BTI70 sample (left) and T-BTS70 sample (right), sintered at different temperatures. From bottom to top, BTI70 was sintered at 1000°C, 1200°C, 1400°C and 1500°C while BTS70 was sintered an additional time at 1500°C and once at 1550°C. Note that the sintering of BTI70 at 1500°C caused a reaction between the sample and crucible, which explains the sudden appearance of a multitude of peaks.

Similarly to the T-BTI70 sample, the T-BTS70 sample displayed increased perovskite phase purity after each successive heating. In contrast to the T-BTI70 sample however, the T-BTS70 sample did not melt or react with the crucible at 1500°C. Instead, the phase purity increased compared to the 1400°C sample as seen in the figure above. A second heating at 1500°C did not eliminate the remaining impurities, identified partially as the barium deficient barium scandium oxide $BaSc_2O_4$, and neither did the following sintering at 1550°C. The impurities can be seen just to the right of the highest intensity peak, at a 2θ-angle of roughly 31-32° in figure 12 above.

4.1.2 XRD on BSTS70 and BSTI70

The development of the perovskite phase for the Sn-containing BSTI70 sample followed a similar path to the T-BTI70 sample as can be seen in the left part of the figure below. The most drastic change seems to take place at 1200°C, with improvements in perovskite phase purity when sintered at 1400°C.

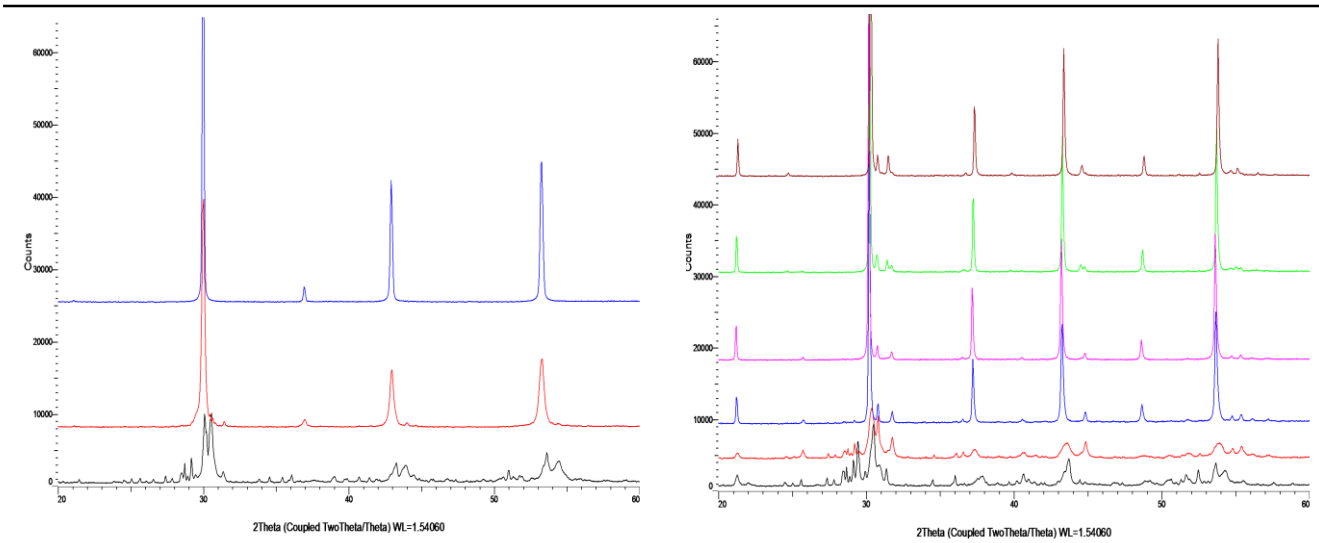

Figure 13. X-ray diffractograms of the two tin containing samples, BSTI70 (left) and BSTS70 (right), sintered at different temperatures. From bottom to top the BSTI70 sample was sintered at 1000°C, 1200°C and 1400°C while the BSTS70 samples was also heated two times at 1500°C and once at 1550°C.

The perovskite phase development of the BSTS70 sample shows many similarities to that of the T-BTS70 sample. The two samples seem to follow a similar path up until the first 1500°C heating, where the T-BTS70 sample purity starts improving much more than that of the BSTS70 sample, se figure above. Phase identification revealed the persistent impurity peaks of the BSTS70 sample to be barium deficient scandium oxides, such as $BaSc_2O_4$ and $Ba_3Sc_4O_9$. The impurity peaks are clearly visible in the same 2θ-range as for T-BTS70, i.e between 31-32°.

The results of the XRD can also be used to confirm the incorporation of tin in the perovskite structure. This can be done by examining the peak shift of the BSTS70 and BSTI70 samples compared to the peak positions of the T-BTS70 and T-BTI70 samples. For clarity, a zoomed-in part of an X-ray diffractogram is shown in Figure 25 below, illustrating this shift for two different peaks at the approximate 2θ-values 43.1 and 53.5°.

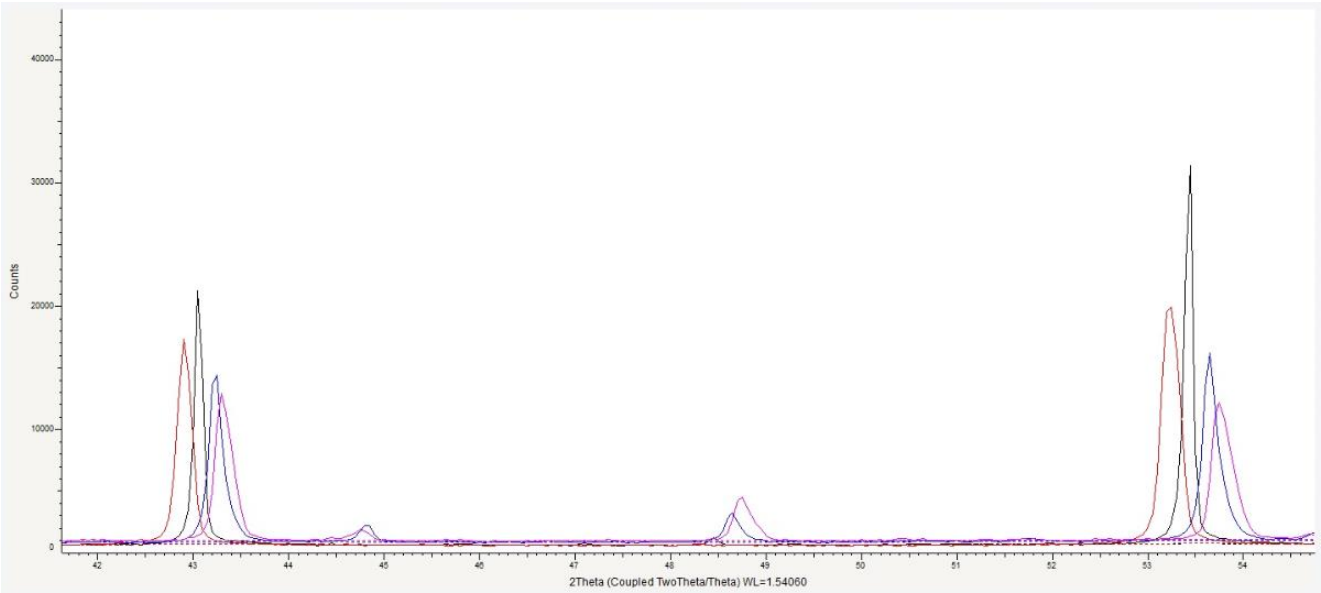

Figure 14. A zoomed-in X-ray diffractogram of the trial and tin containing samples sintered at 1400°C. BSTI70 = red line, T-BTI70 = black line, BSTS70 = blue line and T-BTS70 = pink line. Note the shift towards lower θ-values (higher d-spacing) for the samples with tin compared to those without, as well as the lower θ-values of the indium samples compared to the scandium samples.

As can be seen in figure 14, the BSTS70 and BSTI70 samples (blue and red lines) have peaks shifted towards lower 2θ-values in relation to the T-BTS70 and T-BTI70 samples (pink and black lines). Also visible is the shift of indium-substituted samples towards lower 2θ-values compared to scandium substituted ones. This can be explained by studying the table below. First and foremost, one can see that replacing titanium with tin in the structure will most likely increase the unit cell dimensions, and hence the d-spacing, since the ionic radius of Sn^{4+} is larger than that of Ti^{4+}. The peaks of a tin-substituted sample should therefore be shifted to lower 2θ-values compared to a non-tin-substituted one, which is what is observed. In addition, replacing scandium with indium in the structure should lead to a peak downshift as the radius of indium is larger than that of scandium causing an increase in unit cell size and d-spacing, with a lowering of the 2θ-values. This is also what is observed, as the T-BTI70 and BSTI70 sample peaks are shifted to lower 2θ-values in respect to those of T-BTS70 and BSTS70.

Table 5. A table displaying the ionic radii of the elements present in the assorted samples previously described. The oxidation and coordination numbers are included to avoid confusion as the ionic radii depend on their values. [51]

Element	Oxidation number	Coordination number (in the perovskite)	Ionic radius
Ba	2+	12	1.61 Å
Ti	4+	6	0.605 Å
Sn	4+	6	0.690 Å
Sc	3+	6	0.745 Å
In	3+	6	0.800 Å
O	2-	6	1.40 Å

4.1.3 XRD on BTSI35 and BTSI50

The figure below belongs to the BTSI35 and BTSI50 samples which show a remarkable improvement in phase purity at 1400°C compared to any BTS70-based sample, despite their relatively high scandium substitution levels. The materials can be considered phase pure at this temperature and can therefore be said to display a perovskite phase development behavior more akin to the BTI70-based samples.

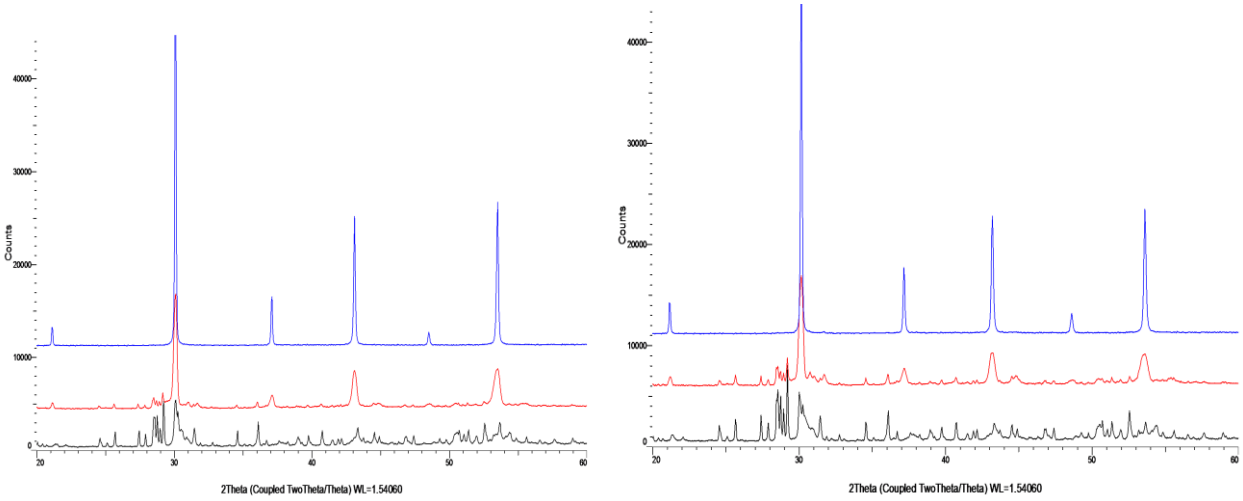

Figure 15. X-ray diffractograms of the two hybrid Sc/In samples, BTSI35 (left) and BTSI50 (right), sintered at different temperatures. From bottom to top, both samples were sintered at 1000°C, 1200°C and 1400°C.

Trying to confirm the presence of both indium and scandium in the mixed Sc/In samples, using the same thought process as when confirming tin incorporation, one can look at the ionic radii of scandium and indium. The larger radius of indium will lead to a larger unit cell and d-spacing, consequently leading to lower 2θ-values.The less indium present in the perovskite, instead substituted with the smaller scandium atoms, will lead to a gradual upshift of the diffraction peaks, which can clearly be seen in the figure below.

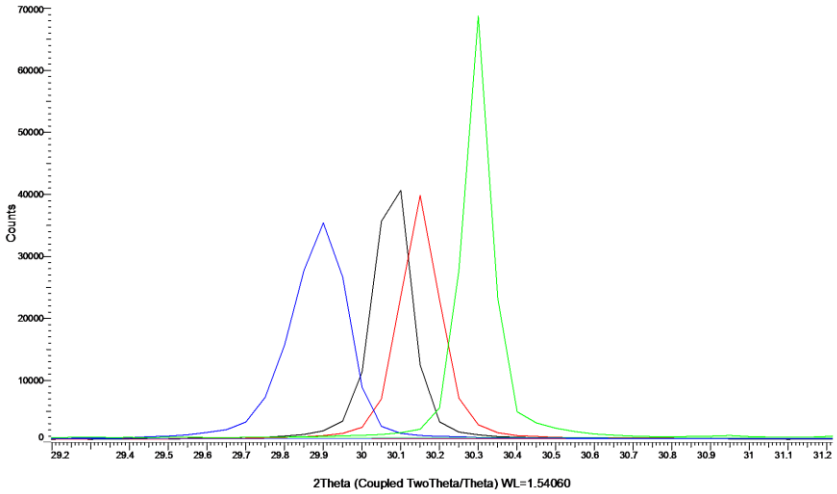

Figure 16. A zoomed in X-ray diffractogram of the trial and mixed Sc/In samples sintered at 1400°C. T-BTI70 = blue line, BTSI35 = black line, BTSI50 = red line and T-BTS70 = green line. Note the increasing 2θ angles with increasing scandium content and decreasing indium content.

4.1.4 XRD on isostatically pressed BTS70 and BTI70

The results from performing XRD on the CIP samples, see figure below, show that both the CIP-BTI70-D and CIP-BTI70-W sample were phase pure after sintering at 1400°C. Comparing this to the results of T-BTI70, it cannot be said with any certainty if the ceramic processing aided the formation of a pure perovskite as T-BTI70 also achieved phase purity at the same temperature.

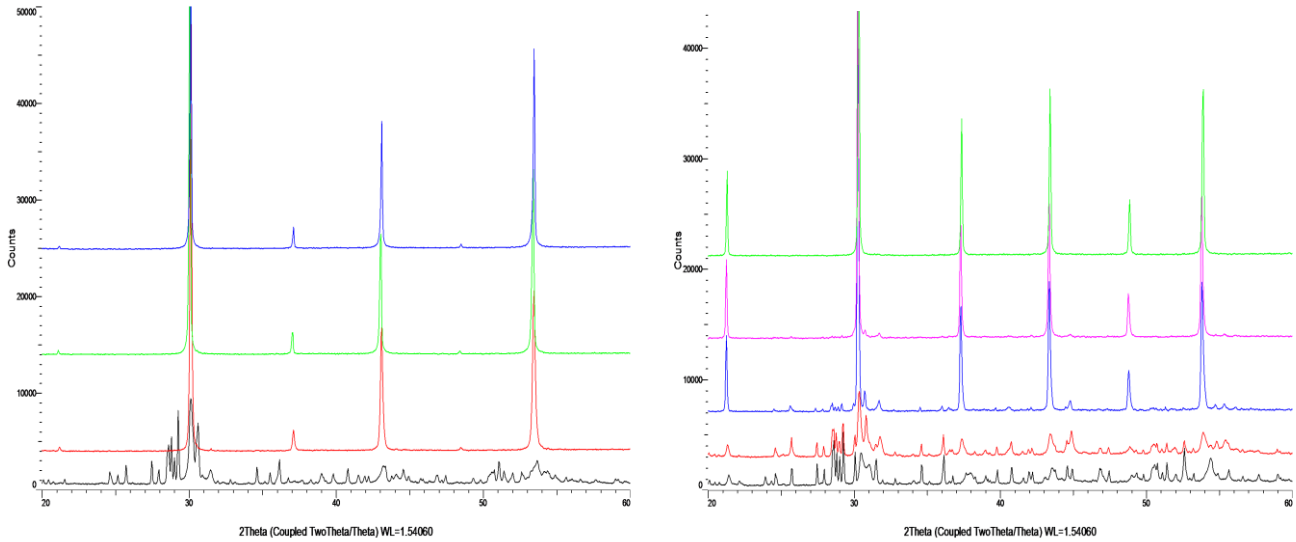

Figure 17. X-ray diffractograms of the CIP-BTI70 (left) and CIP-BTS70 (right) samples sintered at different temperatures. From bottom to top the the CIP-BTI70 sample was sintered at 1000°C, 1200°C, 1400°C (pressed dry, CIP-BTI70-D) and 1400°C (pressed as a wet paste, CIP-BTI70-W) while CIP-BTS70 was sintered at 1000°C, 1200°C, 1400°C, 1500°C (pressed dry, CIP-BTS70-D) and 1500°C (pressed as a wet paste, CIP-BTS70-W). Note that no ceramic processing took place until before the final sintering at 1400 and 1500°C, respectively.

In the case of the CIP-BTS70 samples, see figure above, the cold isostatic pressing of the wet CIP-BTS70 sample seems to have had a profound impact on the perovskite phase development. In contrast to the T-BTS70 sample, the CIP-BTS70-W sample has formed the pure perovskite after just one sintering at 1500°C. T-BTS70 was not pure even after two sinterings at 1500°C and one at 1550°C. CIP-BTS70-D, however, did not display the same success as CIP-BTS70-W and has a phase development more akin to the T-BTS70 sample.

4.1.5 XRD on slipcasted BTS70 and BTI70

The perovskite development of the slipcasted samples doesn't differ in any significant way to that of the trial samples. Examining the diffractograms of SC-BTI70, the only difference seems to be that phase purity is achieved at 1200°C. Since the samples weren't slipcasted until just before the 1400°C sintering, this can only be attributed to better sample preparation leading up to the 1200°C sintering compared to the preparation of the trial samples.

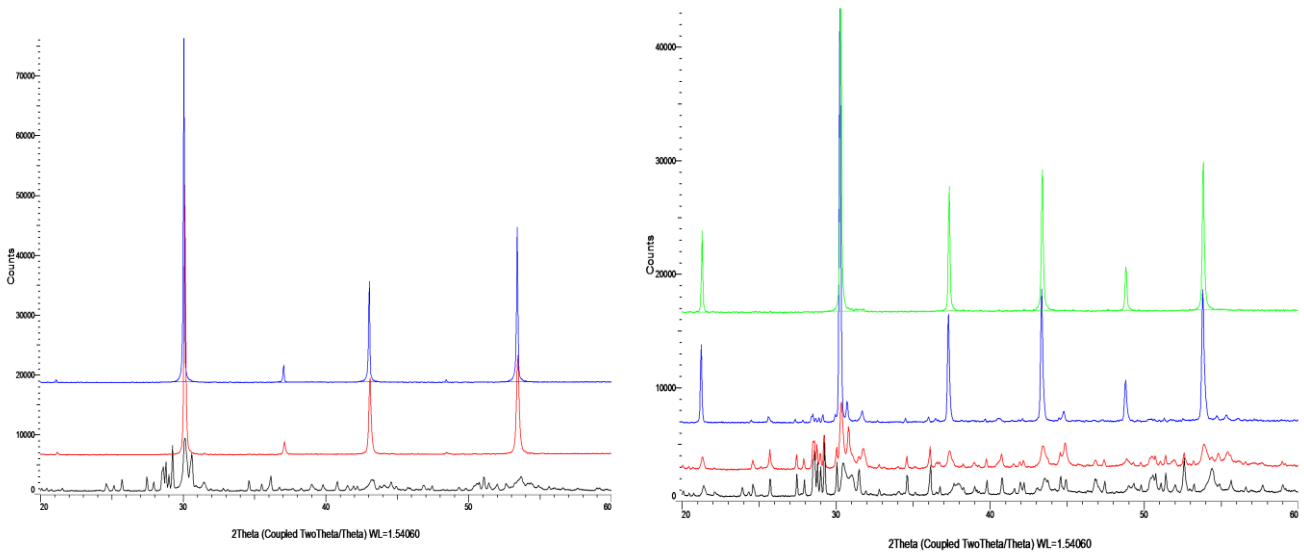

Figure 18. X-ray diffractograms of the slipcasted SC-BTI70 (left) and SC-BTS70 (right) samples, sintered at different temperatures. From bottom to top the SC-BTI70 sample was sintered at 1000°C, 1200°C and 1400°C while SC-BTS70 was also sintered at 1500°C. Note that no ceramic processing took place until just before the final sintering at 1400°C and 1500°C, respectively.

The appearance of the X-ray diffractograms belonging to SC-BTS70 is more or less identical to that of T-BTS70. It is worth noting that the combination of ball milling and slipcasting (processing route 1), unlike ball milling and cold isostatic pressing (processing route 2), did not help BTS70 achieve phase purity when sintered at 1500°C. This will be considered in greater detail in the discussion section.

4.1.6 XRD on hydrated samples

Small amounts of all four sets of samples were hydrated using the hydration oven detailed in the experimental method section. By examining the XRD patterns of the BTI70 based samples, see figure below, it can be said that when purposefully hydrated the structure of all BTI70-based samples transformed from a cubic to a tetragonal perovskite. Although these patterns have not been properly indexed for this study, a material almost identical to BTI70, namely $BaTi_{0.2}In_{0.8}O_{3-\delta}$, has been reported to adopt a tetragonal structure upon hydration, displaying an almost identical diffraction profile as the ones seen below. For comparison, see [54].

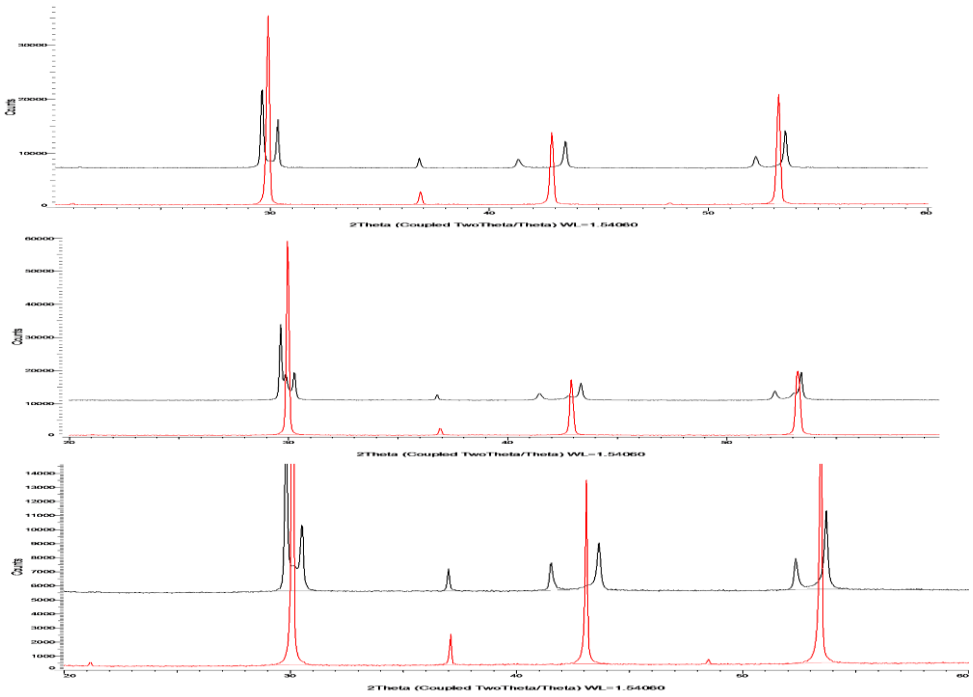

Figure 19. X-ray diffractograms of the T-BTI70 (top), BSTI70 (middle) and CIP-BTI70-W (bottom) samples. Hydrated = black line and as-prepared = red line. The change in diffraction profile going from an as-prepared to hydrated material corresponds to a change from a cubic to tetragonal perovskite.

To verify that the change in diffraction profile originated from hydration and not some other reaction, the BTI70 based samples were subjected to XRD after dehydration in the TGA. All samples had then reverted to their dehydrated form, displaying the same diffraction pattern as before hydration.

In contrast to the BTI70 based sample, the BTS70 based samples retained their cubic structure after being subjected to extensive hydration, although perhaps with a small shift towards lower 2θ-angles, or larger d-spacings, indicating an increase of the unit cell volume.

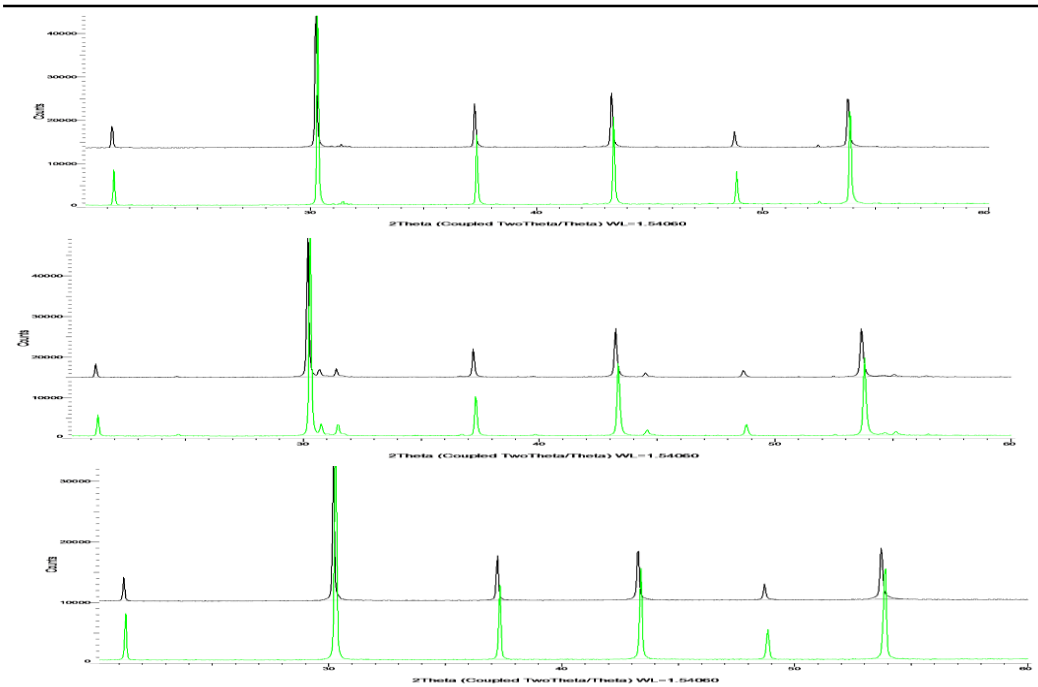

Figure 20. X-ray diffractograms of the T-BTS70 (top), BSTS70 (middle) and CIP-BTS70-W (bottom) samples showing the preservation of the cubic structure after hydration. Hydrated = black line and as-prepared = green line.

Much like the BTS70 based samples, the hybrid BTSI35 and BTSI50 samples did not change structure upon hydration, although perhaps with some small shifts towards larger and smaller d-spacings, respectively, see figure below.

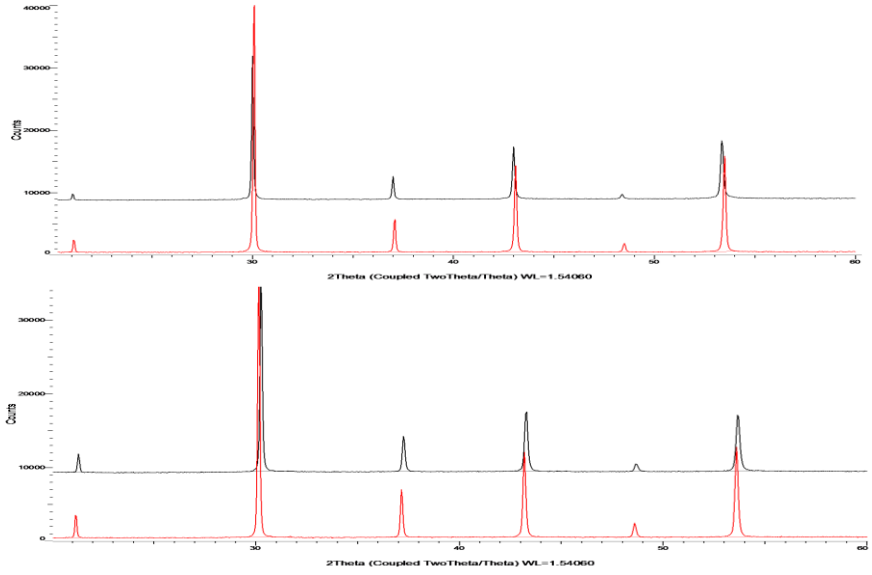

Figure 21. X-ray diffractograms of the BTSI35 (top) and BTSI50 (bottom) samples showing the preservation of the cubic structure after hydration. Hydrated = black line and as-prepared = red line.

4.1.7 Structure analysis

X-ray data from a CIP-BTI70-W and a CIP-BTS70-W sample, sintered at 1400°C and 1500°C respectively, was used to obtain the structural parameters of $BaTi_{0.3}In_{0.7}O_{3-\delta}$ and $BaTi_{0.3}Sc_{0.7}O_{3-\delta}$. This was done through Rietveld refinement using the program GSAS. [52] BTS70 was found to adopt a cubic perovskite structure with space group Pm-3m and cell parameter a = 4.16334 Å. BTI70 was found to belong to the same space group, with a cell parameter of 4.20148 Å. The uncertainties for the cell parameters were estimated to approximately 0.00005 and 0.00002 Å, respectively. The structural parameters obtained through Rietveld refinement are summarized in the table below.

Table 6. A table summarizing the structural parameters obtained through Rietveld refinement of CIP-BTS70-W and CIP-BTI70-W sintered at 1500°C and 1400°C, respectively. The values in parentheses are the estimated uncertainties and refer to the variance of the last decimal in the reported value.

Sample	BTS70	BTI70
Space group	Pm-3m	Pm-3m
Unit cell parameter (Å)	4.16334(5)	4.20148(2)
Isotropic thermal parameter, U_{iso} (Å²)		
Ba (1/2, 1/2, 1/2)	0.0236(0)	0.0125(5)
Ti (0, 0, 0)	0.0267(0)	0.0046(6)
Sc or In (0, 0, 0)	0.0267(0) (Sc)	0.0046(6) (In)
O (0, 0, 1/2)	0.0146(0)	0.0065(18)
Site occupancies		
Ba (1/2, 1/2, 1/2)	1	1
Ti (0, 0, 0)	0.3	0.3
Sc or In (0, 0, 0)	0.7 (Sc)	0.7 (In)
O (0, 0, 1/2)	0.883	0.883
Distances (Å)		
Ba -- O	2.94393	2.97090
Ti/(Sc or In) - O	2.08167 (Ti/Sc - O)	2.10074 (Ti/In – O)
Chi^2	18.04	16.43
Rwp (%)	7.51	8.32
Rp (%)	5.13	6.18
Number of refined parameters	17	17

The difference plots obtained and used to evaluate the fit between the model and the observed data can be seen in the figure below.

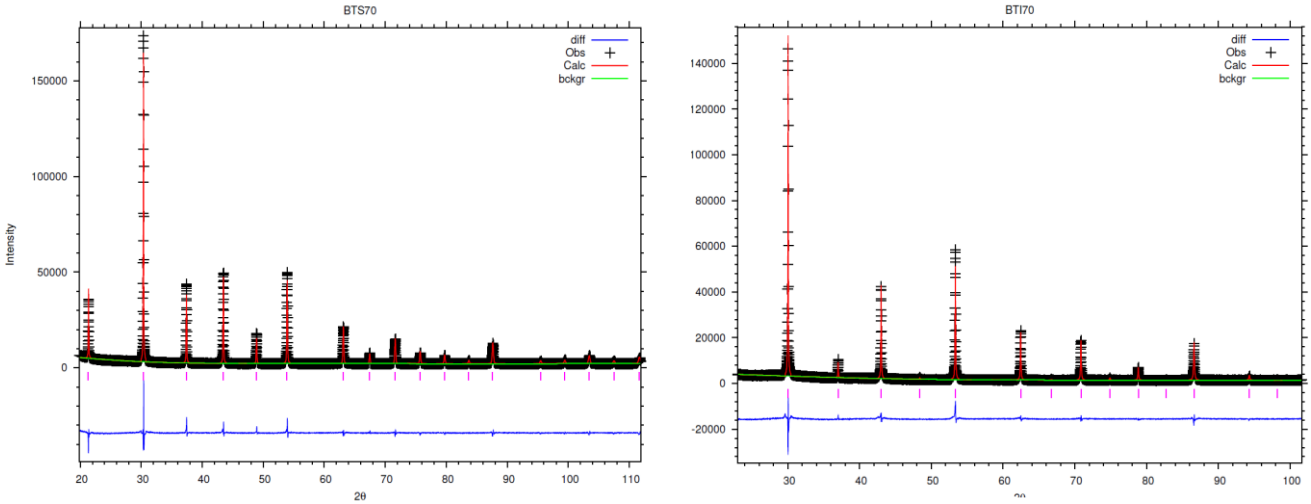

Figure 22. The difference plots obtained by Rietveld refinement in the program GSAS for a CIP-BTS70-W and CIP-BTI70-W sample, indicating the goodness-of-fit between the calculated data from the structural model and the observed data. The leftmost profile belongs to BTS70 and the rightmost profile belongs to BTI70. Black crosses = observed data, red line = calculated data, green line = modeled background, blue line = difference line.

Using the program VESTA, the crystal structure was visualized for both $BaTi_{0.3}Sc_{0.7}O_{3-\delta}$ and $BaTi_{0.3}In_{0.7}O_{3-\delta}$ as seen below. [53]

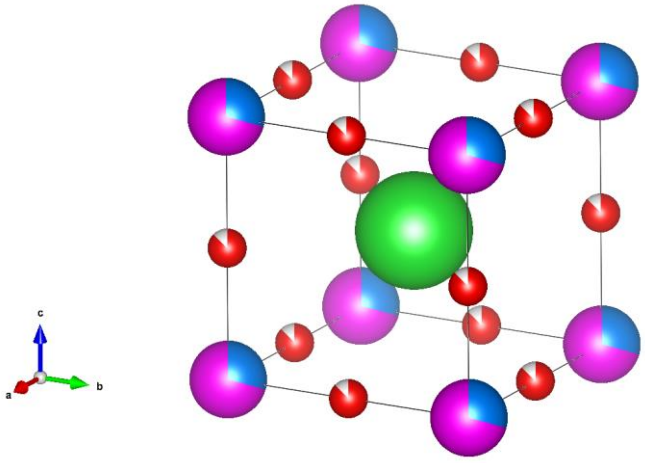

Figure 23. A figure showing the crystal structure of BTS70. Green = Ba, Blue = Ti, Purple = Sc, Red = O. Note that the fractional occupancy of the (0, 0, 0) site by Sc and Ti is represented by those spheres being split into a blue part and a purple part corresponding to the 0.3 and 0.7 fractional occupancy of Ti and Sc, respectively. The oxygen deficiency is portrayed similarly with a fraction of each sphere being white, representing this deficiency.

Although not clearly visible in these two figures, there are subtle differences between the structures of BTS70 and BTI70, stemming from the difference in unit cell dimensions which consequently leads to different bond distances between, for example, barium and oxygen. It should also be mentioned that

these figures are just a schematic representation of both structures and represent an average unit cell. With such heavy substitution and large amount of oxygen vacancies there might be a larger degree of randomness on the local atomic level than these figures suggest.

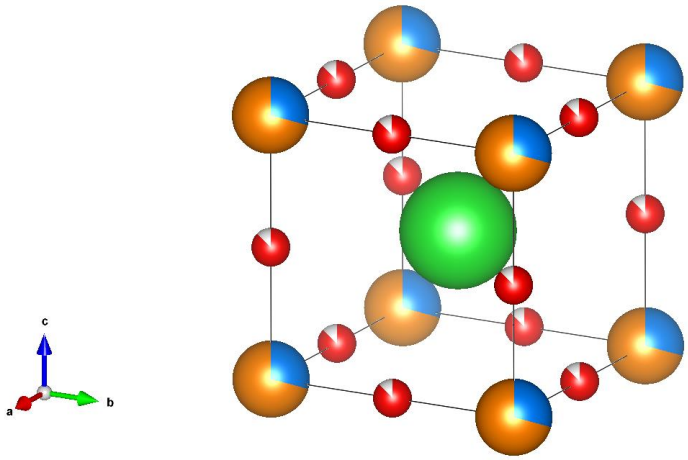

Figure 24. A figure showing the crystal structure of BTI70. Green = Ba, Blue = Ti, Orange = In, Red = O. Note that the fractional occupancy of the (0, 0, 0) site by In and Ti is represented by those spheres being split into a blue part and an orange part corresponding to the 0.3 and 0.7 fractional occupancy of Ti and In, respectively. The oxygen deficiency is portrayed similarly with a fraction of each sphere being white, representing this deficiency.

4.2 Thermogravimetric analysis, hydration and differential scanning calorimetry

The results from TG analysis will be presented in terms of onset- and inflection temperatures as well as the percent hydration at different stages of the dehydration. The onset temperature is the temperature at which the sample starts loosing mass while the inflection temperature corresponds to the temperature at which the mass loss rate reaches its highest value. The percentage mass changes will also be displayed, for completion more than anything. Since only the percentage mass change doesn't provide a meaningful base for comparison of samples with different chemical constitution, in terms of hydration, one should look instead at the calculated values of hydration, displayed in the tables, whose values have been calculated from the mass changes displayed in the figures.

4.2.1 Percent hydration of trial vs tin samples

Comparing the percent hydration of the hydrated and as-prepared, i.e non-hydrated, variants of the trial and tin containing samples, see table below, shows that all samples hydrate to an extent during the synthesis conditions, especially the scandium containing ones, and that the degree of hydration increases after treatment in the hydration oven, in particular for the indium samples. A calculation example showing how to obtain the percent hydration of a sample from the data of a TG analysis can be found in the appendix.

Table 7. The percent hydration of as-prepared (a.p.) and hydrated (hydr.) trial and tin samples, obtained through TG analysis.

Sample	Percent hydration
Indium samples	
T-BTI70 a.p.	24.5 %
T-BTI70 hydr.	90.8 %
BSTI70 a.p.	41.6 %
BSTI70 hydr.	99.8 %
Scandium samples	
T-BTS70 a.p.	52.2 %
T-BTS70 hydr.	82.0 %
BSTS70 a.p.	63.0 %
BSTS70 hydr.	76.9 %

4.2.2 Comparison of the TG curves of hydrated trial and tin samples

Looking at the figure below, it is clearly visible that T-BTI70 and BSTI70 have both a lower onset temperature and a lower inflection temperature than their scandium counterparts, indicating that the protonic defects are less stable in these indium containing materials. However, these samples also hydrate to a larger extent, looking at the table above, displaying very high hydration levels of above 90% for T-BTI70 and almost 100% for BSTI70. In addition to the high hydration level, BSTI70 also shows a higher onset- and inflection temperature than its T-BTI70 cousin.

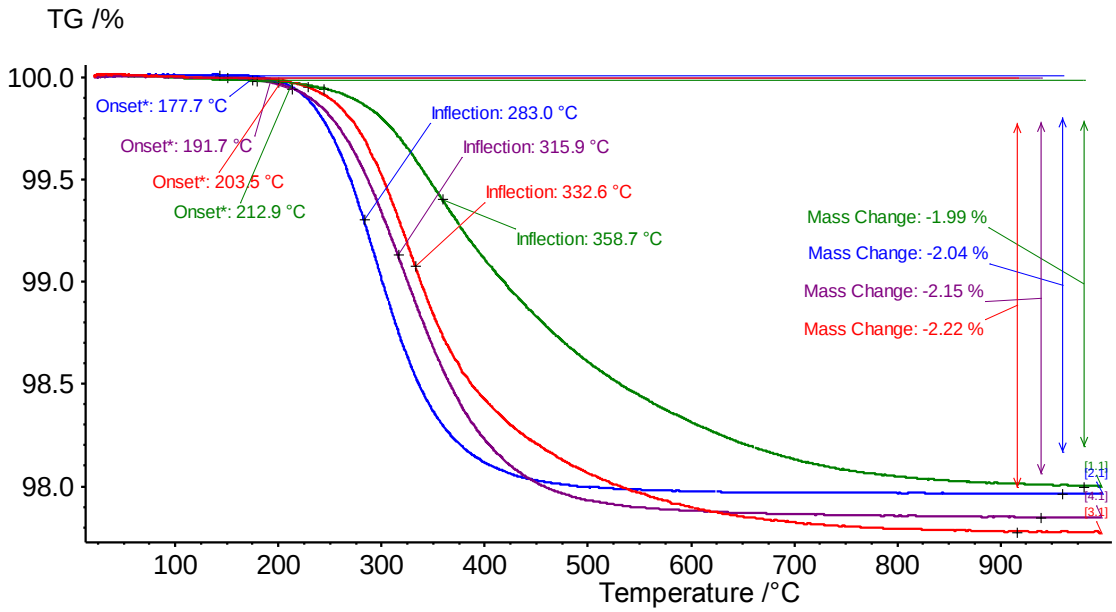

Figure 25. A figure showing the TG curves of T-BTI70 (blue), BSTI70 (purple), T-BTS70 (red) and BSTS70 (green). The indium samples had been sintered at 1400°C while the scandium samples had been sintered at 1550°C.

Comparing T-BTS70 with BSTS70 shows that the addition of tin to the BTS70 perovskite seems to stabilize the protonic defects in the material, as indicated by the slightly higher dehydration onset temperature and much higher inflection temperature. Looking at table 7 above, in contrast to the effect of tin on the initial hydration level of indium substituted samples, tin seems to lower the hydration level of BSTS70 as compared to T-BTS70. It should be noted that both T-BTS70 and BSTS70 contained impurities, which could affect the results and is elaborated on in the discussion.

In the figure below, the progression of dehydration is shown by the indicated hydration levels of the different samples. These values have been calculated as a percentage of the initial hydration. These results indicate, perhaps even more strongly than the onset- and inflection temperature, that the scandium samples hold on to their protons to much higher temperatures. What is also apparent is the effect of tin addition to these samples. The BSTS70 sample is still 20% hydrated at a temperature of almost 570°C compared to 450°C for T-BTS70. Similarly, BSTI70 retains 20% hydration at just above 390°C, compared to BTI70's 350°C.

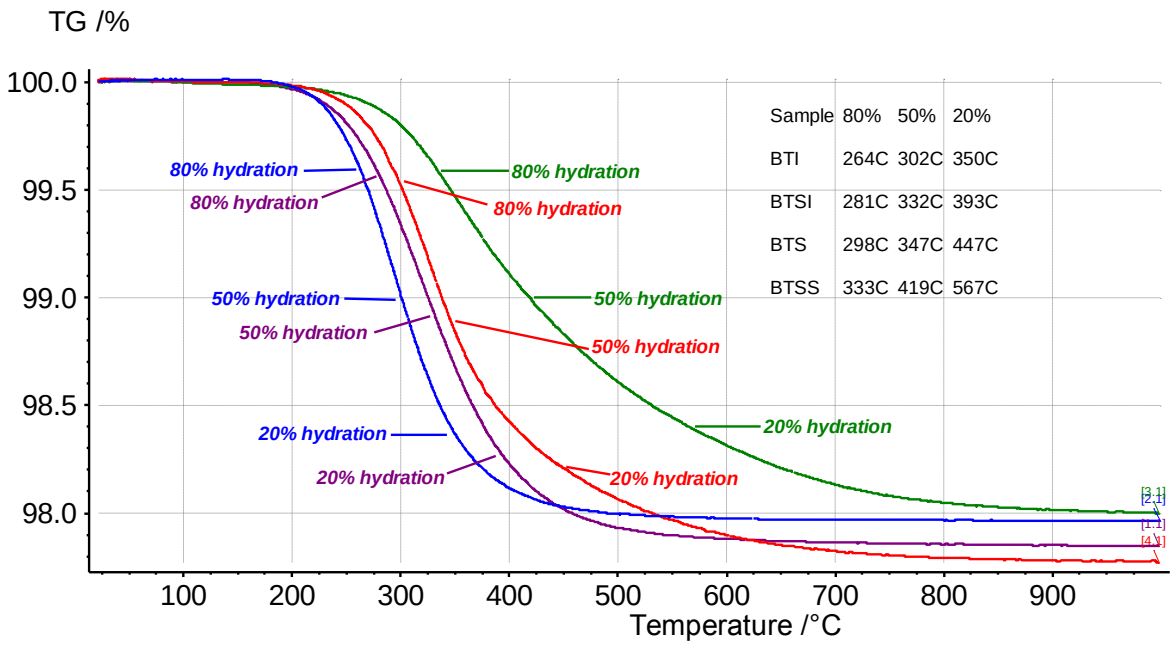

Figure 26. A figure showing the progression of dehydration for T-BTI70 (blue), BSTI70 (purple), T-BTS70 (red) and BSTS70 (green). The indium samples had been sintered at 1400°C while the scandium samples had been sintered at 1550°C. The table in the upper right corner of the figure shows the temperatures at which each sample had reached 80, 50 and 20% hydration compared to their initial hydration level.

4.2.3 Percent hydration of trial vs mixed Sc/In samples

Examining the table below reveals that the hybrid samples have hydrated to a larger extent than both T-BTS70 and T-BTI70, in both their as-prepared and hydrated form. If these values are representative, the incorporation of both indium and scandium in the perovskite structure seems to have a synergistic effect on the hydration level that can be obtained. It should be noted that the hydrated BTSI35 shows a hydration of just above 100% which is not possible assuming the composition $BaTi_{0.3}Sc_{0.35}In_{0.35}O_{3-\delta}$ is correct, which the XRD scans indicate. In addition, the amount of impurities found from X-ray diffraction are miniscule, or non-existent, and should not affect the hydration behavior to any large extent. A possible explanation might be that the TGA correction run was done at the start of the study and never renewed. Therefore the samples analyzed at the later stages of the study might have given results with a larger error than those analyzed a few months earlier since the experimental conditions can change slightly during such a time span. Another source of error might be contamination by dust, human hair or other contaminants prior to TG analysis. Either way, the as-prepared BTSI35 shows that the sample has the potential for extensive hydration, even at ambient conditions, something which is supported by the results from its hybrid cousin, BTSI50.

Table 8. The percent hydration of as-prepared (a.p.) and hydrated (hydr.) trial and mixed Sc/In samples, obtained through TG analysis.

Sample	Percent hydration
Trial samples	
T-BTI70 a.p.	24.5 %
T-BTI70 hydr.	90.8 %
T-BTS70 a.p.	52.2 %
T-BTS70 hydr.	82.0 %
Hybrid samples	
BTSI35 a.p	62.2 %
BTSI35 hydr.	100.4 %*2
BTSI50 a.p	67.5 %
BTSI50 hydr.	99.0 %

*** 2 The reason for the above 100% hydration is unknown. The amount of impurities in this sample is miniscule or non-existent on XRD-scans and should not affect the hydration behavior. See paragraph above table 8 for possible explanations.**

4.2.4 Comparison of the TG curves of hydrated trial and mixed Sc/In samples

Looking at figure 27 below, the hybrid samples BTSI35 and BTSI50 show an unexpected behavior, displaying a lower onset temperature than both T-BTI70 and T-BTS70. It might've been expected for these samples to have onset temperatures in between that of the trial samples, especially BTSI35 which is essentially a 50/50 mix of both. The same expectation could've been valid for the inflection temperature of these samples. Examining the figure it seems like both hybrid samples have values very similar to T-BTI70, around 280°C, and far from that of T-BTS70 at over 330°C. In terms of when the

samples start to dehydrate and when they experience the maximum rate of mass loss, scandium incorporation in the structure therefore seems to have little impact on these hybrid samples.

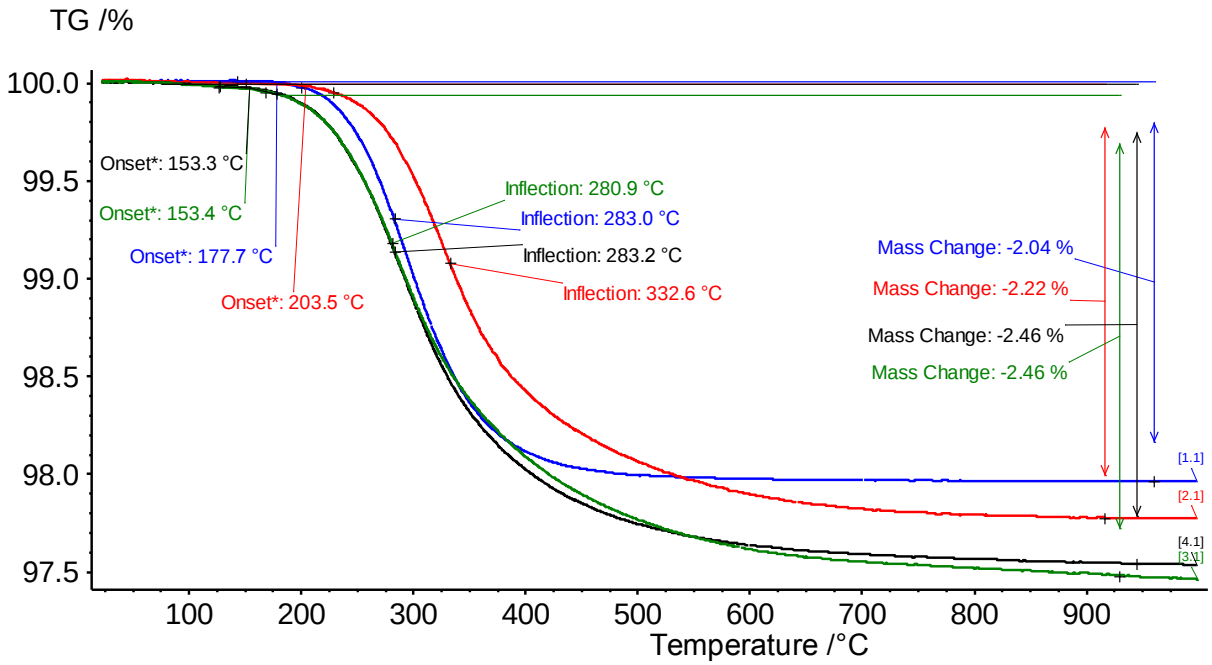

Figure 27. A figure showing the TG curves of T-BTI70 (blue), BTSI35 (black), BTSI50 (green) and T-BTS70 (red). The indium and hybrid samples had been sintered at 1400°C while the scandium sample had been sintered at 1550°C.

The progression of hydration reveals that the samples stay hydrated at higher temperatures the higher the scandium substitution level, as shown in figure 28. BTSI35 shows a dehydration behavior quite similar to T-BTI, although with a greater ability to retain some of its protons, showing a hydration level of 20% even at 400°C compared to T-BTI's 350°C. Following this trend BTSI50 shows further gains in protonic stability, displaying a 20% hydration level at 429°C. It seems that the presence of scandium in the structure of the mixed samples has no, or only a slight, effect on the ability of these materials to retain high to intermediate levels of hydration, i.e 80% and 50%, but does cause an increase in the high temperature stability of the remaining protonic defects compared to T-BTI70.

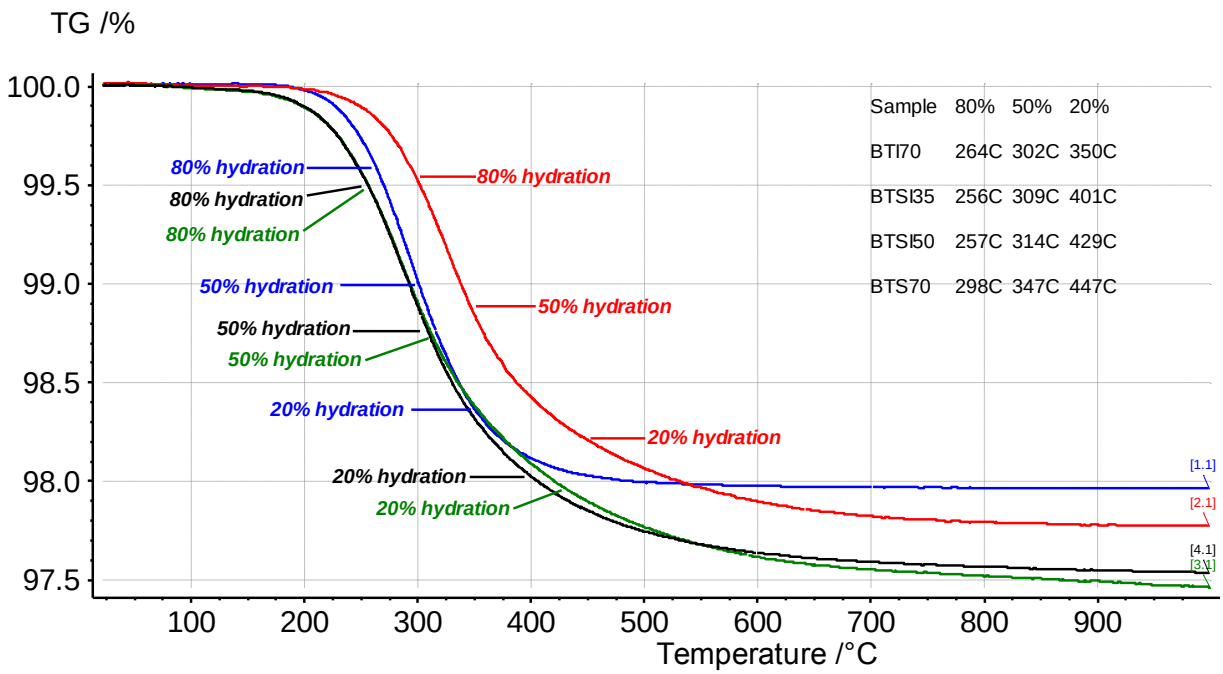

Figure 28. A figure showing the progression of dehydration for T-BTI70 (blue), BTSI35 (black), BTSI50 (green) and T-BTS70 (red). The indium and hybrid samples had been sintered at 1400°C while the scandium sample had been sintered at 1550°C. The table in the upper right corner of the figure shows the temperatures at which each sample had reached 80, 50 and 20% hydration compared to their initial value.

4.2.5 Percent hydration of trial vs CIP-W samples

Inspecting the table below it can be seen that the indium CIP-W sample reaches a higher hydration level than its trial counterpart both in its as-prepared and hydrated state. The scandium CIP-W sample also seems to hydrate to a larger extent when purposefully hydrated, although the as-prepared sample has a slightly lower level of hydration.

Table 9. The percent hydration of as-prepared (a.p.) and hydrated (hydr.) trial and CIP-W samples, obtained through TG analysis.

Sample	Percent hydration
Indium samples	
T-BTI70 a.p.	24.5 %
T-BTI70 hydr.	90.8 %
CIP-BTI70-W a.p.	36.5 %
CIP-BTI70-W hydr.	96.2 %
Scandium samples	
T-BTS70 a.p.	52.2 %
T-BTS70 hydr.	82.0 %
CIP-BTS70-W a.p.	45.6 %
CIP-BTS70-W hydr.	97.1 %

4.2.6 Comparison of the TG curves of hydrated trial and CIP-W samples

As seen in the figure below, the onset and inflection temperatures of both CIP-BTI70-W and CIP-BTS70-W differ somewhat from their trial sample counterparts. It seems however, like the processed BTI70 sample resembles more closely its non-processed counterpart than does CIP-BTS70-W. This might stem from the fact that T-BTS70 actually isn't entirely phase pure and therefore the behavior of CIP-BTS70-W, which is phase pure, might show somewhat more truthfully how a phase pure BTS70 does in fact behave during dehydration than T-BTS70 does.

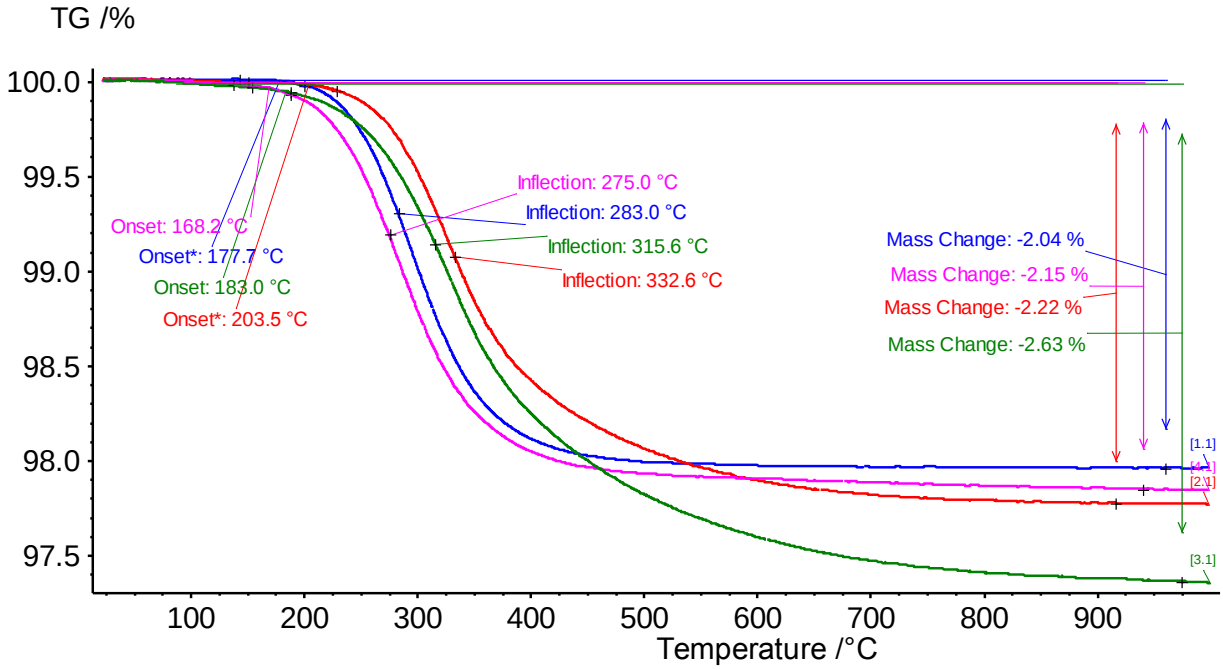

Figure 29. A figure showing the TG curves of T-BTI70 (blue), CIP-BTI70-W (pink), T-BTS70 (red) and CIP-BTS70-W (green). The indium samples had been sintered at 1400°C while the scandium samples had been sintered at 1550°C.

Examining the figure below, the progression of dehydration for T-BTI70 and CIP-BTI70-W is quite similar. The TG curves of T-BTS70 and CIP-BTS70-W also follow each other quite closely until about 375°C where the CIP-BTS70-W sample deviates from the expected curve and displays an increased protonic defect stabilization compared to T-BTS70 at the higher temperatures. This is shown by the remnant 20% hydration at 480°C for CIP-BTS70-W compared to T-BTS70's 447°C. Again, this difference might stem from the small impurity phases present in the T-BTS70 sample.

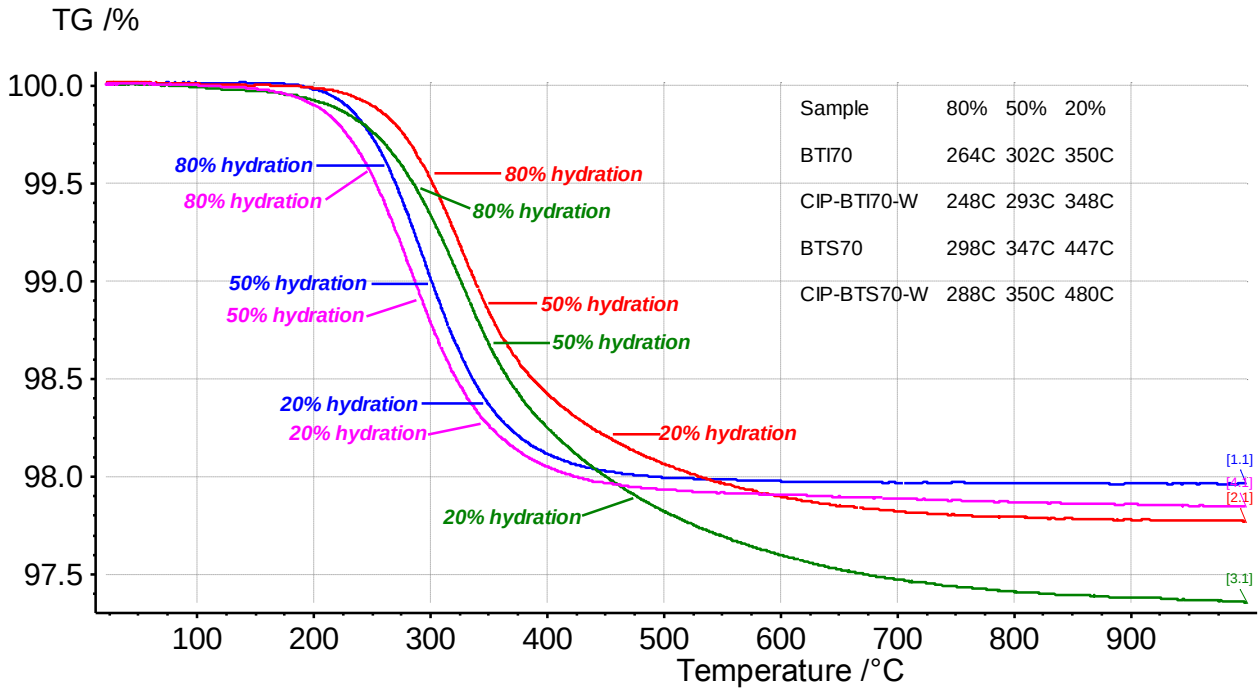

Figure 30. A figure showing the progression of dehydration for T-BTI70 (blue), CIP-BTI70-W (pink), T-BTS70 (red) and CIP-BTS70-W (green). The indium samples had been sintered at 1400°C while the scandium samples had been sintered at 1550°C. The table in the upper right corner of the figure shows the temperatures at which each sample had reached 80, 50 and 20% hydration compared to their initial value.

4.2.7 Results from differential scanning calorimetry

The study of the hydration thermodynamics of the synthesized materials is not part of this study and, as such, no great focus will be directed towards analyzing the results from the differential scanning calorimetry. However, to give an indication of the general hydration behavior of these materials, DSC results from T-BTI70 in its as-prepared and hydrated form will be displayed, see figure below. The appearance of the DSC curves of all other samples is similar, with different magnitudes of the endothermic peaks.

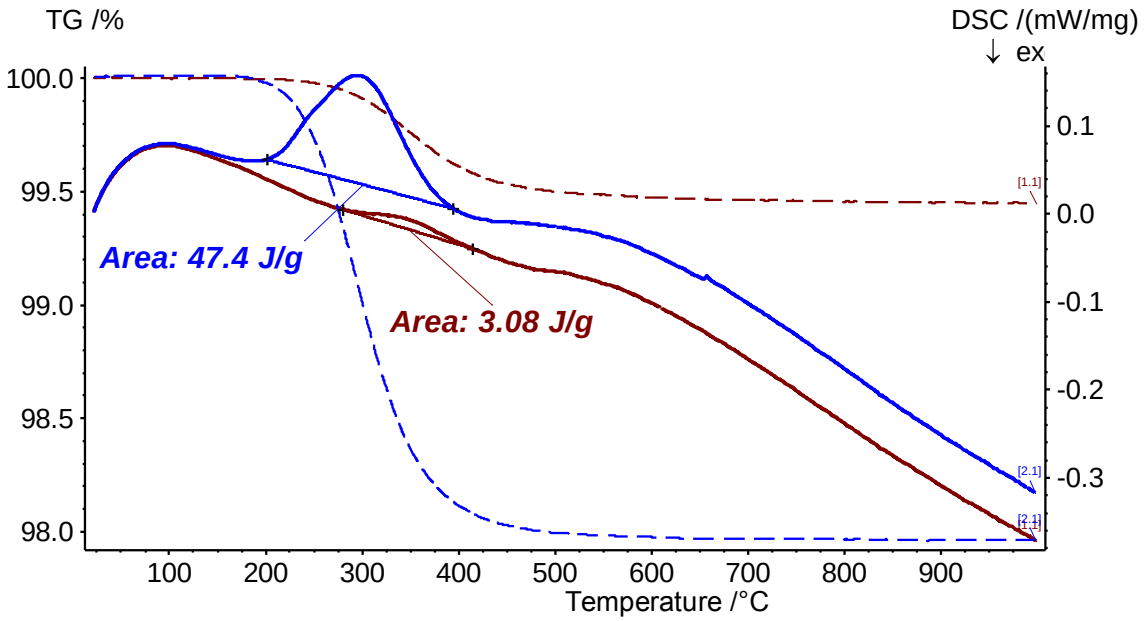

Figure 31. A figure showing the results from performing DSC on as-prepared (brown) and hydrated (blue) T-BTI70. The dotted lines are the TG curves while the drawn lines are the DSC curves. The indicated area represent the endothermic peaks of the hydrated and as-prepared samples.

As can be seen in the figure above, the endothermic peak of the hydrated T-BTI70 sample is more than 15 times as large as that of the as-prepared T-BTI70 in terms of area. To dehydrate 1 g of purposefully hydrated T-BTI70, 47.4 J is needed while only 3.08 J is required for 1 g of as-prepared T-BTI70. This confirms what was brought up in the theory section, namely that the hydration reaction is exothermic for these types of materials and, thus, that their dehydration requires an input of energy.

4.3 Relative density

The relative densities achieved for all chemically modified and processed samples are presented below. These values are always shown in relation to those of the trial samples, whose values are therefore not presented in a section of their own.

4.3.1 Relative densities of tin samples

By measuring the dimensions and mass of the pellets after, ideally, every sintering step one can observe how the density of the samples changes with each sintering step. Comparing this density with the maximum theoretical density of the respective pure perovskite phase gives a value of the relative density that has been experimentally achieved, as a percentage of the theoretical density. The theoretical density can be obtained by calculating the weight of all the atoms in a unit cell and dividing this weight by the

unit cell volume, obtained from the unit cell dimensions acquired through powder X-ray diffraction. A calculation example can be found in the appendix.

Values for the relative density have only been calculated for those heating steps after which the perovskite phase dominated the material makeup. As an example, sintering at 1000°C never yielded a dominating perovskite phase for any BTS70 or BSTS70 sample and calculating a relative density for those samples is therefore meaningless. For those samples which density calculations have been done, some values have been excluded from the results section to improve clarity. However, all relative densities are listed in the appendix.

Looking at the figure below it can be seen that the BSTS70 sample, i.e the tin incorporated sample, displays a lower relative density than T-BTS70 for all sintering temperatures which suggests that tin has a negative impact on the densification during sintering. While the density of T-BTS70 varies between 79-85 %, the BSTS70 samples display values ranging from 76-78%.

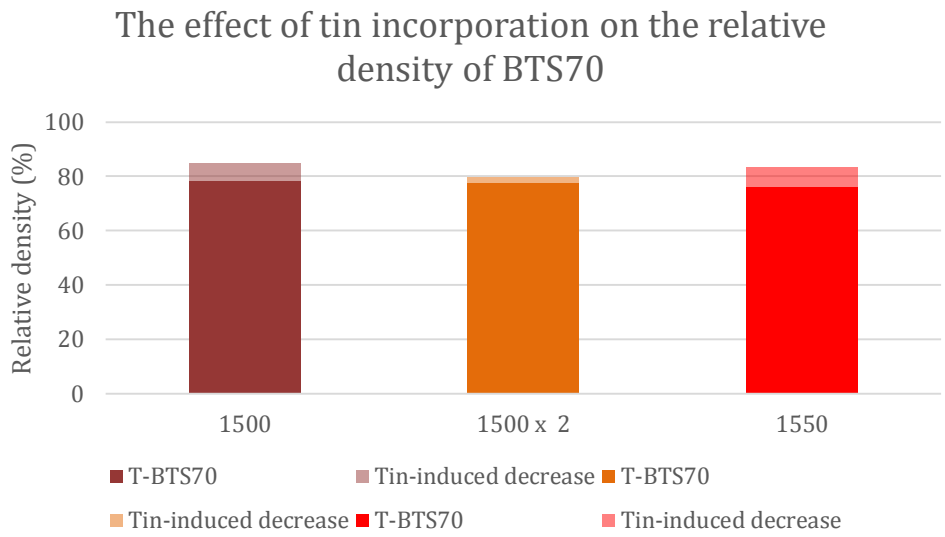

Figure 32. A figure showing the effect of tin incorporation on the relative density of BTS70 after the relevant sintering steps at 1500-1550°C.

Much like the BTS70 case, the incorporation of tin in BTI70 seems to lead to a lower density, although perhaps with a less pronounced effect, see figure below. While T-BTI70 shows a density of almost 87 % at 1400°C, that of BSTI is closer to 83%.

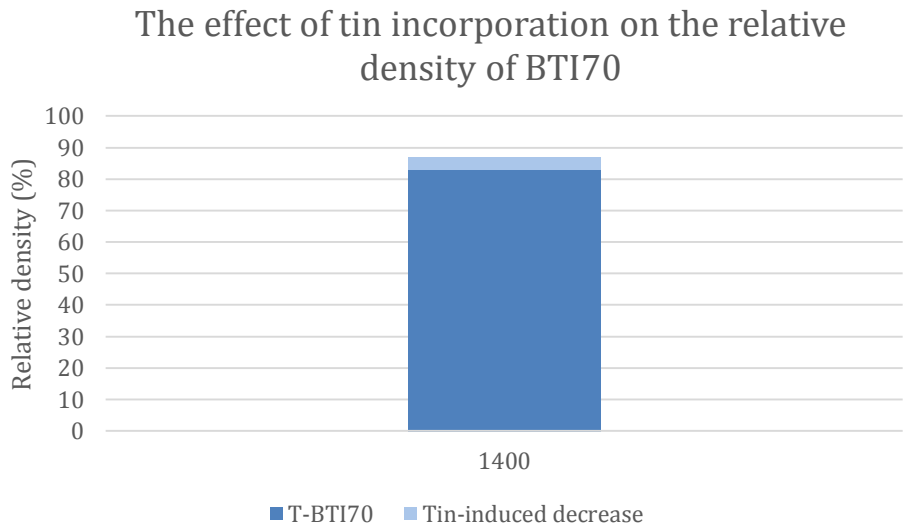

Figure 33. A figure showing the effect of tin incorporation on the relative density of BTI70 after the sintering at 1400°C.

4.3.2 Relative densities of mixed Sc/In samples

The figure below shows how the relative density of BTI70 seems to suffer from incorporation of scandium in the perovskite structure, decreasing from almost 87% to roughly 82 and 80% for the BTSI35 and BTSI50 samples respectively.

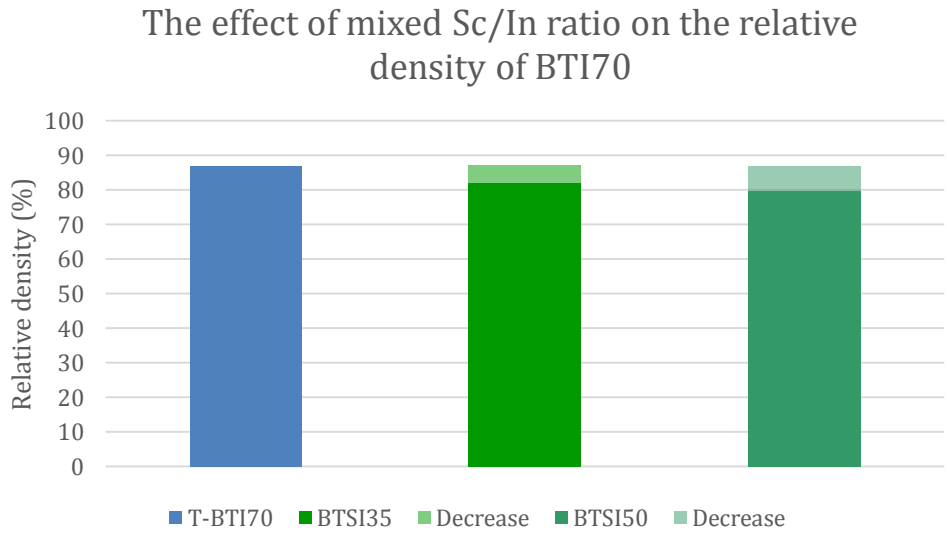

Figure 34. A figure showing the effect of a mixed Sc/In ratio on the relative density of BTI70 after the sintering at 1400°C.

The relative densitites of these hybrid Sc/In samples are also lower than that of the T-BTS70 samples, going from 85% to the values mentioned above for BTSI35 and BTSI50. It should be noted that T-BTS70

was sintered at a higher temperature than the mixed samples and so a direct comparison of their relative densities might not be completely straightforward.

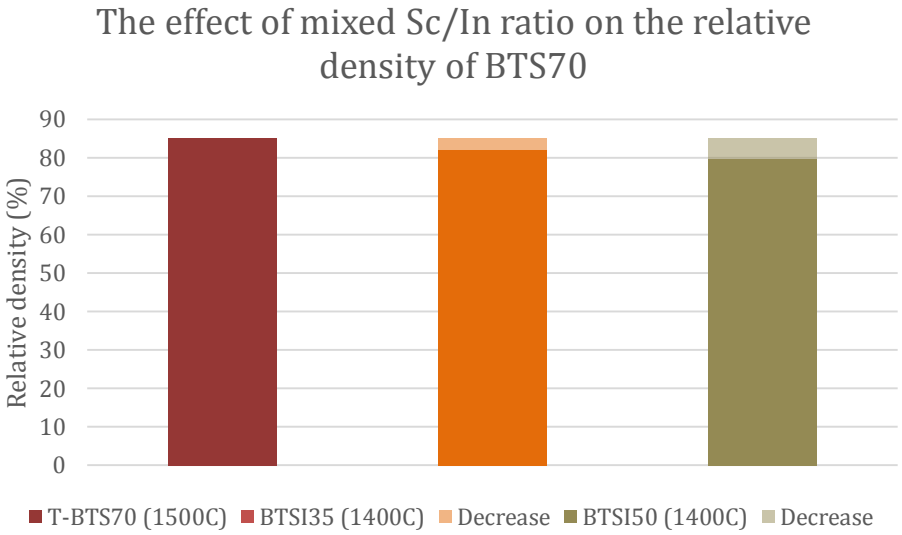

Figure 35. A figure showing the effect of a mixed Sc/In ratio on the relative density of BTS70 after sintering. Note that the relative density of T-BTS70 was calculated after sintering at 1500°C while the mixed Sc/In samples only needed sintering at 1400°C and therefore have no relative density values after a 1500°C sintering.

4.3.3 Relative densities of isostatically pressed samples

4.3.3.1 First batch of CIP samples

Looking at figure 36, both CIP BTS70 samples show an increased density compared to T-BTS70. The improvement is most pronounced for the sample pressed as a wet paste, i.e CIP-BTS70-W, displaying a relative density of almost 93 %. The samples pressed dry shows only a marginal improvement over T-BTS70, 86% compared to 85%.

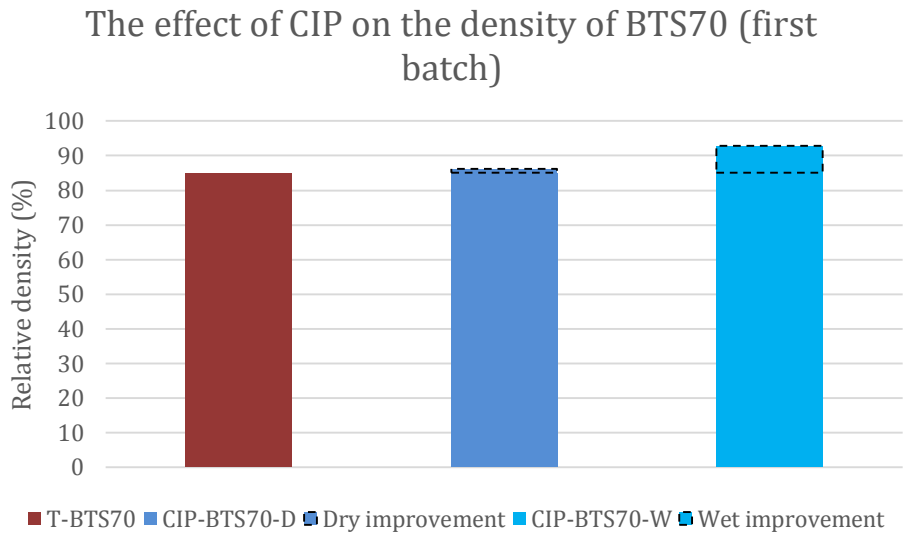

Figure 36. A figure showing the effect of cold isostatic pressing on the relative density of BTS70 after sintering at 1500°C.

Similarly, the CIP samples of BTI70 show a very marginal increase in density for the dry pressed sample, while the wet pressed sample displays a much larger increase from 87 to above 100%. It is obviously not possible to get a higher density than the maximum theoretical value. The fact that CIP-BTI70-W seems to achieve just this is most probably due to a small measurement error when measuring the dimensions of the pellet, which was slightly non-uniform in shape.

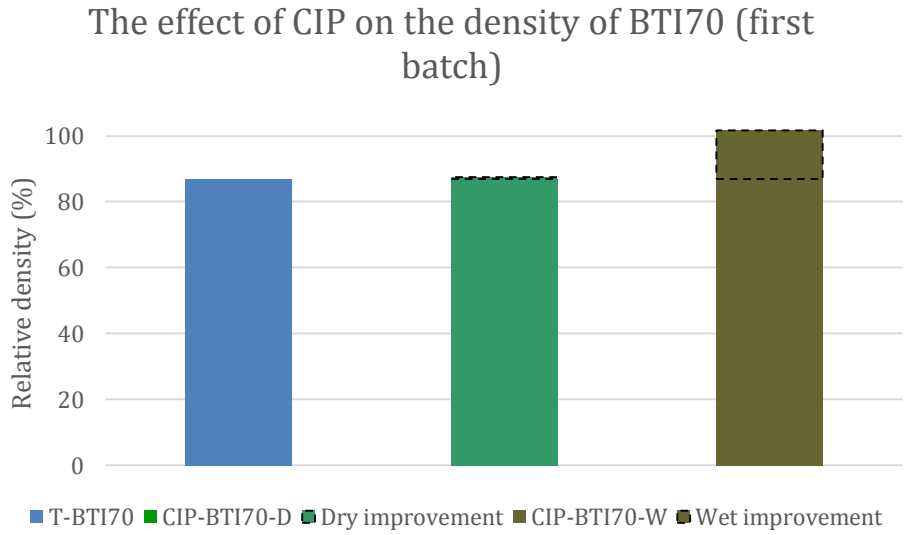

Figure 37. A figure showing the effect of cold isostatic pressing on the relative density of BTI70 after sintering at 1400°C. Note that the relative density of CIP-BTI70-W slightly exceeds 100% which most probably is due to a small measurement error as the pellet was somewhat non-uniform in shape.

4.3.3.2 Second batch of CIP samples

The second batch of CIP samples shows a diversity in the results, indicating that cold isostatic pressing is not an infallible technique when trying to produce dense samples. While pellet 1 displays a similar increase as the first batch sample, from 85 to almost 91 %, the second and third pellet show a decrease to 83 and 79%, respectively. A likely explanation could be the fact that, when pre-pressed, it was noted that pellet 2 and 3 were pressed in a much wetter state. It was observed that ethanol seeped out of the sides of the press during pressing, something which did not happen for the first pellet. It might be that too much ethanol present in the pellet hinders extensive pore collapse during subsequent isostatic pressing, resulting in less dense green pellets. Consequently, the sintered pellets have a harder time achieving high density. Further support for this hypothesis can be found when looking at the success of the second batch of CIP BTI70 pellets which, although wet, were noted to be drier than the CIP BTS70 samples when pressed.

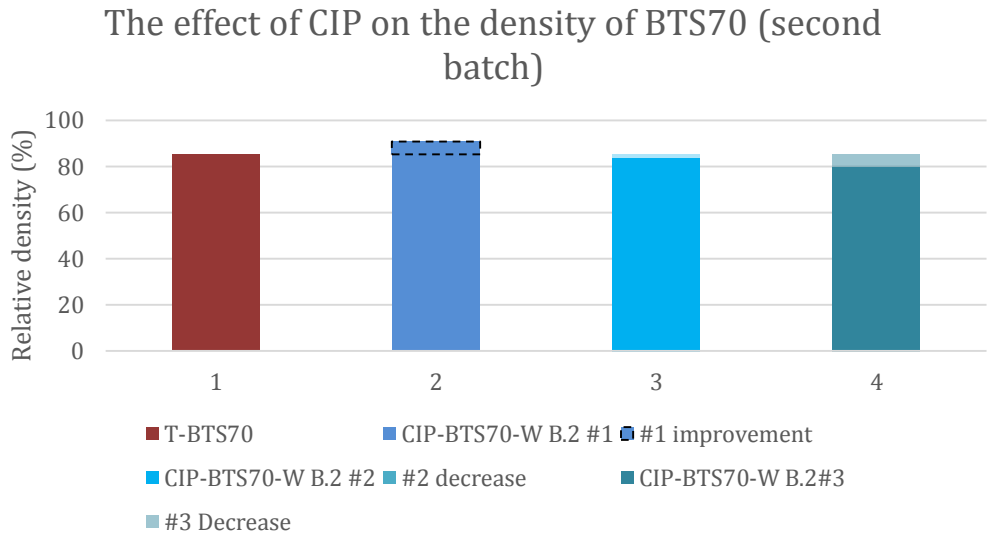

Figure 38. A figure showing the effect of cold isostatic pressing on the relative density of BTS70 after sintering at 1500°C. Note that three different pellets were processed, denoted #1, #2 and #3 in the figure.

Unlike the second batch of CIP BTS70 samples, the CIP BTI70 samples all display a large increase in density compared to T-BTI70, from 87 to 98% (for both pellet 2 and 3). Note that pellet 1 is not included as it was found to be misshaped after pressing.

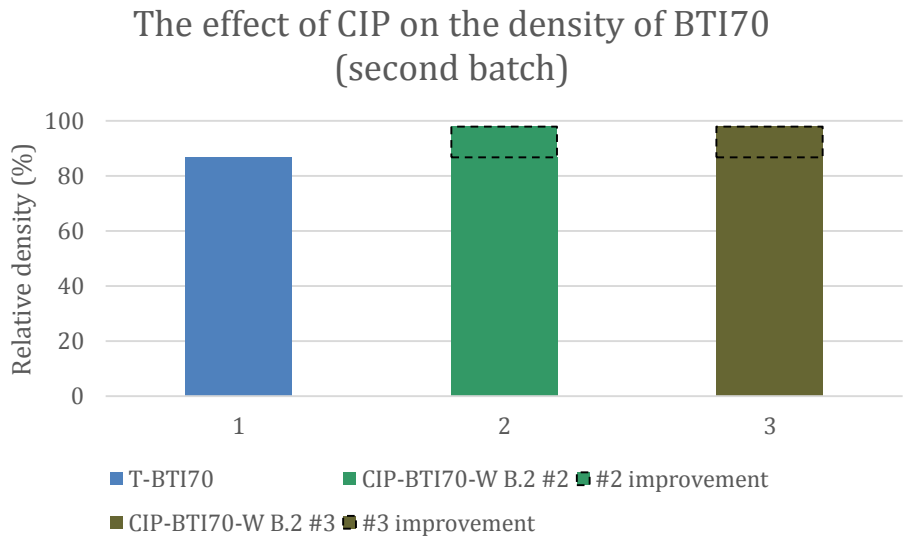

Figure 39. A figure showing the effect of cold isostatic pressing on the relative density of BTI70 after sintering at 1400°C. Note that three different pellets were processed and that pellet #1 was misshaped and therefore not used for calculations. The two remaining pellets are denoted #2 and #3 in the figure.

4.3.4 Relative densities of slipcasted samples

Looking at the results from slipcasting it seems like there is potential for achieving high densities, as demonstrated by SC-BTI70 which has a relative density of 93% compared to the 87% of T-BTI70. In contrast the SC-BTS70 sample shows a decrease in relative density, going from 85% for T-BTS70 to 71 % which is the lowest value of all processed samples. The explanation for this result is likely very straightforward. As has been explained, the slipcasting process relies on sedimentation of particles and absorption of the suspension liquid, i.e ethanol in this case, by plaster. It was observed that the ethanol was absorbed much faster by the underlying plaster of the BTS70 sample which meant topping of the suspension being casted became a micromanagement issue. At times, the BTS70 suspension had nearly dried out before being topped of and so layers of sedimented material formed, instead of a non-layered homogeneous pellet. This was clearly visible after the final drying overnight as the SC-BTS70 sample was layered to a much greater extent than SC-BTI70. When sintered, this would very likely have had a large negative impact on the densification.

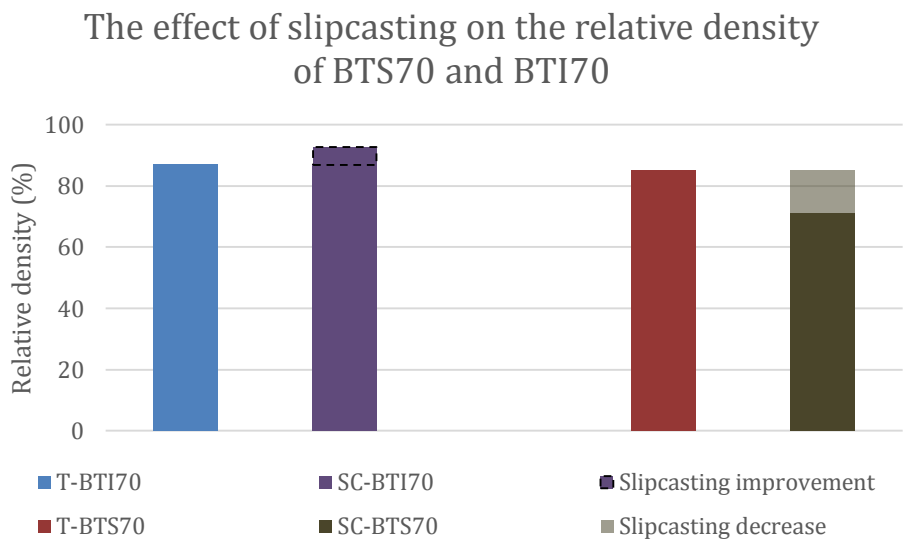

Figure 40. A figure showing the effect of slipcasting on the relative densities of BTI70 and BTS70 after sintering at 1400 and 1500°C, respectively.

4.4 Impedance spectroscopy

The results from impedance spectroscopy, performed on select CIP pellets, are presented below. It must be said that the data was quite difficult to interpret and in order to obtain accurate estimates of the conductivity as a function of temperature a more detailed analysis should be performed. Only part of the data has been used because of the difficulties evaluating the low and high temperature data and conductivity values have therefore been calculated for the intermediate temperatures of 350, 450 and 550°C. Conductivity will be displayed in logarithmic form to facilitate comparison with other studies and refers to the total conductivity of the sample, since the contributions from the bulk and grain conductivity could not be separated.

Relevant dimensions of pellets and their electrodes can be found in the appendix, as well as a calculation example showing the procedure for obtaining the conductivity and activation energy for a specific sample.

4.4.1 Raw data – Nyquist plots

To illustrate the typical appearance of the data, and the fitting using the equivalent circuit described in the method section, two Nyquist plots from the impedance spectroscopy performed on pellet 1 of the BTS70 CIP samples are shown in the figure below.

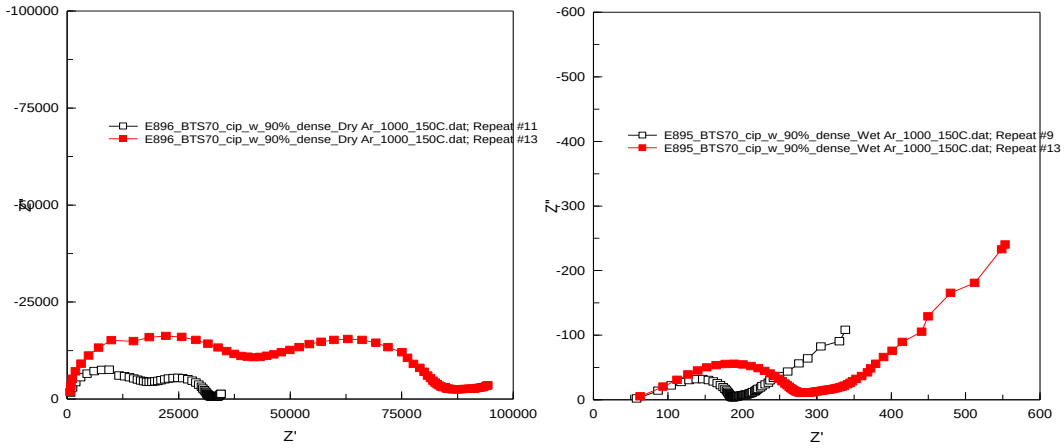

Figure 41. A figure showing the typical appearance of the results from impedance spectroscopy performed on the pellets of BTS70 and BTI70. To the left, BTS70 (pellet 1) analyzed in dry argon with the red line corresponding to 350°C and the black line to 450°C. To the right, the same pellet analyzed in wet argon with the red line corresponding to 350°C and the black line to 550°C.

As can be seen in the figure above, the resistance, i.e the value of the x-axis intercept, decreases as the temperature is increased. What is also clearly visible is the massive decrease in resistance when looking at the wet run compared to the dry run. The equivalent circuit used to evaluate the data consisted of a resistance and a constant phase element in parallel, further connected in series to another parallel resistance and constant phase element.

4.4.2 Conductivity during the heating-cooling cycle

Beginning with the BTS70-based samples, impedance spectroscopy was performed on two CIP-BTS70-W pellets from batch 2, namely pellet 1 and 3, in order to see if the higher density of pellet 1 would have any effect on the conductivity. The results will, of course, also be compared with the values found in literature, in the discussion section. The conductivity as a function of inverse temperature is shown in the figures below. Looking at the figure below, belonging to pellet 1, it can be seen that the conductivity of the heating run is higher than the cooling run during the combined heating-cooling (HC) cycle in dry argon, as is expected because the samples have likely hydrated before the heating run analysis while they are dehydrated during the subsequent cooling run. The reasons behind the general appearance of the HC conductivity graphs will be brought up in the discussion section, along with comparisons with conductivity values obtained in other studies.

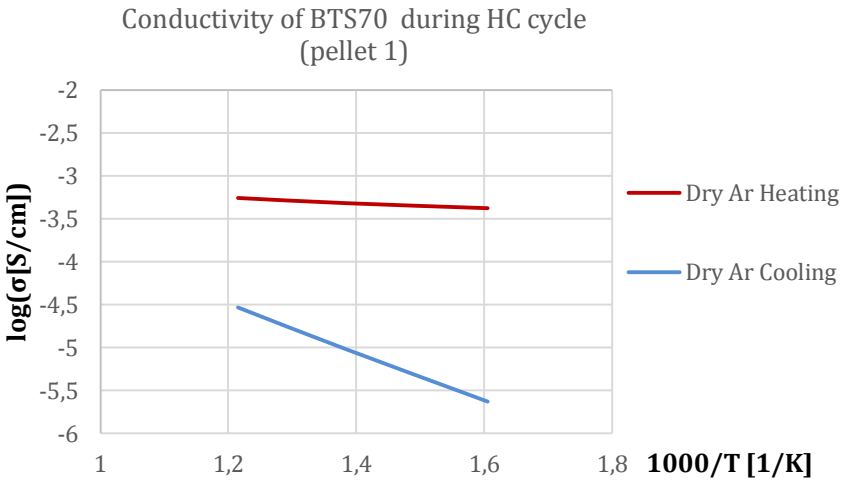

Figure 42. A figure showing the dependence of total conductivity on (inverse) temperature for CIP-BTS70-W (pellet 1) during a heating-cooling cycle in dry argon.

Looking at the same graph for pellet 3 the appearance is virtually identical, see figure 43. For any give temperature during the heating-cooling cycle, the conductivities of pellet 1 and 3 match closely. Again, the heating cycle gives conductivities between one and two orders of magnitude larger than the cooling cycle because of the protons present in the material during heating.

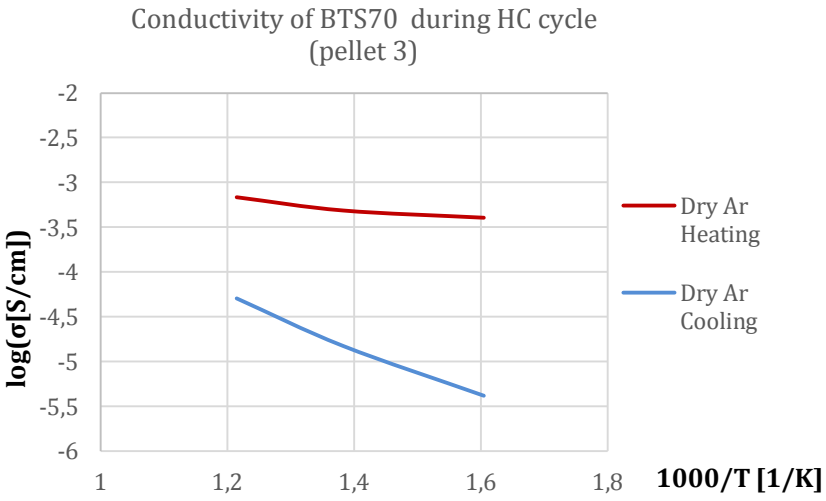

Figure 43. A figure showing the dependence of total conductivity on (inverse) temperature for CIP-BTS70-W (pellet 3) during a heating-cooling cycle in dry argon.

Examining the temperature dependence of the CIP-BTI70-W pellet's conductivity (pellet 3), see figure 44, it looks quite similar to the BTS70 samples, although it shows a slightly lower conductivity at the higher temperatures during the heating run than the BTS70 samples.

Comparing the heating and cooling cycles of the BTI70 sample reveals higher conductivities during heating than during cooling. It should be noted that only one BTI70 pellet was analyzed because two out of three pellets had virtually the same relative density, the third being too non-uniform to measure the dimensions accurately. Therefore, the conductivity results will later be compared only with values found in literature.

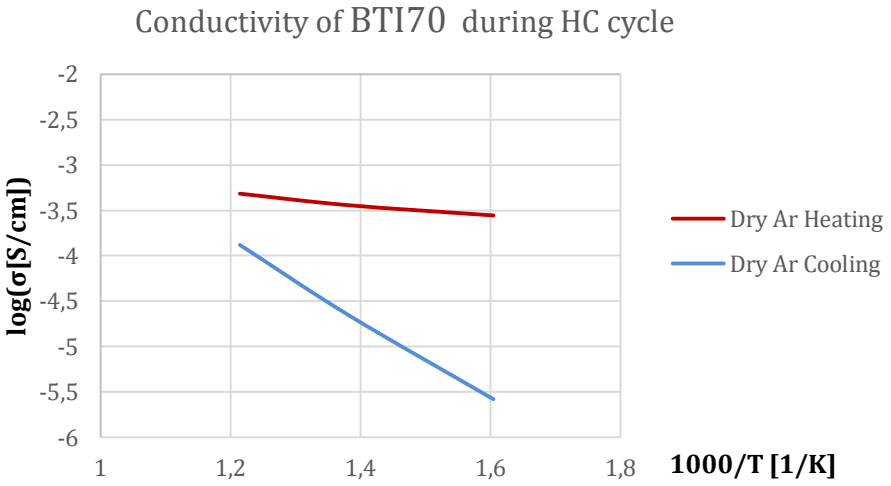

Figure 44. A figure showing the dependence of total conductivity on (inverse) temperature for CIP-BTI70-W (pellet 3) during a heating-cooling cycle in dry argon.

4.4.3 Conductivity during the wet and dry cooling

The same pellets subjected to the HC cycle were also subjected to cooling in wet and dry argon. Looking at the results for pellet 1 of the BTS70 CIP sample, shown in figure 45, the effect of the wet atmosphere on conductivity is apparent, yielding conductivities two orders of magnitude higher than in the dry atmosphere, indicating a large amount of proton conduction in the wet atmosphere.

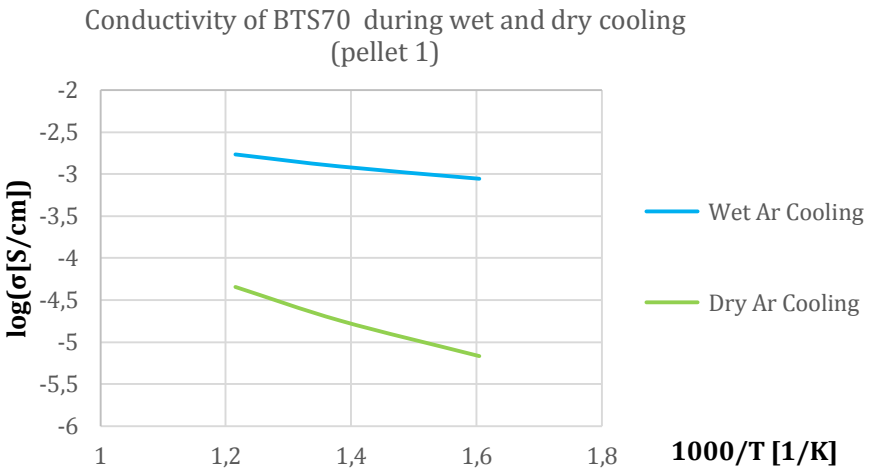

Figure 45. A figure showing the dependence of total conductivity on (inverse) temperature for CIP-BTS70-W (pellet 1) during cooling in wet and dry argon.

Examining figure 46 below, the conductivity values displayed by CIP-BTS70-W pellet 3 for the standalone dry cooling are much too high to be plausible. Comparing it to all other dry cooling runs (both during the HC cycles and during the standalone dry cooling) on all pellets, it is around two orders of magnitude higher, which is unreasonable. It is especially strange considering that the HC cooling run on the same pellet produced much more plausible results, in line with those obtained for the other samples, as shown in the figure below. It might be that the wrong atmosphere was used, i.e a wet argon atmosphere instead of a dry one, since the supposed dry run produces almost identical results to the wet run.

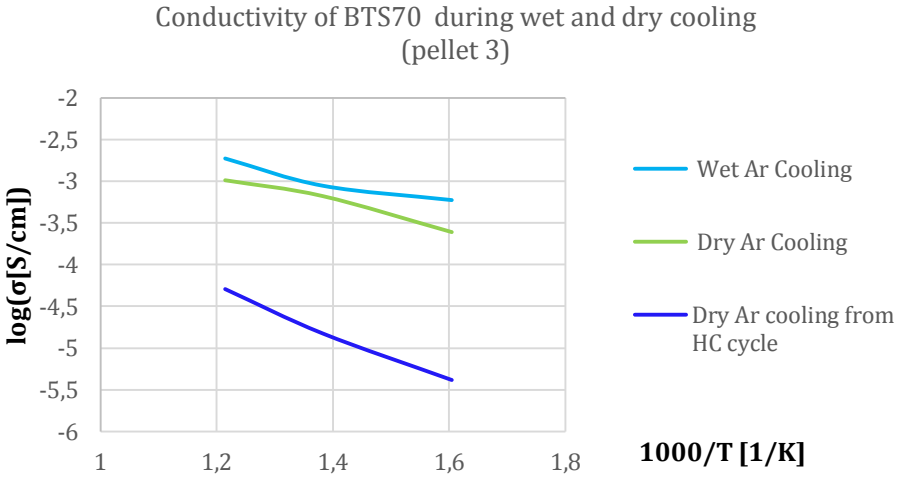

Figure 46. A figure showing the dependence of total conductivity on (inverse) temperature for CIP-BTS70-W (pellet 3) during cooling in wet and dry argon.

Looking at the CIP-BTI70-W sample, the wet run once again produces higher conductivities than the dry run, see figure 47. Comparing the BTI70 sample with the BTS70 samples, it shows a lower conductivity than them during the wet run. In contrast, the dry run shows similar conductivity at the higher temperatures although with a sharper decrease in conductivity as the temperature is lowered compared to the BTS70 samples.

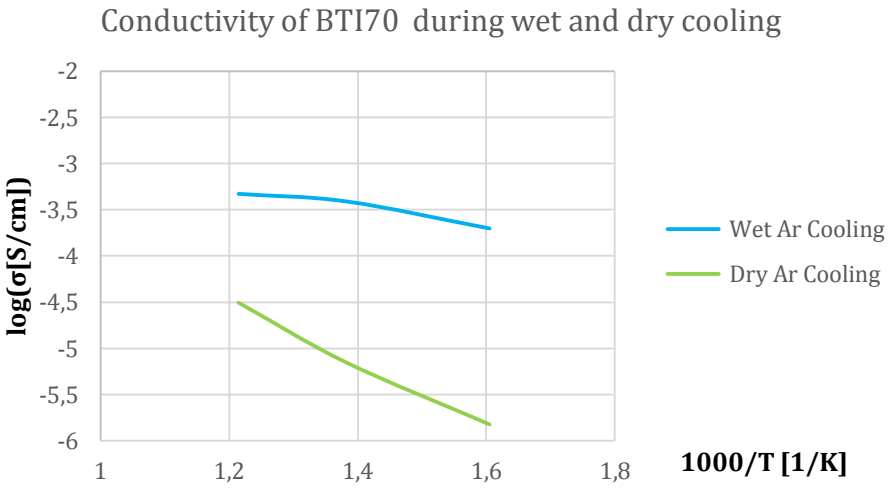

Figure 47. A figure showing the dependence of total conductivity on (inverse) temperature for CIP-BTI70-W (pellet 3) during cooling in wet and dry argon.

4.4.4 Activation energies

The activation energies calculated from the slope of Arrhenius plots, constructed from the data obtained through impedance spectroscopy, are displayed below for all analyzed samples. In addition, the quality of the linear fitting of the curve will be presented in terms of a factor, R^2. R^2 determines the quality of the fit between the linear regression model and the observed data points, the mathematical basis of which can be found in literature on statistics. Suffice to say, it relates the variance between the observed data and the modeled data to the variance within the observed data set.

Table 10. A table showing the activation energy for all three sample pellets analyzed using impedance spectroscopy, during the different heating and cooling cycles. The R^2-factor is also included to judge the quality of the linear fitting.

Sample	Cycle	Activation energy (eV)	R^2
CIP-BTS70-W #1	HC Heating/Cooling	0.12/0.62	0.9962/0.9998
	Dry cooling	0.48	0.996
	Wet cooling	0.21	0.9957
CIP-BTS70-W #3	HC Heating/Cooling	0.17/0.61	0.969/0.9959
	Dry cooling	0.38	0.9875
	Wet cooling	0.31	0.9545
CIP-BTI70-W #3	HC Heating/Cooling	0.18/0.92	0.9917/0.999
	Dry cooling	0.73	0.9952
	Wet cooling	0.25	0.9717

As can be seen in the table above the activation energy for dry cooling is always higher than that for wet cooling for each respective sample, indicating oxygen ion conduction as opposed to proton conduction. It should be mentioned, however, that the activation energies for the wet cooling and dry heating in this case are not truly meaningful for reasons brought up later, in the discussion section.

4.5 Scanning electron microscopy

In order to analyze the microstructure of selected processed samples, and give an indication of the correctness of the calculated relative densities, SEM was done on a CIP-BTI70-W and CIP-BTS70-W pellet from the second CIP batch. The BTI70 pellet had a density of approximately 98% while the BTS70 pellet had a density of nearly 84%.

Looking at the SEM pictures below of the surface of the BTI70 and BTS70 pellets, a distinct difference in microstructure can be seen. Firstly, the BTS70 pellet shows a more porous surface than the BTI70 pellet. In addition, the grain size is much smaller for BTS70 than BTI70, around 2µm compared to approximately 10µm. Furthermore, there are strange plate-like structures protruding from the BTS70 surface, approximately 10µm in diameter, whose origin and cause is unknown at present but discussed briefly later on.

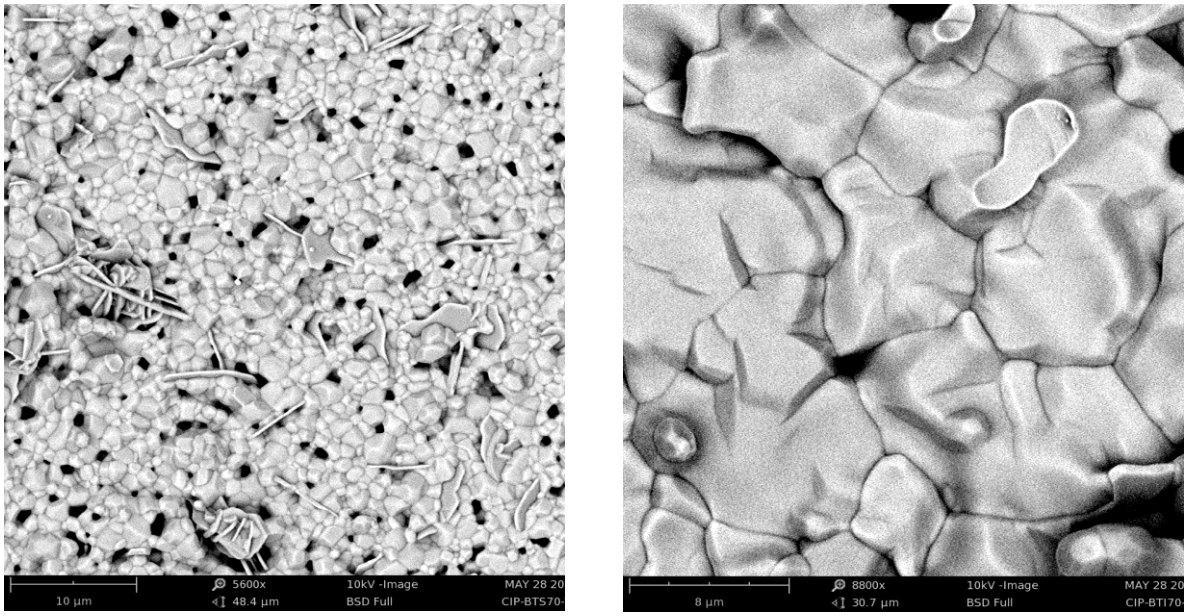

Figure 48. A figure showing two SEM pictures of the surface of a CIP-BTS70-W pellet (left) and a CIP-BTI70-W pellet (right). Note that the left figure has a 10µm scale for reference and the right picture an 8µm scale for reference.

Examining the SEM pictures of the fracture surface of the aforementioned pellets confirms the porous nature of the BTS70 pellet and the successful sintering and densification of the BTI70 pellet, see below.

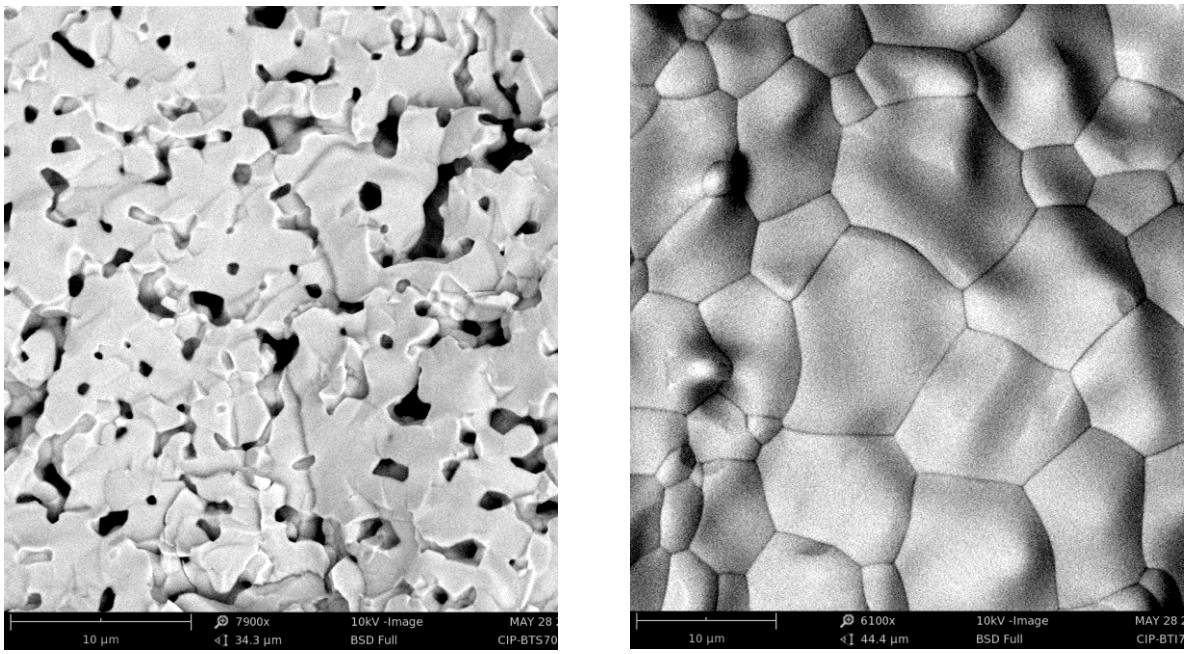

Figure 49. A figure showing two SEM pictures of the fracture surface of a CIP-BTS70-W pellet (left) and a CIP-BTI70-W pellet (right). Note that both pictures have a 10µm scale for reference.

5. Discussion

The results from XRD, TGA, impedance spectroscopy and SEM as well as the results regarding relative density are discussed in the following sections.

5.1 Perovskite phase development

The development of the perovskite phases of the different synthesized samples is discussed below, with references to the observed mass and volume losses which can be found in the appendix.

5.1.1 Trial samples vs tin samples

Comparing the results of X-ray diffraction between the different BTI70-based samples shows that all samples seem to achieve phase purity at 1400°C, displaying peaks corresponding to the perovskite phase. The most dramatic change from a multiphase material to a near pure perovskite occurs when sintered at 1200°C, irrespective of processing or addition of tin. The BTS70-based samples proved harder to purify, because although the processed BTS70 samples achieved phase purity after one sintering at 1500°C, the T-BTS70 and BSTS70 samples still retained impurities after two treatments at 1500°C and a treatment at 1550°C.

The impurities of the T-BTS70 sample were difficult to identify, made up of many low intensity peaks that matched the profile of barium deficient barium scandate. It is likely that one or several stable phases formed during high temperature sintering, perhaps owing to barium evaporation. Like T-BTS70, the sample of BSTS70 showed remnant impurities, although of a higher intensity, consisting of impurity phases identified as barium-deficient barium scandates, again indicating a potential loss of barium at the highest sintering temperatures. BSTS70 also show much larger mass losses at the higher sintering temperatures, see appendix, which increase considerably after the first 1500°C heating. The reason for the more prominent impurity phase and the larger mass losses of BSTS70 might be that the incorporation of tin in the perovskite structure, substituting titanium, reduces the stability of the A-ions (i.e Ba in this case) reducing the energy needed for them to escape the perovskite. Support for this can be found in literature. It has been suggested that large B-cations, being poorly compatible with the perovskite structure, will decrease the thermodynamic stability of the material. Looking at table 5 it can be seen that the ionic radius of tin is indeed larger than that of titanium, which it substitutes in the structure. If tin, being a large B-cation, would lower the thermodynamic stability of the material, an increased loss of barium at higher temperatures could be expected and is also what is observed. Furthermore, comparing the mass loss of BSTS70 with that of T-BTS70, which does not have tin in its structure, at the higher temperatures indicates that the incorporation of tin is in fact the reason behind these large mass losses. [21], [55]

In contrast to the detrimental impact of tin on the perovskite development of BTS70, the BSTI70 sample proved just as successful as its T-BTI70 cousin, achieving phase purity after sintering at 1400°C. The lower melting point of the indium oxide compared to scandium oxide seems to make a great difference in

the preparation of a pure barium titanate based perovskite. Adding tin seems to have adverse effects on the scandium containing samples, aggravating the purifying procedure, while the indium containing samples does not suffer from the introduction of tin in the material, at least in terms of phase purification. A plausible explanation is that since the scandium seems to need very high temperatures to be fully incorporated into the perovskite, the addition of tin oxide exacerbate the situation by substitution of the more temperature stable titanium oxide. When temperatures upwards of 1550°C are reached, some of the tin has been lost and consequently the stoichiometric ratio necessary for formation of the desired perovskite is shifted slightly. This could, in turn, lead to scandium forming other compounds, i.e impurities. Indium oxide on the other hand does not need these high temperatures and so the loss of tin is avoided.

5.1.2 Trial samples vs mixed Sc/In samples

The mixed BTSI35 and BTSI50 samples display, in principle, an identical perovskite phase development to the BTI70 sample. In likeness to all BTI70 based samples, both BTSI35 and BTSI50 display a dominant perovskite phase already at 1200°C which is not seen for any BTS70 sample. In addition they practially achieve phase purity at 1400°C, with miniscule impurities for the BTSI50 sample perhaps owing to the high scandium level in this sample. It can therefore be argued that the introduction of indium, even in the ratio In/Sc = 0.2/0.5, makes a very big difference in the perovskite development compared to BTS70. At a ratio of 0.35/0.35, any likeness to the BTS70 perovskite development has all but disappeared and makes it hard to even distinguish the X-ray diffractogram of the BTSI35 sample from that of a pure indium doped BTI70 sample, apart from the shift of the peaks. The observed losses of mass and volume seem to support these observations as the mixed Sc/In samples display hybrid-like behavior between that of BTS70 and BTI70.

5.1.3 Trial samples vs processed samples

Comparing the non-processed T-BTI70 samples with the cold isostatically pressed samples, it can be seen that while the dry pressed samples have not achieved phase purity at 1500°C the wet pressed samples actually have, suggesting that pure BTS70 samples can be achieved after one heating at 1500°C if the right preparations are made. Unsurprisingly, both the isostatically pressed BTI70 samples were phase pure after sintering at 1400°C much like T-BTI70.

The reason that the CIP-BTS70-D samples were not phase pure after their 1500°C sintering in contrast to the CIP-BTS70-W samples is probably due the effects of ball milling and cold isostatic pressing in achieving a tightly packed material, optimized for reaction and sintering of the particles. In addition, the fact that the slipcasted BTS70 sample, which was subjected to ball milling as well, did not achieve phase purity after its 1500°C sintering indicates the deciding part that cold isostatic pressing has to play in producing pure BTS70.

5.1.4 Suggested critical sintering temperatures

By looking at the phase development of all the samples it seems that the two critical temperatures for forming a pure perovskite phase is 1400°C for indium doped samples and 1500°C for scandium doped samples, the latter requiring proper preparations through e.g ceramic processing. The hybrid samples BTSI35 and BTSI50 seem to behave more like BTI70 than BTS70 in terms of sintering, having a perovskite forming temperature of 1400°C. The one sample that never reached phase purity was BSTS70 but it's not unthinkable that it might have done, using the same successful processing route that produced a pure BTS70 sample, i.e by ball milling and subsequent CIP:ing of the wet paste.

The fact that a sintering temperature of 1400°C and 1500°C seems critical in achieving a phase pure and dense sample, for the respective sample types, is supported by the recorded volume losses, see appendix, which show that the greatest volume loss takes place at these two temperatures for all samples. The only exception is the BSTS70 sample after its first 1500°C sintering. However, since this sample also displays an increasing amount of barium deficient impurities after its first 1500°C sintering, any large volume loss could very well have been caused by loss of barium.

5.2 Hydration and dehydration behavior

The hydration and dehydration behavior of the different sample sets is discussed in the following sections.

5.2.1 Trial samples vs tin samples

A summarizing table of some important results from TG analysis of the trial and tin samples, displayed below, shows that the onset and inflection point temperature follows a trend, with the indium samples having the two lowest onset and inflection temperatures, i.e they start to lose water at lower temperature than the scandium containing samples. On the other hand, the indium containing samples also display a higher hydration and consequently a larger proportion of their oxygen vacancies have been filled during the hydration treatment.

Table 11. A comparison of the onset-, inflection temperature and initial hydration of the hydrated trial and tin samples.

Sample	Onset temperature (°C)	Inflection temperature (°C)	Sample hydration
T-BTI70	177.7	283.0	90.8 %
BSTI70	191.7	315.9	99.8 %
T-BTS70	203.5	332.6	82.0 %
BSTS70	212.9	358.7	76.9 %

It should be noted, that the as-prepared samples of T-BTS70 and BSTS70 hydrated to a much larger extent at ambient conditions than T-BTI70 and BSTI70, as shown in the result section. According to a study on the hydration characteristics of indium and scandium substituted barium titanates, scandium

containing samples should in fact have a higher hydration enthalpy and hydrate to a larger extent than their indium counterparts, see [26]. The findings of that study show that the water uptake of BTS70 is much higher than that of BTI70 between 1000°C and 250°C. At 250°C and below however, the water uptake of BTI70 increases rapidly and the structure changes as it nears complete hydration, from a cubic to a tetragonal perovskite. Hydration of BTI70 close to the hydration limit is therefore not a single-phase reaction and the phase change might be what causes the increased water uptake. The XRD results of the hydrated T-BTI70 sample shows the emergence of the tetragonal phase after hydration which isn't surprising considering that the last stage of the hydration treatment took place at 150°C. It might be that T-BTI70 and BSTI70 show such large hydration levels compared to those obtained during ambient conditions because of this phase change from cubic to tetragonal upon extensive hydration. [26]

The progression of hydration shows me interesting results, where the tin samples display a greater ability to stabilize their protonic defects and therefore remain partly hydrated up to higher temperatures, see the summarizing table below.

Table 12. A summarizing table showing the three different levels of remnant hydration for the hydrated trial and tin samples and the corresponding temperature at which these hydration levels were reached during TG dehydration.

Sample	80% hydration	50% hydration	20% hydration
T-BTI70	264°C	302°C	350°C
BSTI70	281°C	332°C	393°C
T-BTS70	298°C	347°C	447°C
BSTS70	333°C	419°C	567°C

In addition, something which has already been mentioned, the scandium samples stay hydrated up to higher temperatures than the indium ones.

The fact that tin improves the high temperature remnant hydration goes against a correlation introduced by Norby et. al, see [25]. The correlation presented predicts that the smaller the difference in electronegativity between the A and B atom in an ABO_3 perovskite the more negative the enthalpy of hydration becomes. Looking at the table of electronegativity values below (Allred-Rochow scale), this would suggest that Sn, with an electronegativity value of 2.0 compared to that of Ti, 1.5, would be detrimental to the hydration thermodynamics of both BSTI70 and BSTS70 compared to T-BTI70 and T-BTS70. The difference in electronegativity between Ba and Ti is 0.6 while that between Ba and Sn is 1.1. In addition, the correlation predicts a large positive enthalpy of hydration for BTI70 because of the large difference in electronegativity between Ba and In, which would not result in hydration behavior displayed by T-BTI70. Instead, following from the correlation, the hydration of T-BTI70 would increase with temperature because of the endothermic hydration enthalpy. As noted by Bjørheim et. al., see [26], this correlation might be too simplistic and unsuitable for describing the hydration of these highly substituted perovskites.

Table 13. A table showing the electronegativity values of the constituent elements making up all samples synthesized for this study. The electronegativity values are reported on the Allred-Rochow scale. Values taken from [56].

Element	Electronegativity (Allred-Rochow scale)
Ba	0.9
Sc	1.4
Ti	1.5
In	1.8
Sn	2.0

The reason why tin improves the temperature stability of the hydrated BSTI70 and BSTS70 compared to BTI70 and BTS70, respectively, might seem hard to explain based on the electronegativity hypothesis presented above. However, even if the hypothesis would hold for high substitution levels, the discussion above only looks at the enthalpy term of the expression of Gibbs free energy. To be complete, one must also consider the entropy term which is likely affected, one way or another, by the introduction of tin in the BTS70 or BTI70 structure. As an example, it could be that the introduction of tin affects the degree of disorder among the oxygen vacancies and how this disorder changes during hydration, which in turn would have an impact on the entropy change during hydration and dehydration. Examining the results from [26] concerning hydration thermodynamics, it can be seen that both the enthalpy and entropy change of the hydration reaction of BTS70 and BTI70 are negative. In other words, for a given exothermic hydration reaction a smaller negative entropy change, giving a smaller positive $-T\Delta S$ term in the expression for Gibbs free energy, will mean that higher temperatures can be reached before dehydration is favored over hydration. It might be that the introduction of tin achieves this, in some way, although no explanation can be provided at this time.

5.2.2 Trial samples vs mixed Sc/In samples

By comparing and contrasting the results displayed in the two summarizing tables below, it could be argued that the hybrid samples have gained some positive characteristics from both purely indium substituted and purely scandium substituted barium titanate. Although they display low onset and inflection temperatures, akin to those of T-BTI70, they have simultaneously gained the trait of extensive hydration when purposefully hydrated, much like T-BTI70. The scandium present in these hybrid samples also seems to prevent the samples from turning into a tetragonal perovskite. This is of course very important if these materials are to be used as solid electrolytes in future fuel cells. A material which changes its crystal structure upon hydration will most likely not be mechanically stable as a fuel cell electrolyte since phase changes could cause internal strains in the material, producing cracks or other defects.

Table 14. A comparison of the onset-, inflection temperature and initial hydration of the hydrated trial and hybrid samples.

Sample	Onset temperature (°C)	Inflection temperature (°C)	Sample hydration
T-BTI70	177.7	283.0	90.8 %
BTSI35	153.3	283.2	100.4%
BTSI50	153.4	280.9	99.0 %
T-BTS70	203.5	332.6	82.0 %

The presence of scandium also appears to provide the mixed Sc/In samples with an increased ability to trap the protons present in the material, resulting in an increased temperature resistance in terms of dehydration compared to T-BTI70, although it is still lower than that of T-BTS70, see table below.

Table 15 A summarizing table showing the three different levels of remnant hydration for the hydrated trial and hybrid samples and the corresponding temperature at which these hydration levels were reached during TG dehydration.

Sample	80% hydration	50% hydration	20% hydration
T-BTI70	264°C	302°C	350°C
BTSI35	256°C	309°C	401°C
BTSI50	257°C	314°C	429°C
T-BTS70	298°C	347°C	447°C

5.2.3 Trial samples vs CIP-W samples

Looking at the table below, it can be seen that the onset and inflection temperatures of both CIP-W samples differ somewhat from their trial samples equivalents. Considering that the processed and non-processed samples have identical chemical formulas, one might not expect any differences. As was mentioned in the results section, however, the behavior of CIP-BTS70-W probably diverges from that of T-BTS70 because of the impurities present in the T-BTS70 sample. Another explanation for the dissimilarities is that when compared to those between the trial and tin samples, which are the most chemically dissimilar sample sets in his study, the differences are quite small.

One might argue that the differences are quite small between the hybrid samples and T-BTI70 and T-BTS70 also, even though they are chemically dissimilar. Shouldn't the processed samples therefore diverge less from the trial samples than the hybrid samples do? This is best answered by considering the fact that the hybrid samples are, in fact, chemical mixtures of T-BTI70 and T-BTS70 and so it is expected that some or all of their dehydration characteristics resemble either one of the trial samples, or both of them.

Table 16. A comparison of the onset-, inflection temperature and initial hydration of the hydrated trial and CIP-W samples.

Sample	Onset temperature (°C)	Inflection temperature (°C)	Sample hydration
T-BTI70	177.7	283.0	90.8 %
CIP-BTI70-W	168.2	275.0	96.2 %
T-BTS70	203.5	332.6	82.0 %
CIP-BTS70-W	183.0	316.6	97.1 %

The progression of dehydration for the CIP-W samples also seems to match the trial samples to a large extent. There are some differences, mainly the temperature at which CIP-BTI70-W has lost 20% of its water compared to T-BTI70. Another difference is the high temperature at which CIP-BTS70-W still retains 20% of its water, 480°C compared to 447°C for T-BTS70. As has been mentioned, T-BTS70 contained impurities, which might affect the dehydration behavior. All in all, the processed samples seem to display similar hydration and dehydration characteristics to their trial sample cousins, which is to be expected considering they're chemically identical.

Table 17. A summarizing table showing the three different levels of remnant hydration for the hydrated trial and CIP-W samples and the corresponding temperature at which these hydration levels were reached during TG dehydration.

Sample	80% hydration	50% hydration	20% hydration
T-BTI70	264°C	302°C	350°C
CIP-BTI70-W	248°C	293°C	348°C
T-BTS70	298°C	347°C	447°C
CIP-BTS70-W	288°C	350°C	480°C

5.3 Relative densities

The effect of the employed chemical modification and ceramic processing approaches on the relative density of BTI70 and BTS70 is examined below.

5.3.1 Trial samples vs chemically modified samples

The densities of the trial samples T-BTS70 and T-BTI70 seem to agree quite well with the densities achieved in previous studies, perhaps with some small improvements, see [6]-[7]. Comparing these values with those of the tin and mixed Sc/In samples shows that while altering the chemical formula of BTS70 and BTI70 might improve some characteristics of these materials, such the temperature at which a pure material can be achieved, the relative density seems to suffer in all the studied cases.

Contrary to what was expected, the introduction of tin did not help the densification of either the indium or scandium substituted barium titanate despite its relatively low melting temperature. In the BSTS70 case, in light of the discussion on the perovskite phase development, this might be related to the thermodynamic instability introduced by tin. If tin does lower the stability of this particular barium titanate structure, the sintering will likely be made more difficult, as small islands of barium deficient

material form, interspersed in the developing $BaSn_{0.15}Ti_{0.15}sc_{0.7}O_{3-\delta}$ phase. It is not unthinkable that these impurity phases might segregate to the surface of particles or aggregate in certain types of grain boundaries, giving rise to different interfaces in the material that are unwilling to merge during sintering. Looking at the BSTI70 sample, however, this explanation seems very unlikely as the material can be considered phase pure from its XRD scans. There might therefore be other factors in play that prevent the material from achieving a high density. One explanation that could apply to both tin samples is the possibility that their mechanical properties differ from the trial samples'. When these tin containing samples are ground in between sintering steps, for just as long as the trial samples even though they might have an improved hardness for example, the resulting sample powder might not be as fine and pose a hindrance to satisfactory sintering.

Looking at the hybrid samples it seems most fair to compare their densities with that of BTI70, considering they share the same final sintering temperature, unlike BTS70. It comes as no surprise that the introduction of scandium hampers the densification of the BTI70 sample since the melting temperature of scandium oxide is much higher than that of indium oxide, more than 500°C higher in fact. Furthermore, it can be seen that the more scandium that is part of the structure, the less dense the samples become, as illustrated by the declining trend going from BTI70 to BTSI35 to BTSI50.

5.3.2 Trial samples vs processed samples

It is no surprise that many of the isostatically pressed samples showed an increase in density compared to their axially pressed counterparts. It has been shown that cold isostatic pressing can have large effects on the green material density and the sintered material density by providing a better packing of particles as well as inducing other changes such as breakage of aggregates. [31], [33] What is surprising is that the dry pressed samples did not display as large an increase as one might expect, while the wet pressed samples fared much better. Since the dry pressed powder did not display nearly as large an improvement in density over the trial samples as the wet samples did, it seems that only performing cold isostatic pressing is not enough.

The reason why the majority of the wet CIP samples display a much greater density than their dry counterparts might be twofold. Firstly, the wet samples were ball milled which will likely have produced a sample powder with a narrower particle size distribution. The dry pressed samples had only been ground by hand using a mortar and pestle and not nearly for the same amount of time, 25 minutes compared to 12 hours of ball milling. It has been suggested that a narrow particle size distribution aids sintering kinetics as well as the densification of the material. Secondly, it could be theorized that pressing the powder as a paste, i.e with ethanol, could aid particle packing by decreasing friction and aiding interparticle slippage and particle rearrangement. This could produce a denser green material and consequently a denser sintered material. As an example, the low pressures needed to achieve dense materials during pressure slipcasting has been explained in this way and contrasted against the high pressures needed for dry powder cold isostatic pressing, see [58]. [57], [58]

The relative densities achieved by slipcasting indicate that the technique has the potential to produce highly dense barium titanate-based materials. However, as demonstrated by the results from the SC-

BTS70 sample, the technique relies on good sedimentation characteristics to achieve these high densities. When contrasting the relative density results against the results from XRD, it could also be argued that cold isostatic pressing might be a superior technique compared to slipcasting, at least for these materials. It seems that the act of isostatically pressing the wet powders improves the packing to the point that all the material can react to form a pure BTS70 sample. It stands to reason that this improved packing could also yield densities that cannot be matched by slipcasting alone. It should be stressed however, that there are improved versions of slipcasting involving surfactants, binders and high pressure which could likely produce samples of a very high final density after subsequent sintering.

5.4 Conductivities and activation energies

The results from impedance spectroscopy are considered below. The authors of study [8] have graciously supplied raw data from the mentioned study to facilitate comparison between the BTS70 conductivities reported there and the ones achieved in this study. Approximate BTI70 data has been gathered from graphs presented in the study [26]. Much like in the results section, conductivities will be displayed in logarithmic form to facilitate comparison with other studies and always refers to the total conductivity of the sample, since the contributions from the bulk and grain conductivity could not be separated. Consequently, only the total conductivities reported in other studies will be used for comparison.

5.4.1 Heating-cooling cycle

Looking at the graphs, in the result section, constructed from the heating-cooling cycle impedance data, all samples show a very flat conductivity curve during heating. Comparing with previous studies, see [6]-[8], it seems like both indium and scandium substituted titanates display a conductivity plateau between approximately 300^{o}C and 600^{o}C, corresponding to inverse temperature values (in K^{-1}) of 1.8 and 1.15. In other words, it is very plausible that the reason for the flat conductivity curve during heating of all three pellets is the fact that these samples are in the conductivity plateau at the temperatures for which reliable data could be extracted, i.e between 350 and 550^{o}C. This is further supported by the results from the subsequent dry cooling which displays a much steeper slope and no conductivity plateau in this range, as is expected from theory and from examining the previous studies mentioned. As a consequence, the activation energies calculated for the heating run are meaningless because the concentration of protons changes in the material during the dehydration which, together with the increasing mobility of the protons, is what gives rise to the plateau in conductivity.

To facilitate comparison between studies, impedance data on BTS70 from [8] have been incorporated with that presented in the results section, and the resulting figure for the dry heating and cooling runs is shown below.

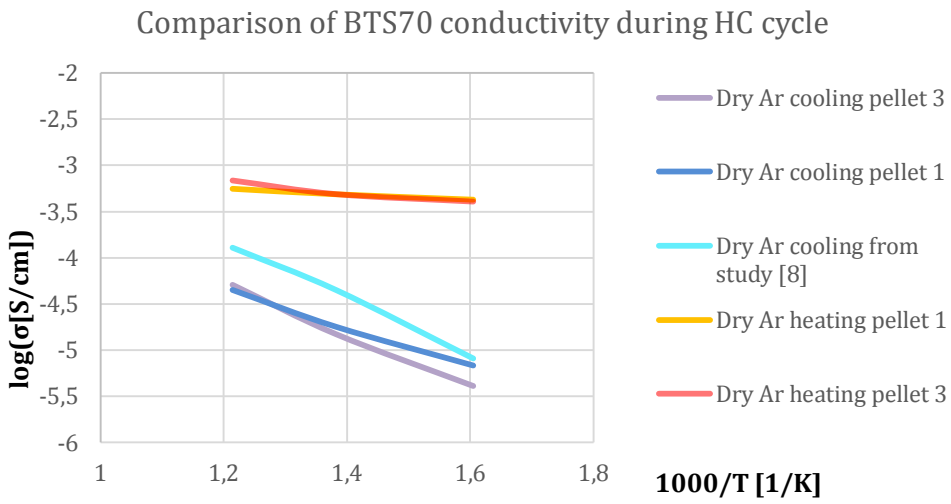

Figure 50. A figure comparing the dependence of total conductivity on (inverse) temperature for CIP-BTS70-W (pellet 1 and 3) with a BTS70 sample from [8], during dry heating and cooling in argon. Note that no dry argon heating run was reported in [8].

Looking at the figure above and comparing the conductivities during the dry cooling run on CIP-BTS70-W (pellet 1) with the results reported in [8], it is apparent that the conduction of other species than protons is higher in the material produced in [8], at these temperatures. Assuming that the materials are not hydrated to any meaningful extent at any point during this dry cooling, the only conduction is that of oxygen ions and not protons unless the material analyzed in the mentioned study wasn't dry before analysis. Doing a comparison with another study, although on BTS50, the reported logarithmic conductivity values in the same temperature range as the one considered in the present study, during heating and cooling in dry argon, are around -4.5 for the heating stage and -5.0 to -4.0 for the cooling stage. This matches with the values in the figure above quite well. Similarly, the activation energy of 0.63 eV, during dry cooling, matches very closely the value reported in [7] for a dry cooling run on a BTS50 sample in argon.

Examining the results from the CIP-BTI70-W sample by looking at the figure below, it can be seen that the conductivity is markedly lower than that reported in study [26]. Much like for BTS70 above, assuming the materials are dehydrated, it can be said that oxygen ion conduction seems to be higher in the BTI70 material of the mentioned study, in this temperature range.

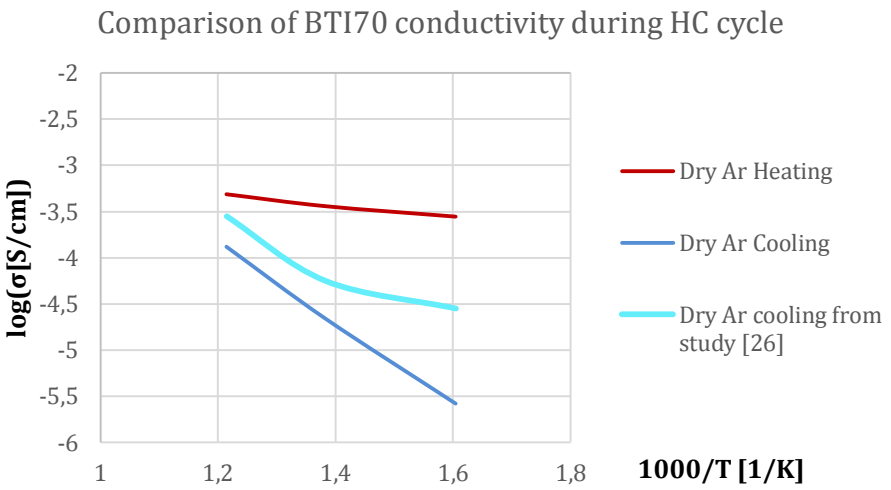

Figure 51. A figure comparing the dependence of total conductivity on (inverse) temperature for CIP-BTI70-W (pellet 3) with a BTI70 sample from [26], during dry heating and cooling in argon. Note that no dry argon heating run was reported in [26].

The conductivity values found for CIP-BTI70-W also matches that of a previous study on a similar material, BTI50. Reported values from this study, in the same temperature range, include a logarithmic conductivity value of approximately -4.0 to -6.0 during cooling in dry argon. A comparative value for a dry argon heating run has not been reported in that study. In the same study, an activation energy of 0.99 eV was reported for temperatures above 400°C, matching quite closely the value of 0.92 eV found in the present study between 350 and 550°C.

5.4.2 Wet and dry cooling

The same reasoning that was applied to explain the flat conductivity curve of the heating cycle can also be applied to the wet cooling cycle. As the sample is cooled in a wet atmosphere it should display the same type of conductivity plateau as during heating from ambient conditions, owing to the protons present in the material. The flat curves of the wet cooling runs on all analyzed pellets lie in the range where the conductivity plateau can be expected to appear. The resulting calculated activation energies will therefore, like for the heating cycle, be misleading.

Once again, to facilitate comparison, impedance data on BTS70 from [8] have been incorporated with that presented in the results section, and the resulting figure for the wet and dry cooling runs is shown below.

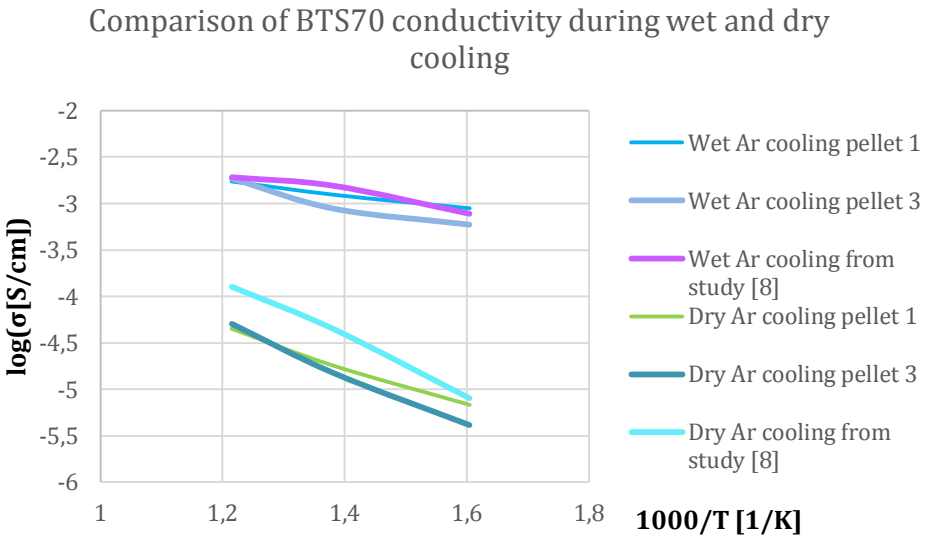

Figure 52. A figure comparing the dependence of total conductivity on (inverse) temperature for CIP-BTS70-W (pellet 1 and 3) with a BTS70 sample from [8], during wet and dry cooling in argon.

As can be seen in the figure above, hydrating BTS70 results in a massive increase in conductivity owing to the contribution from the protons in the material. It could be argued that pellet 1 displays a somewhat higher conductivity than pellet 3 in this specific temperature range, perhaps owing to the higher density of roughly 91% compared to 80%. The exact density of the BTS70 sample analyzed in [8] is not reported, instead a range of densities is given for all the analyzed samples of that study. The densities lie between 77 and 89%. If the specific BTS70 analyzed in that study was at the higher end of this range, it would lend some support to the notion that an increase in density can yield slight improvements in conductivity.

Comparing the isostatically pressed BTS70 samples with a similar, but not identical, sample of BTS50 they display conductivities almost one order of magnitude higher than that reported in [7]. The reason for the difference between the conductivity of the CIP pellets and that of BTS50 could be explained by either the higher density of the CIP pellets or the fact that BTS50 and BTS70 are chemically different. Most likely, a large part of the difference originates from the differing chemical makeup since the BTS70 pellet 3, whose density is not much higher than the reported BTS50 value, shows just as large a difference in conductivity as between pellet 1 and BTS50. This is supported by the fact that a BTS70 sample should most likely display a higher proton conductivity than a BTS50 sample because of the higher substitution level of scandium and consequently the larger amount of oxygen vacancies available for protonic defect formation.

Examining the impedance results of CIP-BTI70-W, the large increase in conductivity going from a dry to a wet argon atmosphere can be seen clearly. What is also visible is the shift towards higher conductivities for both the dry and wet run performed in [26] compared to the present study. This is surprising, considering that the relative density reported in the mentioned study was 80%, compared to the 98% of the CIP-BTI70-W pellet. Possible reasons for this difference include differences in microstructure, the

lack of reliable data and the difficulty with which it was evaluated. This will be elaborated on in the next section.

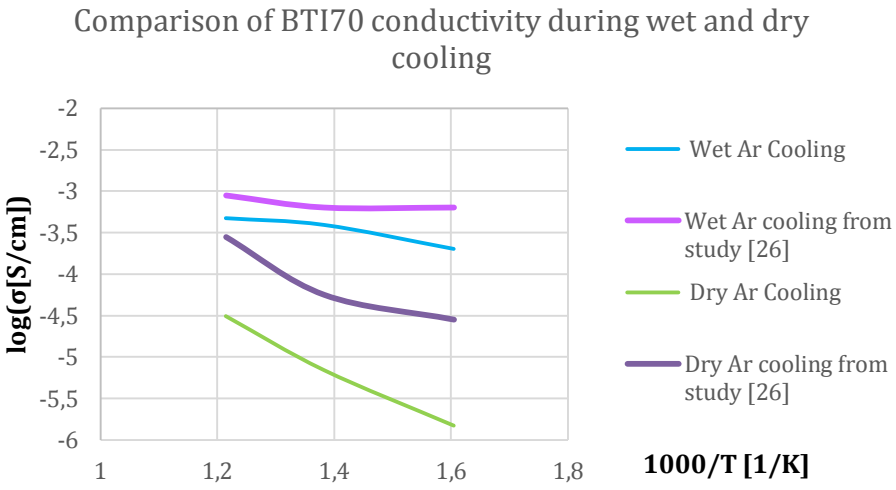

Figure 53. A figure comparing the dependence of total conductivity on (inverse) temperature for CIP-BTI70-W (pellet 3) with a BTI70 sample from [26], during wet and dry cooling in argon.

Comparing the results with those on a BTI50 sample from [6], it seems the standalone dry cooling run yields conductivities that match closely the logarithmic conductivity range -4.0 to -6.0 obtained in [6]. Similarly, the wet cooling run's value of -3.3 is in good agreement with the value of around -3.5 obtained at approximately 550°C in [6]. Assuming the data is reliable this difference in conductivity could stem from either the higher density of the CIP sample, roughly 98% compared to 82%, or from the fact that BTI50 is chemically different from BTI70, as discussed for the scandium samples above.

Looking at the activation energies it seem like the dry cooling run gives a reasonable value of roughly 0.73 eV, although it is quite a bit lower than the value of 0.92 eV obtained from the cooling run in the HC cycle . Once again, the wet run also yields an unreasonably small value for the activation energy for reasons which have already been explained.

5.4.3 Conductivity versus density

The reason why the conductivity of BTS70 and BTI70 show only a slight, or no, dependence on density is difficult to determine. Firstly, there are experimental factors to take into consideration. While measurement of pellet dimensions is a quick and easy way of obtaining relatively accurate estimates of volume, there are other approaches such as the Archimedean method that might have yielded more accurate dimensions and consequently better density estimates. As a consequence of the measurement errors, the calculated densities might be slightly different. This could mean that samples which, presently, are deemed to have very different densities are in fact more alike in this respect than what was thought. Subsequent analysis of these two chemically identical pellets with similar density would

then yield similar conductivity data. In addition, as has already been mentioned, a large part of the impedance data was difficult to evaluate and the conductivity results might not be completely reliable as a consequence.

Apart from experimental error factors, there are many other factors affecting the total conductivity of a sample, such as the microstructure of the sample or impurities present on the surface. Slightly different conditions during some of the synthesis steps such as grinding, sintering and processing will affect the final microstructure. Moreover, the samples with which the CIP samples are compared have not been put through ceramic processing and their microstructure might be very different in comparison.

5.5 Microstructure

Looking at the SEM results, the lower relative density of the particular BTS70 pellet compared to the BTI70 pellet is confirmed by the much greater porosity of the BTS70 pellet. In addition, the grain size of the BTI70 pellet was much larger than that of BTS70 which consequently means less grain boundaries and perhaps a lower grain boundary resistance, although confirmation of this cannot be found in the impedance data as it could not be separated into the bulk and grain boundary contributions.

Regarding the unusual plate like structures protruding from the BTS70 pellet, it seems similar structures were not found in previous studies, see [7] and [8]. These plates might therefore originate from the differences in processing that the samples have been subjected to, compared to those in the mentioned studies. It might also be that the plates are mainly made up of impurities, although the BTS70 sample was found to be phase pure by XRD and the SEM images suggest that the extent of plate formation is quite large, large enough to perhaps give rise to an impurity peak if that was the case.

6. Conclusions

It has been found that both BTS70 and BTI70 crystallize in the cubic Pm-3m perovskite structure which in the case of BTI70 and BSTI70 transforms to a tetragonal structure when extensively hydrated. While BTI70 was found to be phase pure after one sintering at 1400°C, pure BTS70 was harder to synthesize and wasn't made pure without the use of ceramic processing techniques and one sintering at 1500°C. Without processing, BTS70 did not reach phase purity even after two sinterings at 1500°C and one at 1550°C. The introduction of tin had no effect on the ability of indium substituted barium titanate to achieve phase purity, but aggravated the situation for the scandium doped counterpart, resulting in even more pronounced impurities than for BTS70. The mixed scandium/indium samples both reached phase purity at 1400°C, indicating that indium present even in small substitution levels can aid the perovskite development of BTS70.

The relative densities of BTS70 and BTI70, i.e 85 and 87%, were improved upon by ceramic processing. The highest densities were achieved through the combination of ball milling and cold isostatic pressing, which produced BTS70 and BTI70 samples with relative densities as high as 93 and 98%, respectively. It can be said with confidence that the densities of scandium and indium substituted barium titanates can

be improved by the use of ball milling in combination with cold isostatic pressing. The use of slipcasting has the potential to produce materials of high density but demands more optimization and micromanagement to be a reliable alternative. Scanning electron microscopy, although only performed on one wet pressed CIP-BTI70 and CIP-BTS70 pellet, gave an indication of the correctness of the calculated relative densities and revealed a larger grain size of 10μm in the BTI70 sample compared to the 2μm of the BTS70 sample.

The chemical modification approach did not enhance the density of the samples, but did produce some interesting results in terms of hydration. The incorporation of tin seems to stabilize the protonic defects in both BTI70 and BTS70, allowing them to remain partly hydrated to significantly higher temperatures, as well as increase the extent of hydration for BTI70 , though not for BTS70. In contrast, the mixed scandium/indium samples achieved higher hydration levels than both BTS70 and BTI70. In addition, the presence of scandium in these samples seems to help maintain remnant hydration up to higher temperatures compared to BTI70 as well as prevent the transformation to a tetragonal perovskite when extensively hydrated.

No definitive conclusions can be drawn on the impact of density on the conductivity of BTS70 and BTI70. What can be said with relative certainty is that the conductivities achieved seem to be comparable to those reported in other studies. Results from impedance spectroscopy, along with TG analysis, strongly indicates the proton conducting nature of both BTS70 and BTI70 and that both materials are capable of extensive hydration.

Future work

The most promising of the densification routes seems to be that involving ceramic processing and not chemical modification. Therefore, further work focusing on just optimizing the cold isostatic pressing approach seems reasonable. In order to examine if it's the pressing of the sample as an ethanol-impregnated paste that has a dominating effect on the final density, and not the previous ball milling, experiments involving ball milled and dried powders (instead of pastes) being put into a cold isostatic press could be examined in the future. In addition, investigations into optimizing the slipcasting route through introduction of binders and surfactants in the suspension would be prudent. Furthermore, studies where the microstructure is investigated to a larger extent and optimized along with density would perhaps give more control over the conductivity results.

Although the chemical modification approach did not yield samples with an improved density, it did produce samples with interesting hydration characteristics. Further study involving the hybrid, or mixed, scandium/indium samples and the tin substituted samples could reveal interesting hydration thermodynamics that could be used improve the proton conducting behavior of these types of materials. Understanding the underlying mechanisms behind the tin-induced improvements in temperature stability could prove fruitful.

References

[1] Pachauri, R.K. et al. (2014) *Climate Change 2014 Synthesis Report - Summary for Policymakers*

[2] Stambouli, A.B. & Traversa, E. (2002) Solid oxide fuel cells (SOFCs): a review of an environmentally clean and efficient source of energy. *Renewable and Sustainable Energy Reviews*, vol. 6, no. 5, pp. 433-455.

[3] Badwal, S.P.S. & Foger, K. (1996) Solid oxide electrolyte fuel cell review, *Ceramics International*, vol. 22, no. 3, pp. 257-265.

[4] Ormerod, R.M. (2003) Solid oxide fuel cells, *Chemical Society Reviews*, vol. 32, no. 1, pp. 17-28.

[5] Kawamoto, H. (2007) Research and Development Trends in Solid Oxide Fuel Cell Materials - From the Viewpoint of Electrolyte-Related R&D as Key, *Quarterly review*, no. 26, pp. 52-70.

[6] Rahman, S.M.H. et al. (2012) 50 mol% indium substituted BaTiO3: Characterization of structure and conductivity. *International Journal of Hydrogen Energy*, vol 37, no. 9, pp. 7975-7982.

[7] Rahman, S.M.H. et al. (2014) Characterization of structure and conductivity of BaTi0.5Sc0.5O3−δ. *Solid State Ionics*, vol. 255, pp. 140-146.

[8]Rahman, S.M.H. et al. (2014) Proton conductivity of hexagonal and cubic BaTi1−xScxO3−δ (0.1 ≤ x ≤ 0.8). *Dalton transactions*, vol. 43, no. 4, pp. 1555-1564.

[9] Norby, T. (1999) Solid-state protonic conductors: principles, properties, progress and prospects. *Solid State Ionics*, vol. 125, no. 1, pp. 1-11.

[10] Babilo, P. et al. (2007) Processing of yttrium-doped barium zirconate for high proton conductivity. *Journal of Materials Research*, vol. 22, no. 5, pp. 1322-1330.

[11] Liu, Y. et al. (2013) A novel approach for substantially improving the sinterability of BaZr0.4Ce0.4Y0.2O3-δ electrolyte for fuel cells by impregnating the green membrane with zinc nitrate as a sintering aid. *Journal of Membrane Science*, vol. 437, pp. 189-195.

[12] Park, I. et al. (2013) Enhanced sintering behavior mechanism of nanocrystalline BaCe0.8Sm0.2O3-d by Cu doping. *International Journal of Hydrogen Energy*, vol 38, no. 18, pp. 7423-7429.

[13] Muccillo, R. et al. (2012) Densification and enhancement of the grain boundary conductivity of gadolinium-doped barium cerate by ultra fast flash grain welding. *Journal of the European Ceramic Society*, vol. 32, no. 10, pp. 2311-2316.

[14] Azad, A. et al. (2008) High density and low temperature sintered proton conductor BaCe0.5Zr0.35Sc0.1Zn0.05O3–δ. *Solid State Ionics*, vol. 179, no. 19-20, pp. 678-682.

[15] Kreuer, K.D. (2003) Proton-conducting oxides. *Annual Review of Materials Research*, vol. 33, no. 1, pp. 333-359.

[16] Amsif, M. et al. (2009) Synthesis and characterisation of BaCeO3-based proton conductors obtained from freeze-dried precursors. *Journal of the European Ceramic Society*, vol. 29, no. 1, pp. 131-138.

[17] Amsif, M. et al. (2012; 2011) Low temperature sintering of LaNbO4 proton conductors from freeze-dried precursors. *Journal of the European Ceramic Society*, vol. 32, no. 6, pp. 1235-1244.

[18] Di Vona, M.L., Knauth, P. (2012) *Solid state proton conductors: properties and applications in fuel cells*. Oxford. Wiley-Blackwell.

[19] Paddison, S.J. & Promislow, K. (2009) *Device and materials modeling in PEM fuel cells*. New York; London. Springer.

[20] Hempelmann, R. (1996) Hydrogen diffusion mechanism in proton conducting oxides. *Physica B: Physics of Condensed Matter*, vol. 226, no. 1, pp. 72-77

[21] Kreuer, K.D. (2003) Proton conducting oxides. *Annual Review of Materials Research*, vol. 33, no. 1, pp. 333-359.

[22] Rooksby, H. P. et al., (1945) Compounds of the structural type of calcium titanate. *Nature*, vol 152, pp. 484-485.

[23] Lesley E. Smart, Elaine A. Moore. (2012) *Solid State Chemistry – An Introduction*. Fourth Edition. Boca Raton. Taylor and Francis Group.

[24] Iwahara, H. (1996) Proton conducting ceramics and their applications. *Solid State Ionics*, vol. 86-8, pp. 9-15.

[25] Norby, T. et al. (2004) Hydrogen in oxides. *Dalton Transactions*, no. 19, pp. 3012-3018.

[26] Bjørheim, T.S. et al. (2015) Hydration thermodynamics of the proton conducting oxygen-deficient perovskite series BaTi1- xMxO3- x /2 with M = in or Sc. *Inorganic Chemistry*, vol 54, no. 6, pp. 2858-2865.

[27] Gibson, I.R. et al. (1998) Sinterability of commercial 8 mol% yttria-stabilized zirconia powders and the effect of sintered density on the ionic conductivity. *Journal of Materials Science*, vol. 33, no. 17, pp. 4297-4305.

[28] Schouler, E.J.L. et al. (1983) In situ study of the sintering process of yttria stabilized zirconia by impedance spectroscopy. *Solid State Ionics*, vol. 9, no. 2, pp. 989-996.

[29] Badwal, S. P. S. et al. (1987) Yttria-zirconia: effect of microstructure on conductivity. *Journal of materials science*, 1987, vol 22, no. 9, pp. 3231-3239.

[30] Wachtman, J.B., Cannon, W.R., Matthewson, M.J. (2009) Mechanical properties of ceramics. Second edition. Hoboken, N.J. John Wiley & Sons.

[31] Baláž, P. (2008). Mechanochemistry in nanoscience and minerals engineering. Berlin; London. Springer.

[32] P.E. Price. (1998) Cold Isostatic Pressing. *Shaping and Consolidation Technologies*, Vol 7, *Powder Metal Technologies and Applications*, ASM International, p 382–388.

[33] Galusek, D. et al. (1999) The influence of cold isostatic pressing on compaction and properties of Mg-PSZ ceramics. *Journal of Materials Science Letters*, vol. 18, no. 16, pp. 1347-1351.

[34] Kamiya, H. et al. (1998) Densification of sol-gel-derived mullite ceramics after cold isostatic pressing up to 1 GPa. *Journal of the American Ceramic Society*, vol. 81, no. 1, pp. 173-179.

[35] Refractory materials – A series of monographs, volume 5. New York. Academic press.

[36] Rietveld, H.M. (1967) Line profiles of neutron powder-diffraction peaks for structure refinement. *Acta Crystallographica*, vol. 22, no. 1, pp. 151-152.

[37] Rietveld, H.M. (1969). A profile refinement method for nuclear and magnetic structures. *Journal of Applied Crystallography*, vol. 2, no. 2, pp. 65-71.

[38] McCusker, L.B et al. (1999) Rietveld refinement guidelines. *Journal of Applied Crystallography*, vol. 32, no. 1, pp. 36-50.

[39] Will, G. 2006. Powder Diffraction: The Rietveld Method and the Two-Stage Method. New York. Springer-Verlag.

[40] (2010) Thermogravimetric Analysis (TGA) – A Beginners Guide. *PerkinElmer*. http://www.perkinelmer.com/CMSResources/Images/44-74556GDE_TGABeginnersGuide.pdf (2015-01-27)

[41] (2013) Differential Scanning Calorimetry (DSC) – A Beginners Guide. *PerkinElmer*. http://www.perkinelmer.com/CMSResources/Images/44-74542GDE_DSCBeginnersGuide.pdf (2015-03-19)

[42] Swapp, S. (2012) Scanning Electron Microscopy (SEM). The Science Education Resource Center at Carleton College. http://serc.carleton.edu/research_education/geochemsheets/techniques/SEM.html (2015-01-27)

[43] Scanning Electron Microscope. *Purdue University*. http://www.purdue.edu/ehps/rem/rs/sem.htm (2015-01-27)

[44] (2009) Scanning Electron Microscopy. *Materials Evaluation and Engineering, Inc*. http://mee-inc.com/sem.html (2015-01-27)

[45] Basics of Electrochemical Impedance Spectroscopy. *Gamry*. http://www.gamry.com/application-notes/basics-of-electrochemical-impedance-spectroscopy/ (2015-01-26)

[46] Phase. *Hyperphysics*. http://hyperphysics.phy-astr.gsu.edu/hbase/electric/phase.html (2015-01-26)

[47] Reactance and Impedance. *All about circuits*. http://www.allaboutcircuits.com/vol_2/chpt_5/1.html (2015-01-26)

[48] Fitzpatrick, R. (2007) Capacitors in DC Circuits. http://farside.ph.utexas.edu/teaching/302l/lectures/node60.html (2015-01-26)

[49] Barsoukov, E. & Macdonald, J.R. (2005) *Impedance spectroscopy: theory, experiment, and applications*. Hoboken, New Jersey. Wiley-Interscience.

[50] Orazem, M.E., Tribollet, B. (2008) *Electrochemical impedance spectroscopy*. Hoboken, New Jersey. Wiley.

[51] Shannon, R.D. (1976) Revised effective ionic radii and systematic studies of interatomic distances in halides and chalcogenides. *Acta Crystallographica Section A: Crystal Physics, Diffraction, Theoretical and General Crystallography*, vol. 32, no. 5, pp. 751-767.

[52] Larson, A.C. & Von Dreele R.B. (1994). General Structure Analysis System (GSAS). *Los Alamos National Laboratory Report LAUR 86-748*.

[53] Momma, K. & Izumi, F. (2011). VESTA 3 for three-dimensional visualization of crystal, volumetric and morphology data. *Journal of Applied Crystallography*, vol. 44, no. 6, pp. 1272-1276.

[54] Quarez, E. et al. (2010) Water incorporation and proton conductivity in titanium substituted barium indate. *Journal of Power Sources*, vol. 195, no. 4, pp. 1136-1141.

[55] Kreuer, K.D. (1997) On the development of proton conducting materials for technological applications. *Solid State Ionics*, vol. 97, no. 1, pp. 1-15.

[56] Allred-Rochow Electronegativity. *University of California, Davis*.

http://chemwiki.ucdavis.edu/Physical_Chemistry/Physical_Properties_of_Matter/Atomic_and_Molecular_Properties/Electronegativity/Allred-Rochow_Electronegativity (2015-05-15)

[57] Chappell, J.S. et al. (1986) Particle size distribution effects on sintering rates. *Journal of Applied Physics*, vol. 59, no. 1, pp. 383-391.

[58] Papitha, R. et al. (2013) Pressure slipcasting and cold isostatic pressing of aluminum titanate green ceramics: A comparative evaluation. *Processing and Application of Ceramics*, vol. 7, no. 4, pp. 159-166.

Appendices

Appendix A – Calculations

Calculations that have been performed, using data and results obtained during the course of the study and which aren't considered trivial, are included in the sections below.

A1. Theoretical density

The theoretical density of a crystalline solid can be calculated by dividing the weight of the constituent atoms of the unit cell with the volume of the unit cell, according to equation A1 below.

$$\rho_{theoretical} = \frac{N_c * A}{N_A * V_c} \qquad \frac{[\#\ atoms]*[\frac{kg}{mol}]}{[\frac{\#\ atoms}{mol}]*[m^3]} = \frac{[\#\ atoms]*[kg]*[mol]}{[\#\ atoms]*[m^3]*[mol]} = \frac{[kg]}{[m^3]} \qquad \text{(A1)}$$

Where N_c is the number of atoms in the unit cell, A the atomic weight, N_A Avogadros number and V_c the unit cell volume.

A1.1 Relative density of a T-BTS70 sample sintered at 1500°C (Calculation example)

The relative density is the ratio between the measured, or actual, density of a sample and the theoretical density. The theoretical density can be calculated from data regarding the unit cell and its dimensions while the actual density of the T-BTS70 pellet can be calculated from its measured dimensions and weight.

$$\rho_{pellet} = \frac{m_{pellet}}{V_{pellet}} \qquad \text{(A2)}$$

$$V_{pellet} = \pi r^2 * h = \pi \left(\frac{d}{2}\right)^2 * h \qquad \text{(A3)}$$

Where d and h is the measured diameter and thickness, respectively. So for the T-BTS70 sample after sintering at 1500°C:

$$V_{pellet} = \pi \left(\frac{d}{2}\right)^2 * h = \pi \left(\frac{14.84}{2}\right)^2 * 2.41 = \ 416.845\ mm^3 = 4.17 * 10^{-7} m^3$$

$$\rho_{pellet} = \frac{m_{pellet}}{V_{pellet}} = \frac{1.8313\ g}{4.17*10^{-7} m^3} = \ \frac{1.8313*10^{-3}\ kg}{4.17*10^{-7} m^3} = 4391.61\ \frac{kg}{m^3}$$

The theoretical density takes slightly more effort. The atomic weight and Avogadros number can be found in tables, but the unit cell volume needs to be elucidated from characterization of the material, using XRD, by determining the unit cell parameter(s). The number of each atom in a unit cell is easily determined by looking at the chemical formula, $BaTi_{0.3}Sc_{0.7}O_{2.65}$.

$$\rho_{theoretical} = \frac{N_c * A}{N_A * V_c} = \frac{(N_{Ba} * A_{Ba}) + (N_{Ti} * A_{Ti}) + (N_{Sc} * A_{Sc}) + (N_O * A_O)}{N_A * V_c} =$$

$$= \frac{(1 * 137.327 * 10^{-3}) + (0.3 * 47.867 * 10^{-3}) + (0.7 * 44.9559 * 10^{-3}) + (2.65 * 15.9994 * 10^{-3})}{(6.022 * 10^{23}) * V_c}$$

Where N_c is the number of each atom in a unit cell, A is the atomic weight of the specific atom, N_A is Avogadros number and V_c is the unit cell volume.

Assuming a cubic unit cell:

$$V_c = a^3 \qquad \text{(A4)}$$

Where "a" is the unit cell parameter, i.e. the unit cell length, width and height (since it is cubic). From XRD analysis, a was determined to be 4.17 Å.

$$V_c = a^3 = (4.17)^3 = 72.51\ Å^3 = 72.51 * 10^{-30} m^3$$

$$\rho_{theoretical} = \frac{(1 * 137.327 * 10^{-3}) + (0.3 * 47.867 * 10^{-3}) + (0.7 * 44.9559 * 10^{-3}) + (2.65 * 15.9994 * 10^{-3})}{(6.022 * 10^{23}) * (72.51 * 10^{-30})} = 5152.69\ \frac{kg}{m^3}$$

The relative density can now be calculated:

$$\rho_R = \frac{\rho_{pellet}}{\rho_{theoretical}} = \frac{4391.61}{5152.69} = 0.85 = 85\ \% \qquad \text{(A5)}$$

A2. Degree of hydration of a hydrated T-BTI70 sample sintered at 1400°C (Calculation example)

The percent hydration of a sample can be calculated by comparing the recorded mass loss of the sample with the maximum theoretical mass loss that would be observed if a fully hydrated sample was completely dehydrated. The first step is noting that the molar mass of the sample will change as water is lost during dehydration. It is assumed, of course, that only water is lost as the sample is heated. Calculating the ratio between the molar mass of a completely dry and fully hydrated sample shows what the minimum residual

mass, i.e mass of the dry sample, will be after a TG analysis, as a percent of the initial mass of the hydrated sample:

$$R_{min} = \frac{M_{dry\ sample}}{M_{hydr.\ sample}} = \frac{274.4581}{280.7634} = 0.9775 = 97.75\ \% \qquad \text{(A6)}$$

So, if a sample displays a residual mass of 97.75 %, it will have gone from fully hydrated to dry during the TG analysis. Note that if the residual mass, in percent, is higher than this number it corresponds to an originally less hydrated sample.

The maximum possible mass loss for a fully hydrated sample can now be calculated:

$$\Delta m_{max} = 1 - R_{min} = \ 0.0225 = 2.25\ \% \qquad \text{(A7)}$$

The mass loss of the "real" sample can then be compared with this maximum theoretical mass loss to give the percent hydration.

The thermogravimeter records the changes in sample mass and can provide data on the mass of the dry sample, i.e the residual mass, as a percent of the initial mass of the hydrated sample. Using the data for the T-BTI70 sample, the residual mass was measured to be 97.96 % giving a percentage mass loss of 2.04%. Taking the ratio between this mass loss and that of equation A7, the percent hydration of the hydrated sample can be calculated:

$$H = \frac{\Delta m_{sample}}{\Delta m_{max}} = \frac{2.04}{2.25} = 0.907 = 90.7\ \% \qquad \text{(A8)}$$

A3. Measuring and calculating the density of a pellet fragment

This method of measuring a sample's density relies on Archimede's principle, i.e: The magnitude of the buoyancy force is equal to the weight of the displaced fluid the object is submerged in, i.e $F_b = m_{w,d}*g$. One can use many different fluids for this purpose and in this case ethanol was used.

Simple case (non- or closed-porous sample):

For the simple case, the sample is submerged while tied to a string so that it's suspended in the middle of an ethanol filled container. By suspending the sample in the liquid and not putting it on the bottom of the container one can calculate the volume of displaced liquid using a precise scale, instead of measuring the actual displaced volume of water (which can be inaccurate if you don't have proper equipment).

Looking at the figure below, it can be seen that the gravitational force downwards, F_g is counteracted by the force from the string, F_t, and the buoyancy force, F_b. The only force out of the three that is exerted on the scale is the buoyancy force (as a mental image, think of it as a column of water holding up the sample pellet with force F_b. The water column must stand on something, right? E.g the scale).

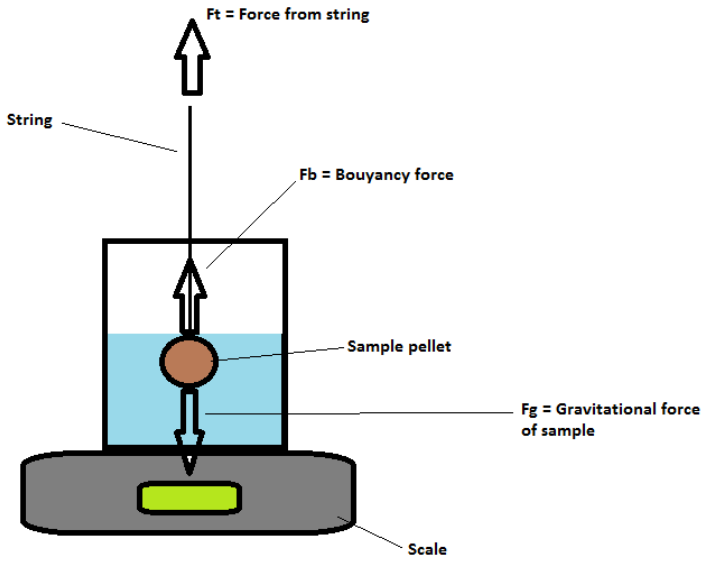

So the scale registers a weight corresponding to F_b.

Archimede's principle: The magnitude of the buoyancy force is equal to the weight of the displaced fluid the object is submerged in, i.e: $F_b = m_{e,d}*g$.

$$F_b = m_{e,d} * g \qquad \text{(A9)}$$

Where $m_{e,d}$ is the mass of displaced ethanol and g is the gravitational constant.

Using equation A9 the weight of displaced ethanol $m_{e,d}$ can be obtained and, knowing the density of ethanol, the displaced volume. Consequently one gets the volume of the sample.

Complicated case (open porous sample):

For open porous samples, as in this case, it's a bit more complicated because now the sample pores, which can absorb liquid, have to be accounted for. For simplicity, imagine that the sample has only one big pore in the center, with a small channel for the liquid to enter it through. Let's say the pore gets completely filled with ethanol. The apparent weight of the sample will now increase as the buoyancy force will decrease (less ethanol is displaced). If one does the calculations as in the simple case, a volume much smaller than the actual volume of the sample, denoted here as the "donut volume", will be obtained (see figure). Nevertheless this calculation should be done, in addition to the one described next.

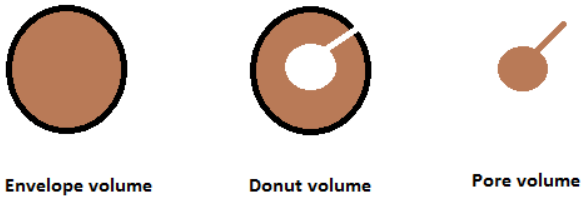

By measuring the weight of the dry sample and the wet sample (immediately after it has been taken out of the ethanol), one gets the weight of the ethanol that has impregnated the sample. Knowing the density of ethanol, one gets the volume of ethanol that has impregnated the sample and thereby the impregnated pore volume. Combining this with the donut volume that was previously calculated, the envelope volume of the sample is obtained.

Correcting for the volume of the string:

To get a more correct envelope volume, the volume of the submerged part of the string can be calculated (by measuring its dimensions) and subtracted from the donut volume (which is obtained as the sample is submerged). So the true, corrected, envelope volume becomes:

$$V_{envelope} = (V_{donut} - V_{string}) + V_{pore} \qquad \text{(A10)}$$

A4. Calculating the total conductivity and activation energy of a sample from impedance data

After fitting of the impedance data has been done to obtain the total resistance of the sample, the total conductivity can be calculated using the equation below:

$$\sigma_{tot} = \frac{L}{A * R_{tot}} \qquad \text{(A11)}$$

Where σ is the total conductivity, L the thickness of the pellet, A the average area of the electrodes on each side of the pellet and R_{tot} the total resistance obtained from the analysis.

Calculating the total conductivity for all temperatures and then plotting log(σ) against temperature, or inverse temperature, will produce plots of the type presented in the results and discussion section of this study.

The activation energy can either be calculated at temperatures above those of the conductivity plateau, which gives the activation energy for oxide ion conduction (since there are no protons left in the material) or it can be calculated at the lowest temperatures, before the conductivity plateau to get the activation energy for proton ion conduction. Demonstrating the procedure by the latter example, one must first and foremost use equation (A12) below:

$$\sigma = \frac{\sigma_0}{T}\exp\left(\frac{-E_a}{k_B T}\right) \qquad \text{(A12)}$$

Where σ is the conductivity, σ_0 is the pre-exponential factor, T is the temperature, k_B is the Boltzmann constant and E_a is the activation energy. Rearranging equation (A12) one gets:

$$\ln(\sigma T) = \ln(\sigma_o) + \left(\frac{-E_a}{k_B T}\right) \qquad \text{(A13)}$$

Plotting ln(σT) against 1/T will give a straight line with a y-intercept of $\ln(\sigma_0)$ and, more importantly, a slope of $-E_a/k_B$. The activation energy can thereafter be calculated by fitting the observed data using linear regression to obtain the slope and multiplying it with the Boltzmann constant.

Appendix 2 – Tabulated values and results

A2.1 Relative densities

Table 18. A table showing the calculated relative densities of all phase pure or near phase pure perovskite samples synthesized for this study.

Sample	*Relative density (%)*
T-BTS70, 1500°C	85.05 %
T-BTS70, 1500°C (2nd sintering)	79.65 %
T-BTS70, 1550°C	83.44 %
BSTS70, 1400°C	74.61 %
BSTS70, 1500°C	78.12 %
BSTS70, 1500°C (2nd sintering)	77.46 %
BSTS70, 1550°C	76.04 %
CIP-BTS70-D 1500°C, b.1	86.24 %

CIP-BTS70-W 1500°C, b.1	92.95 %
CIP-BTS70-W 1500°C, b.2	
Pellet #1	90.81 %
Pellet #2	83.73 %
Pellet #3	79.80 %
BTSI35 1200°C	
Pellet #1	75.39 %
Pellet #2	72.90 %
BTSI35 1400°C	81.99 %
BTSI50 1200°C	
Pellet #1	71.59 %
Pellet #2	71.04 %
BTSI50 1400°C	79.76 %
T-BTI70 1400°C	86.90 %
T-BTI70 1400°C, b.2 (2nd sintering)	83.94 %
BSTI70 1400°C	82.84 %
CIP-BTI70-D 1400°C b.1	87.39 %
CIP-BTI70-W 1400°C b.1	101.73 %
CIP-BTI70-W 1400°C b.2	
Pellet #1	N/A (misshaped)
Pellet #2	98.07 %
Pellet #3	98.05 %

A2.2 Pellet and electrode dimensions for samples analyzed using impedance spectroscopy

Table 19. A table showing the pellet thickness and average electrode are of the pellets analyzed using impedance spectroscopy.

Sample	*Pellet thickness (cm)*	*Average electrode area (cm²)*
CIP-BTS70-W #1	0.223	0.39
CIP-BTS70-W #3	0.286	0.58
CIP-BTI70-W #3	0.2235	0.535

Appendix 3 – Mass and volume losses during sintering

The mass and volume changes observed for all samples during the different sintering steps are presented below. Observe that there is more data available on mass loss than dimensional change because of the ease with which certain pressed pellets fractured during sintering or subsequent handling. Mass and volume loss is displayed in the figures as a percentage of the ingoing mass or volume for each sintering step.

A3.2 Mass losses

The mass losses recorded for all samples doped exclusively with indium are displayed in the figure below. It is clear that all samples experience a significant mass loss during the first heating, at 1000°C, very likely because of the decomposition of barium carbonate into barium and carbon dioxide. As further sintering treatments ensues, there is a trend showing decreasing mass losses for all samples up till 1400°C where the wet CIP samples display a higher mass loss, perhaps owing to evaporation of some remnant ethanol from the ceramic processing.

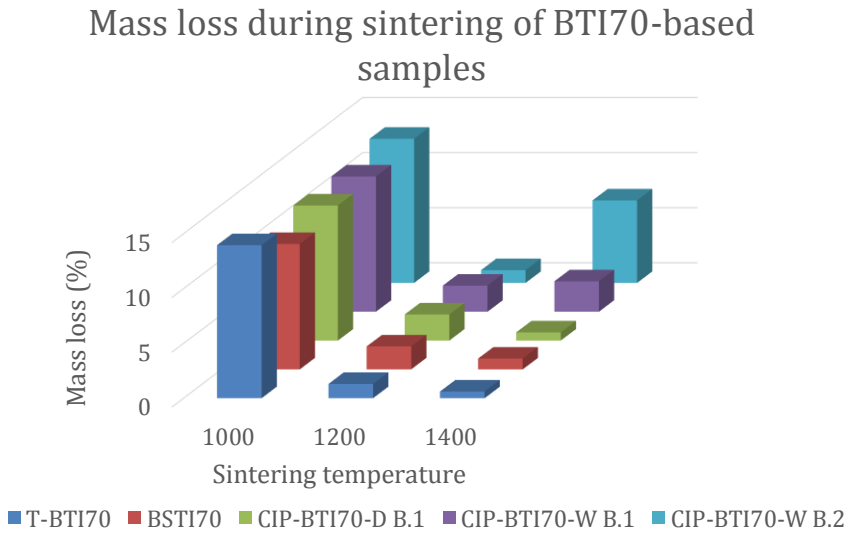

Figure 54. A figure showing the mass loss during sintering of all BTI70-based samples for each sintering step.

Looking at the samples doped exclusively with scandium, see figure 13, it can once again be stated that there is a large mass loss at 1000°C followed by successively smaller mass losses for each sintering. In addition, the wet CIP samples show a larger mass loss than all others at the highest common sintering temperature of 1500°C, owing to ethanol evaporation most likely.

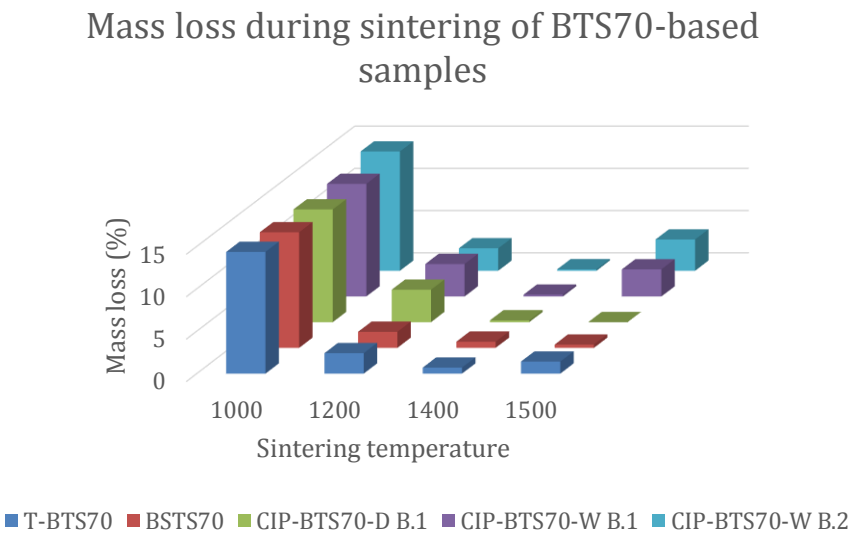

Figure 55. A figure showing the mass loss during sintering of all BTS70-based samples for selected sintering steps. Note that the second sintering at 1500°C and the sintering at 1550°C have been left out for clarity but are displayed in the figure below.

Expanding the graph above to include sintering steps 4b and 5, reveals an increasing mass loss of the tin-containing BTS70 sample. A possible reason for this trend break is examined later on.

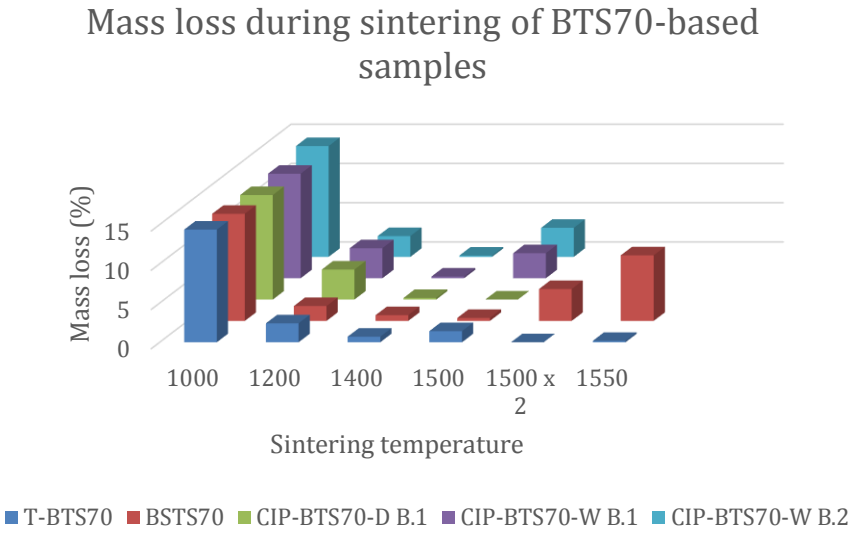

Figure 56. A figure showing the mass loss during sintering of all BTS70-based samples for each sintering step.

The only samples not included in the above graphs are the mixed scandium/indium samples since they don't really belong to either the BTI70-based or BTS70-based samples and are instead a hybrid of both. Their mass losses are therefore displayed next to T-BTS70 and T-BTI70 for comparison in the figure below.

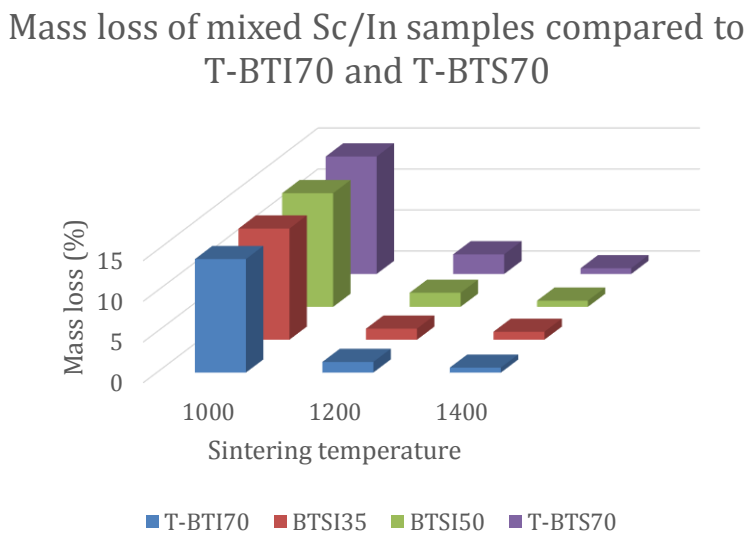

Figure 57. A figure showing the mass loss during sintering of the BTSI35 and BTSI50 samples for each sintering step. Their mass losses are displayed next to those of T-BTI70 and T-BTS70 for comparison.

As can be seen, at least at the 1200°C sintering, their mass loss trends display a behavior in between that of T-BTI70 and T-BTS70 sample, losing less mass than the BTS70 sample and more than the BTI70 sample. This, in conjunction with results from XRD etc, will be deliberated later on.

A2.2 Volume losses

Looking at volume losses during sintering of the BTI70 based samples at 1400°C, shows that both batches of wet CIP samples display the largest decrease in volume followed by the trial BTS70 sample and the dry CIP sample, with the BSTI70 sample displaying the smallest loss of volume.

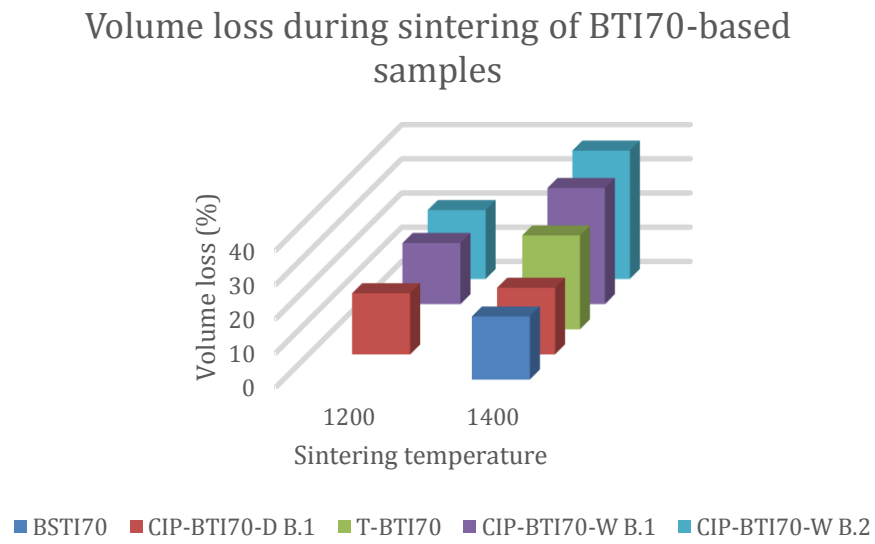

Figure 58. A figure showing the volume loss during sintering of all BTI70-based samples for each sintering step.

The BTS70 based samples display almost the exact same trend as the BTI70 based samples at the highest common sintering temperature of 1500°C, the only difference being that batch 1 and 2 of the wet CIP samples have switched places, see figure 17.

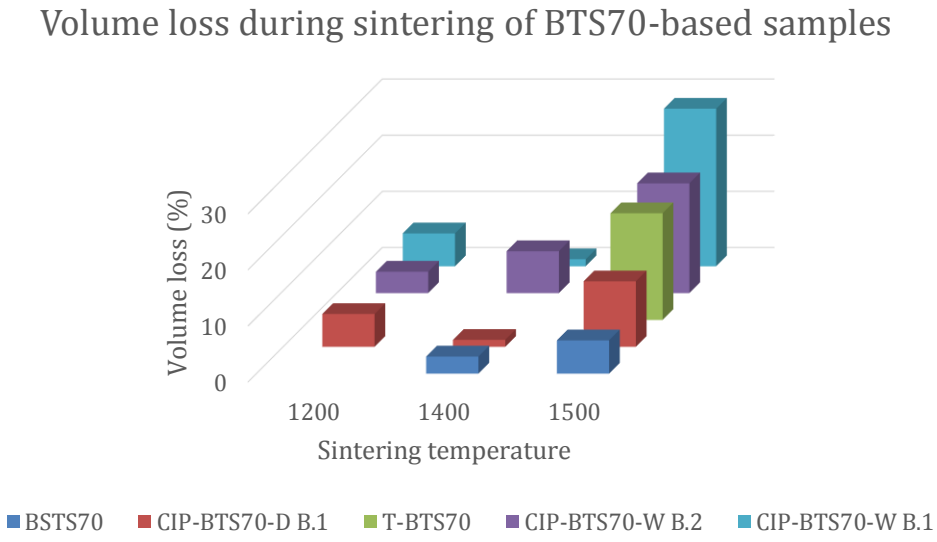

Figure 59. A figure showing the volume loss during sintering of all BTS70-based samples for selected sintering steps. Note that the second sintering at 1500°C and the sintering at 1550°C have been left out for clarity but are displayed in the figure below.

Expanding the graph above to include the second heating at 1500°C as well as at 1550°C, it can be seen that further volume loss takes place for the samples subjected to these sintering steps, namely BSTS70 and T-BTS70.

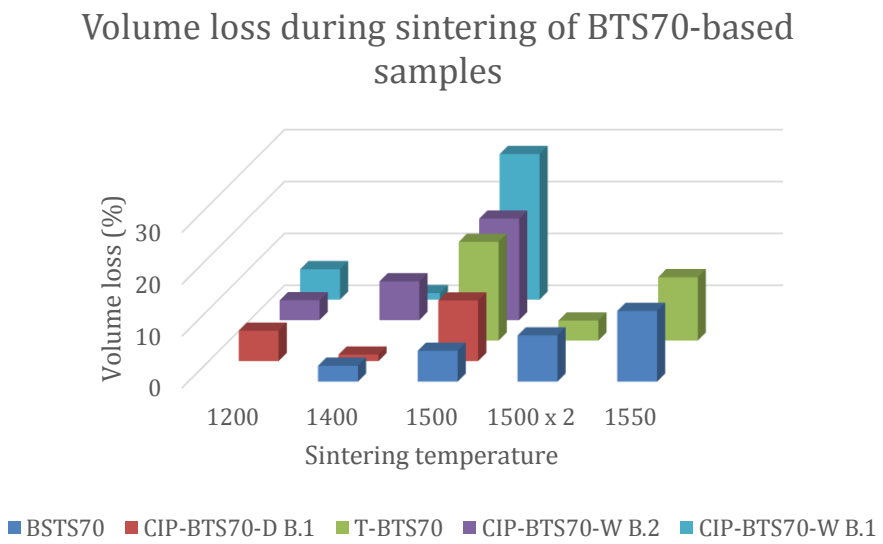

Figure 60. A figure showing the volume loss during sintering of all BTS70-based samples for each sintering step.

Looking at the BTSI35 and BTSI50 samples, although perhaps not displaying as clear a trend as for the mass losses, their volume losses seem to be somewhat in between those of the CIP-BTS70- D and CIP-BTI70-D samples, at least at 1400°C. The mixed Sc/In samples are compared to the dry pressed CIP samples in this case because of lack of volume loss data on T-BTS70 at 1400°C.

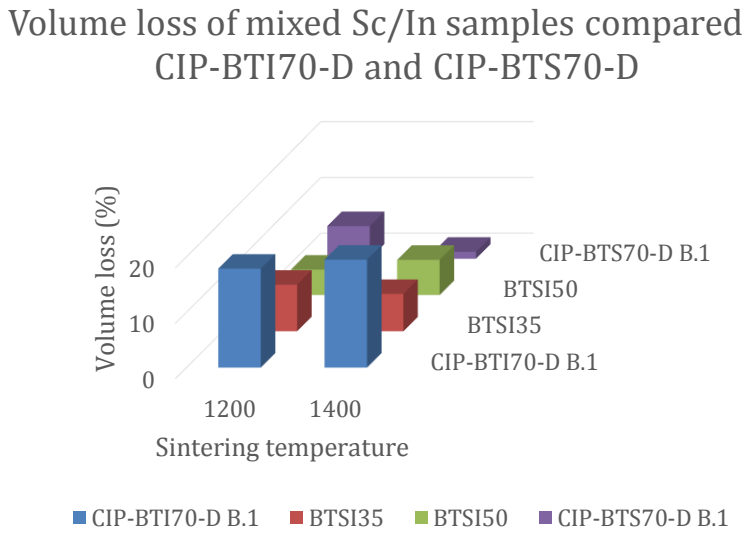

Figure 61. A figure showing the volume loss during sintering of the BTSI35 and BTSI50 samples for each sintering step. Their mass losses are displayed next to those of dry pressed CIP-BTI70 and CIP-BTS70 for comparison because of the lack of volume loss data on T-BTS70 at 1400°C.